



**TECHNISCHE  
UNIVERSITÄT  
WIEN**

Vienna University of Technology

# CO oxidation reaction on palladium - platinum model catalysts: the role of the support

ausgeführt zum Zwecke der Erlangung des akademischen Grades eines  
Magisters der Naturwissenschaften unter der Leitung von

**Assoc.Prof. Dipl.-Phys. Dr.rer.nat. Yuri Suchorski**  
Institut für Materialchemie (E165)

eingereicht an der Technischen Universität Wien  
Fakultät für Technische Chemie

von

**Martin Datler**

Matrikelnummer e0625984

Liechtensteinstraße 117

1090 Wien, Österreich

Datum

# Kurzfassung

---

In der vorliegenden Diplomarbeit werden verschiedene Faktoren, die möglicherweise das katalytische Verhalten von Modellkatalysatoren in der CO-Oxidation unter Hochvakuumbedingungen beeinflussen, untersucht. Dieses Thema wurde primär aus zwei Gründen gewählt: Obwohl die einzelnen katalytisch aktiven Bestandteile der Drei-Wege-Katalysatoren, die in Millionen von Autos zum Einsatz kommen, um die gesundheitsschädlichen Abgase der Verbrennungsmotoren zu verringern, bereits sehr gut untersucht sind, ist nur wenig über die Wechselwirkungen zwischen den katalytisch aktiven Partikeln oder über die Details der Wechselwirkungen zwischen den verwendeten Trägermaterialien und den Katalysatoren bekannt. Zweitens weckt das tiefe Verständnis des Langmuir-Hinckelwood-Mechanismus, welches auf zahlreichen Studien beruht, die Hoffnung, neue Erkenntnisse über die oben genannten Wechselwirkungen zu erhalten.

Die verwendeten Modellsysteme wurden mittels eines Photoelektronenmikroskops (PEEM, engl. photoemission electron microscope) untersucht. Ein PEEM fokussiert Photoelektronen, welche aus einer Probe emittiert werden, auf einen Phosphorbildschirm, um die Probenoberfläche in einem  $\mu\text{m}$ -Maßstab abzubilden. Da der Kontrast der PEEM-Bilder von der Anzahl der lokal emittierten Photoelektronen abhängt, resultieren Veränderungen der Bildhelligkeit hauptsächlich aus Veränderungen der Adsorbatenbedeckung, wie z.B. Kohlenmonoxid (CO) und Sauerstoff.

Reaktionen, die dem Langmuir-Hinckelwood-Mechanismus folgen, zeigen unter bestimmten Bedingungen ein bistabiles Verhalten: Beispielsweise zeigt die heterogen katalysierte CO-Oxidation zwei stationäre Zustände und einen bistabilen Bereich; sobald der CO-Druck innerhalb der Reaktionskammer einen gewissen Wert erreicht hat, findet der kinetische Übergang von der sauerstoffbedeckten Probenoberfläche (stationärer Zustand hoher katalytischer Aktivität) zu der CO-bedeckten Probenoberfläche (stationärer Zustand niedriger katalytischer Aktivität) an dem Übergangspunkt  $\tau_A$  statt, wohingegen der inverse kinetische Übergang von einer CO-bedeckten zu einer sauerstoffbedeckten Oberfläche am Übergangspunkt  $\tau_B$  stattfindet. Zwischen  $\tau_A$  und  $\tau_B$  befindet sich der Bistabilitätsbereich, in dem die Probe unter exakt denselben Reaktionsbedingungen (Temperatur, Partialdrücke von CO und Sauerstoff), in Abhängigkeit von der experimentellen

Vorgeschichte, entweder katalytisch aktiv oder inaktiv sein kann.

Die kinetischen Übergänge während der CO-Oxidation wurden im Zuge dieser Arbeit mit Hilfe eines PEEMs studiert, um Informationen über das lokale katalytische Verhalten der untersuchten Proben zu erhalten. Mehrere Sätze von Übergangspunkten, die alle bei demselben partiellen Sauerstoffdruck, aber bei unterschiedlichen Temperaturen gemessen wurden, können in einem  $T/p_{CO}$ -Phasenraum als sogenanntes kinetisches Phasendiagramm abgebildet werden, welches das katalytische Verhalten der Probe in einem bestimmten Parameterbereich charakterisiert. Die das katalytische Verhalten der Probe in der CO-Oxidation charakterisierenden Daten wurden entweder durch isotherme Experimente (der partielle Kohlenmonoxiddruck wurde bei konstanter Temperatur zyklisch verändert) oder durch isobare Messungen (die Temperatur wurde bei konstanten Partialdrücken von CO und Sauerstoff zyklisch variiert), welche einen „Kaltstart“ eines realen Katalysators simulieren, erhalten.

Um neue Einblicke in die auftretende Wechselwirkung zwischen den katalytisch aktiven Partikeln und dem verwendeten Trägermaterial sowie in die Rolle der Morphologie des Katalysators zu erhalten, wurde eine Pd/Pt-Modellsystemprobe untersucht, die durch das Imprägnieren von Palladium-Pulver (Pd-Pulver) in eine Platin-Folie (Pt-Folie) hergestellt wurde. Ein weiteres Modellsystem wurde durch das Imprägnieren desselben Pd-Pulvers in eine  $Al_2O_3$ -Folie hergestellt, wohingegen eine reine polykristalline Pt-Folie und eine reine polykristalline Pd-Folie als Referenzproben verwendet wurden.

Um die katalytischen Eigenschaften des Pd-Pulvers mit denen der Pt-Folie direkt vergleichen zu können, wurde für die PEEM-Messungen eine Region der Pd/Pt-Probe ausgewählt, in der sich zwei Pd-Pulver Agglomerate sowie verschiedene Domänen der Pt-Folie befanden. Zwei Pt-Domänen, Pd(100) und Pt(110), wurden durch den Vergleich der lokal gemessenen PEEM-Intensität bei unterschiedlichen Adsorbatbedeckungen identifiziert. Die kinetischen Phasendiagramme, die für die besagten Domänen lokal gemessen wurden, zeigten eine gute Übereinstimmung mit den Phasendiagrammen zweier Domänen einer reinen Pt-Folie, welche dieselbe kristallographische Orientierung aufweisen. Das lokal ermittelte Phasendiagramm für die Pd-Pulver Agglomerate weist hingegen signifikante Unterschiede zu jenem der Pt-Domänen auf. Daraus folgt, dass beide katalytisch aktiven Bestandteile der Pd/Pt-Probe ihre Unabhängigkeit in Bezug auf ihre katalytische Wirkung in der CO-Oxidation unter den gegebenen (Hochvakuum-) Bedingungen beibehalten.

Der Vergleich der Reaktivität der beiden Pd-Agglomerate, welche sich im  $\mu m$ -Bereich in ihrer Größe und ihrer Form unterscheiden, zeigt, dass die katalytische Aktivität nicht von Unterschieden der Agglomeratsgröße oder Agglomeratsform (in der besagten Größenord-

nung) beeinflusst wird. Weiters wurde ein Phänomen beobachtet, das bisher noch nicht in der Literatur beschrieben wurde: das Auftreten von Reaktionsfronten auf katalytisch aktiven Pulveroberflächen. Der Vergleich der evaluierten Geschwindigkeiten der Reaktionsfronten auf der rauen Oberfläche des Pd-Teils der Pd/Pt-Probe und des Pd-Teils der Pd/Al<sub>2</sub>O<sub>3</sub>-Probe mit den Geschwindigkeiten von auftretenden Reaktionsfronten auf einer Ar<sup>+</sup> gesputterten Pd-Folie, deren Oberfläche durch die zahlreichen künstlich herbeigeführten Stufen und Defekte eine ähnliche Morphologie wie die der Pulverproben aufweist, zeigt, dass die verwendeten Trägermaterialien die katalytischen Eigenschaften signifikant beeinflussen.

Abschließend konnte der Unterschied zwischen dem katalytischen Verhalten der gesputterten Pt-Folie und der gepressten Pd/Al<sub>2</sub>O<sub>3</sub>-Probe erklärt werden: Die erhobenen Daten weisen darauf hin, dass die Oxid-Metall-Wechselwirkung zwischen dem Trägermaterial und dem imprägnierten Pd-Pulver das katalytische Verhalten der katalytisch aktiven Partikeln signifikant beeinflusst. Andererseits zeigt der Vergleich des Pd/Pt-Systems mit der gesputterten Pd-Folie, dass die Pt-Folie das katalytische Verhalten des Pd-Pulvers kaum beeinflusst.

# Abstract

---

The aim of the present thesis was to study factors which might influence the catalytic behaviour of model catalysts in the CO oxidation reaction under high vacuum conditions. This topic was chosen for two main reasons: although there already is a lot of data concerning the individual catalytic components of the three-way catalyst which is used in millions of cars to decrease the harmful pollutant emissions of the combustion engines, we still do not know much about the interactions between the catalytically active particles or details of the interaction between the support and the catalyst. Secondly, the good understanding of the Langmuir-Hinshelwood mechanism of the CO oxidation reaction, which is based on a considerable number of studies, provides the hope to reveal details of the interactions mentioned above.

The studies were performed using a photoemission electron microscope (PEEM). A PEEM focuses photoelectrons which are emitted from a sample onto a phosphorous screen to image the sample surface in the low  $\mu m$ -range. As the contrast of PEEM images depends on the number of photoelectrons which are emitted from a certain area of the sample surface, changes in the local image brightness result mainly from changes of the surface coverage by adsorbates, e.g. CO or oxygen.

Reactions following the Langmuir-Hinshelwood mechanism show a bistable behaviour under certain reaction conditions: e.g. the CO oxidation reaction shows two steady states and a region of bistability; at increasing CO pressure in the reactor, the kinetic transition from the oxygen-covered surface (steady state of high reactivity) to the CO-covered surface (steady state of low reactivity) takes place at the transition point  $\tau_A$ , while the reverse kinetic transition from an CO- to an oxygen-covered surface takes place at  $\tau_B$ . Between  $\tau_A$  and  $\tau_B$  there is the area of bistability, where the sample can be either reactive or inactive at exactly the same reaction conditions (temperature and partial pressures of CO and oxygen), depending on its prehistory.

In the present work the kinetic transitions during the CO oxidation reaction were monitored by a PEEM to obtain information about the local catalytic behaviour of the studied samples. A set of transition points which were obtained at the same partial oxygen pressure, in a  $T/p_{CO}$  parameter space is called kinetic phase diagram. Such a kinetic phase

diagram characterises the catalytic behaviour of a sample in a certain parameter range. The data concerning the kinetic behaviour of the samples in the CO oxidation reaction were obtained from isothermal measurements (temperature and partial oxygen pressure were held constant while the partial CO pressure was changed cyclically) as well as from isobaric ignition-extinction measurements (partial oxygen and partial CO pressure were held constant while the temperature was changed cyclically) which simulate a „cold-start“ of a real catalyst.

To receive new insights into the interaction between the catalytic particles and their supports and to reveal the role of the surface morphology in the catalytic behaviour, a Pd/Pt model system sample was prepared by impregnating Pd powder into a Pt foil. Another model system was prepared by impregnating the same Pd powder as in the Pd/Pt model system into an Al<sub>2</sub>O<sub>3</sub> foil, while a pure polycrystalline Pt and a pure polycrystalline Pd foil served as reference samples.

To directly compare the catalytic properties of Pd with those of Pt, a certain region of the Pd/Pt model system sample, where two Pd powder agglomerates and different domains of the Pt foil were visible, was chosen. Two low Miller index domains, namely Pt(100) and Pt(110), were determined by comparing the local PEEM image intensities at different adsorbate coverages. The kinetic phase diagrams obtained for these domains show a good agreement with the previous studies for the domains of the same crystallographic orientation of a pure polycrystalline Pt foil. In turn, the kinetic phase diagrams for the Pd powder agglomerates, which were locally obtained, differ significantly from those for the Pt domains, i.e. that the Pd and Pt components of the combined Pd/Pt system sample retain their independence in respect to the CO oxidation under the present (high vacuum) conditions.

The comparison of the data received for the two Pd powder agglomerates of the Pd/Pt model system sample, which differ in size and shape, shows that the catalytic reactivity of Pd powder agglomerates is not influenced by variations of size and shape in the  $\mu\text{m}$ -scale. Further, a phenomenon which has not been described in the literature yet, could be observed: the occurrence of reaction fronts on powder surfaces. The comparison of the velocities of the reaction fronts on the Pd part of the Pd/Pt sample and the Pd part of the Al<sub>2</sub>O<sub>3</sub> sample with those on a sputtered Pd foil whose surface has (due to the artificially created steps and defects) a morphology similar to that of the powder surfaces, shows, that the supports have a significant influence on the behaviour of the reaction fronts.

Finally, the striking difference between the catalytic behaviour of a sputtered Pd foil and the pressed Pd powder which was supported by an Al<sub>2</sub>O<sub>3</sub> foil could be explained: the

oxide-metal interaction between the oxidic supporting material ( $\text{Al}_2\text{O}_3$ ) and the impregnated Pd powder changes the catalytic behaviour of the catalytically active Pd particles significantly. Additionally, the comparison of the Pd part of the Pd/Pt model system with a sputtered Pd foil shows that the Pt foil used as support for the same Pd powder has no significant influence on its catalytic behaviour.

# Acknowledgements

---

I would like to express my thanks to the people who have supported me during the time it took me to write this thesis. I would like to thank...

... **Prof. Yuri Suchorski**, who always took the time to supervise and support me with his advice during all stages of this thesis.

... **Dipl.-Phys. Diana Vogel**, who taught me a lot about the daily life of a scientist working in a laboratory.

... **MSc Zuzana Budinská** and **MSc Ivan Bepalov** for the great collaboration.

... **Prof. Günther Rupprechter**, the head of the IMC, who enabled me to work on my thesis at this institute.

... the **Fonds zur Förderung der wissenschaftlichen Forschung (FWF)** and in particular the Special Research Program „Functional Oxide Surfaces and Interfaces“ (SFB F45 „FOXSI“) for financially supporting my research.

... **Johannes Frank** for all his technical support concerning the experimental setup.

... **my parents and my sister** for always supporting me during my studies with the various things I needed.

... **my friends** for their moral support; specially **Felix Leditzky** and **Christine Zeiler**.

... **Angelika**, for more than words could ever say.

# Table of Contents

---

<b>1</b>	<b>Introduction</b>	<b>3</b>
1.1	How catalysts changed the face of the world . . . . .	3
1.2	The principles of catalysis . . . . .	6
<b>2</b>	<b>CO oxidation reaction on platinum group metal</b>	<b>8</b>
2.1	CO oxidation reaction . . . . .	8
2.2	Environmental importance of the CO oxidation reaction . . . . .	9
2.3	Elementary steps of the CO oxidation reaction . . . . .	11
2.4	The Langmuir-Hinshelwood mechanism of the CO oxidation reaction . . .	13
2.5	Bistability and the kinetic phase diagram . . . . .	14
<b>3</b>	<b>Experimental</b>	<b>18</b>
3.1	The ultrahigh vacuum system . . . . .	18
3.1.1	Vacuum pumps . . . . .	19
3.1.2	Pressure measurement . . . . .	21
3.1.3	Gas inlets and ion sputter gun . . . . .	22
3.1.4	Sample transfer . . . . .	22
3.1.5	XPS chamber . . . . .	22
3.1.6	PEEM chamber . . . . .	23
3.2	Methods . . . . .	23
3.2.1	X-ray Photoelectron Spectroscopy . . . . .	24
3.2.1.1	The photoeffect . . . . .	25
3.2.1.2	Principle of the electron energy analysis . . . . .	28
3.2.1.3	The surface sensitivity of XPS . . . . .	30
3.2.1.4	Hemispherical Electron Energy Analyser . . . . .	32
3.2.1.5	The XPS-spectrum . . . . .	34
3.2.2	Photoemission Electron Microscopy . . . . .	37
3.2.2.1	Working principle of the PEEM . . . . .	38

*Table of Contents*

3.2.2.2	Layout of a UV-PEEM . . . . .	40
3.2.2.3	Evaluation of PEEM images . . . . .	41
3.2.3	Quadrupole Mass Spectrometry . . . . .	42
3.2.3.1	The Ion source of the QMS . . . . .	43
3.2.3.2	The quadrupole mass analyser of the QMS . . . . .	44
3.2.3.3	The detector of the QMS . . . . .	46
<b>4</b>	<b>The model system: Pd powder on Pt foil</b>	<b>50</b>
4.1	Platinum and palladium . . . . .	50
4.2	The sample . . . . .	52
<b>5</b>	<b>CO oxidation reaction on the Pd/Pt model system</b>	<b>54</b>
5.1	Experimental procedure . . . . .	54
5.2	Global kinetic behaviour of the CO oxidation reaction catalysed by the Pd/Pt model system . . . . .	55
5.3	Local kinetics of the CO oxidation on the Pt part of the sample . . . . .	58
5.4	CO oxidation on the Pd part of the sample . . . . .	62
5.4.1	Local kinetics of CO oxidation on a Pd part of the combined sample	62
5.4.2	The role of the size and shape of Pd agglomerates in the CO oxidation	65
5.4.3	Reaction front propagation during the catalytic CO oxidation on Pd	68
5.4.3.1	Reaction fronts . . . . .	68
5.4.3.2	Reaction fronts on Pd samples with different morphologies	71
5.4.4	Comparison of the CO oxidation on Pd samples of different mor- phology . . . . .	74
<b>6</b>	<b>Summary and Conclusions</b>	<b>77</b>
	<b>List of figures</b>	<b>80</b>
	<b>References</b>	<b>83</b>
	<b>Oral talks and poster presentations</b>	<b>85</b>

# 1

## Introduction

---

### 1.1 How catalysts changed the face of the world

The first known catalyst was used by the Sumerians in Mesopotamia who catalysed the alcoholic fermentation of sugar already in 6000 B.C. The importance of catalysis increased during the centuries and nowadays a life without catalysts is nearly unthinkable. For example the population in Europe increased enormously during the 19<sup>th</sup> century because the birthrate increased after the abolition of serfdom, the loss of the influence of the church and also because people thought of their children as a provision for their old age. At the same time the increased knowledge of medicine, the awareness of the importance of hygiene, the expansion of transport routes, which enabled a better sharing of food stocks, and many other achievements of this time decreased the death rate. As always in history, society changed and the economic system had to adapt to the new situation - Europe was looking forward to mass starvation, but in 1910 A.D. Carl Bosch and Fritz Haber filed a patent application for their Haber-Bosch process<sup>1</sup> which enabled the production of a sufficient amount of ammonia, which was and still is processed further to fertilizers. Without the possibility to produce masses of fertilizers, agriculture could never satisfy

---

<sup>1</sup>The Haber-Bosch process uses iron (with impurities of  $\text{Al}_2\text{O}_3$ ,  $\text{K}_2\text{O}$  and  $\text{CaO}$ ) as a catalyst to process  $\text{N}_2$  and  $\text{H}_2$  at approximately 150 to 320 *bar* and 720 *K* to 820 *K* to  $\text{NH}_3$ .

## 1 Introduction

the enormous demand for food. Since 1910 the consumption of ammonia has increased continuously and reached approximately 200 million tons in 2011, which could not be produced without the catalyst in the Haber-Bosch process.

Many different catalysts are nowadays used in big scale industries, but also millions of people use them in daily life although some of them do not realize it. We are talking about the ramifications of the development of the first car in 1885 by Carl Benz, which changed our daily life and our environment; e.g. the significant increment of harmful pollutant emission (compared to the time before 1885). One of the biggest successes in combating automobile exhaust pollution was the development of the three-way catalyst.<sup>2</sup>

These are only two examples in order to show that we could not live our present life without catalysts - but although they are that important for us, one still has problems understanding all the details of many catalytic processes. Some time ago, scientists attempted to improve catalysts by the very expensive trial-and-error method, because they had not enough profound knowledge about such complex catalytic reactions. Today science tries to understand these complex processes and the linked parameters that influence the reactivity of catalysts and the catalysed reaction. Because these systems are very complex, it is useful to simplify them, so that it is possible to examine only a few parameters.

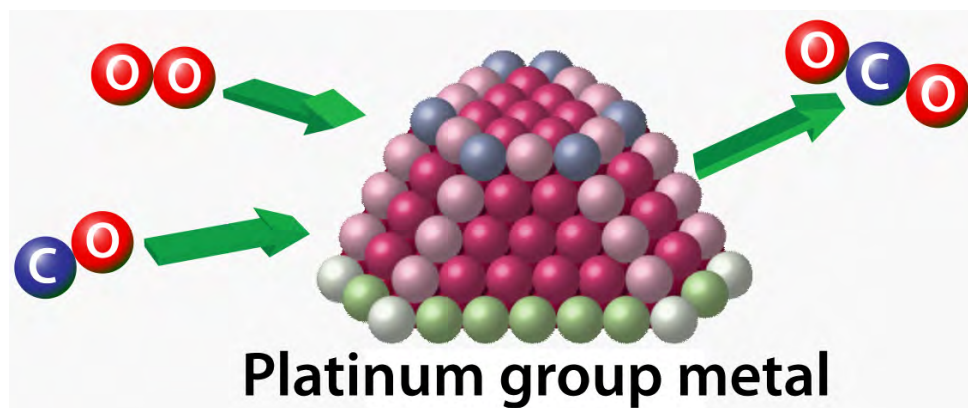


**Fig. 1.1:** Even such a seemingly simple catalytic reaction as the CO oxidation on platinum group metals appears too complex to study all its details simultaneously under real conditions. It is, however, reasonable to study some details of the CO oxidation reaction on simplified models of real catalysts.

This simplification leads to a so-called *material gap* and a so called *pressure gap*. The material gap refers to the simplification of the sample: for example a platinum or palladium powder that is impregnated onto a supporting material can be modelled by a single

---

<sup>2</sup>See chapter 2.2 “Environmental importance of the CO oxidation reaction” for further details.

## 1 Introduction

crystal of the catalytic active material. The study of single crystals should provide enough results to enable the study of a more complex system (for example a polycrystalline foil), which again provides enough results to enable the study of an even more complex system (powder impregnated on a support), etc. The main idea is to increase the complexity of the model system step by step to bring the studied samples gradually closer to the real catalyst.

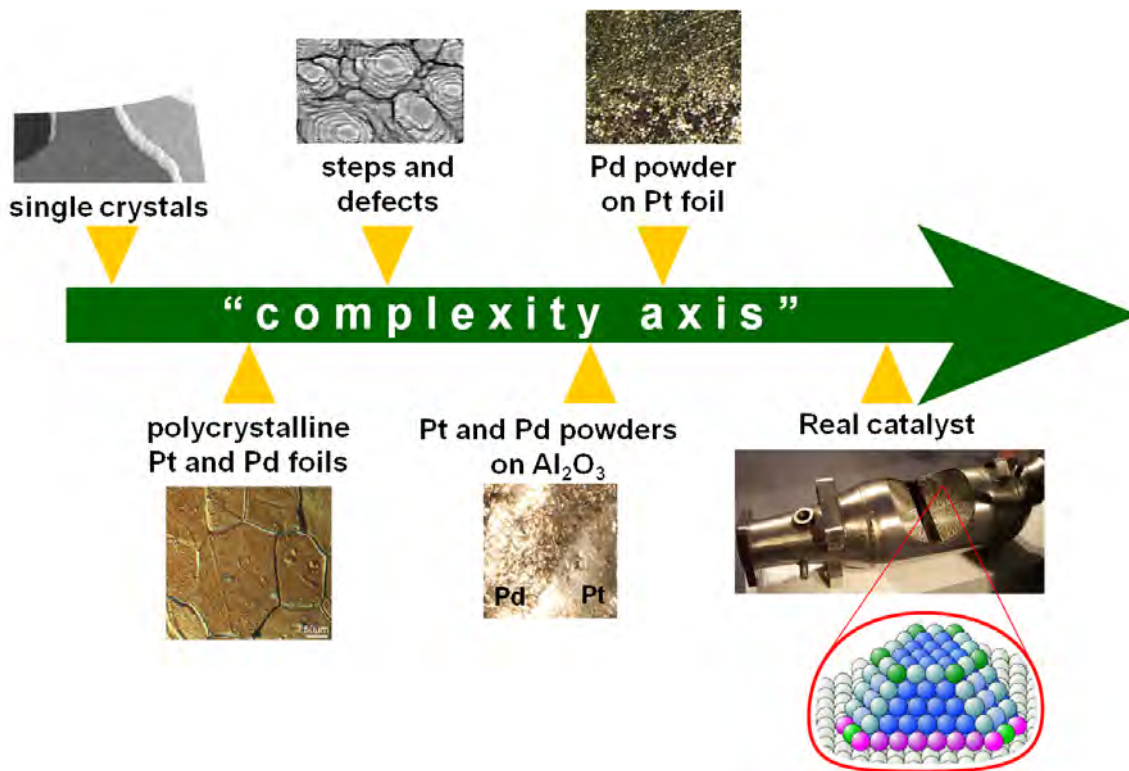


**Fig. 1.2:** Different catalytic model systems in surface science along the “complexity axis”. The picture of the real catalyst was taken from Ref. [1].

Additionally, the gaseous phase can be simplified by reducing the pressure, thus resulting in the pressure gap. If one performs experiments under ultra high vacuum conditions (UHV,  $10^{-8}$  to  $10^{-10}$  mbar), the partial pressures of all gases are at least as low as this pressure. If the pressure of a certain species increases to high vacuum (HV,  $10^{-4}$  to  $10^{-6}$  mbar), all other partial pressures remain at the same pressure. This means that they become negligible, because the pressures would only differ by a factor of approximately  $10^4$ . This pressure difference results in clearly defined reaction conditions. By increasing the pressures inside the experimental setup the pressure gap can be reduced until real conditions are reached.

The importance of studies on model systems which differ from real catalysts by a material

and a pressure gap was shown among others by Gerhard Ertl, who was honoured with the Nobel Prize in 2007 “for his studies of chemical processes on solid surfaces of single crystals in high vacuum conditions” [2].

The results presented in this thesis, which concern different influences like the supporting material, the morphology of the catalytically active surface or the shape of powder agglomerates on the catalytic behaviour of the catalyst in the CO oxidation reaction, were mainly obtained from a palladium/platinum model system sample. This new insight might be a further step on the long way towards understanding heterogeneous catalytic processes in all their details.

## 1.2 The principles of catalysis

Most chemical reactions need an activation energy  $E_A$  to process their reagents to products because of the energetically unfavourable transition state along the reaction coordinate. This activation energy can be reduced by using a catalyst.

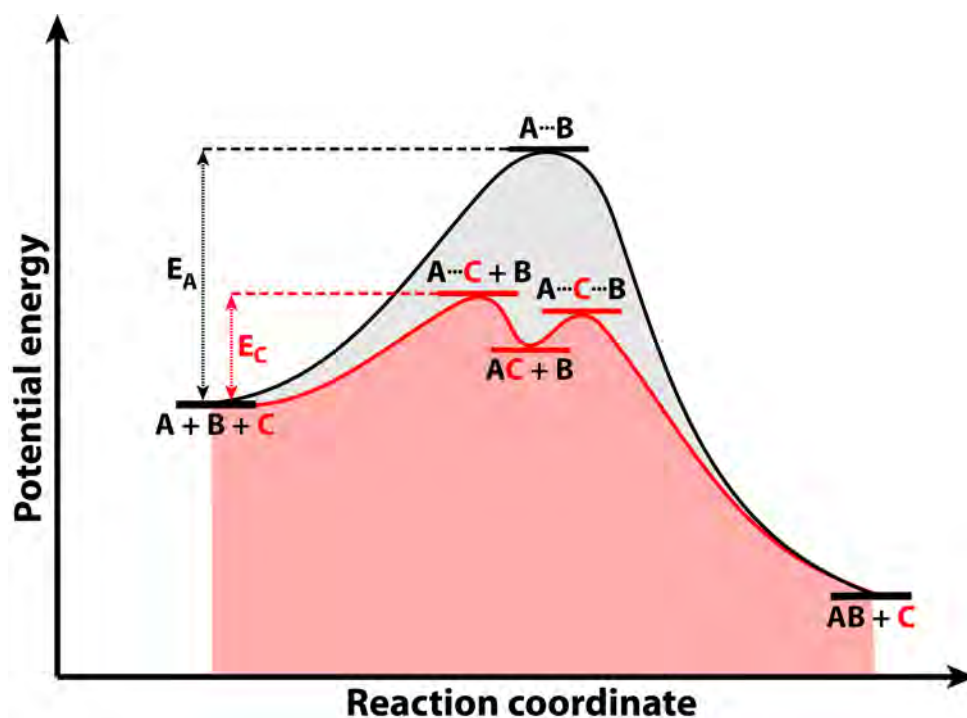


**Fig. 1.3:** Energy diagram of the chemical reaction  $A + B \rightarrow AB$  with (red) and without (gray) using a catalyst:

The activation energy of the catalysed reaction  $E_C$  is much smaller than the activation energy of the uncatalysed reaction  $E_A$ .

## 1 Introduction

The chemical reaction  $A + B \rightarrow AB$  shown in Fig. 1.3 needs the activation energy  $E_A$  to produce the product  $AB$  out of the two reagents  $A$  and  $B$ . If a suitable catalyst  $C$  is added to the reaction system, there occur one intermediate product ( $KA + B$ ) and two transition states ( $K \cdots A + B$  and  $A \cdots K \cdots B$ ). As a result of this intermediate product and the two transition states the activation energy is reduced to  $E_C$ , which is significantly smaller than  $E_A$ .

The activation energy can be used to calculate the reaction rate  $k$  from the equation

$$k = A \cdot e^{-\frac{E_A}{k \cdot T}} \quad (1.1)$$

where  $A$  is the pre-exponential factor,  $T$  the temperature and  $k$  the Boltzmann constant. The equation demonstrates convincingly how the use of a catalyst facilitates the reaction rate by reducing the activation energy  $E_A$ .

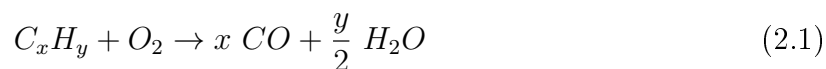
# 2

## CO oxidation reaction on platinum group metal

---

### 2.1 CO oxidation reaction

The major part of the toxic and ecologically harmful carbon monoxide (CO), which is one of the products of the incomplete combustion of carbonaceous compounds ( $C_xH_y$ ), is produced by big scale industries, traffic and households.



The harmful CO can be oxidised to  $CO_2$ .

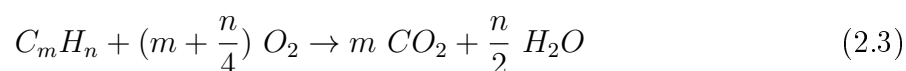


Carbon dioxide is an important reagent of the carbon cycle, because plants and other autotrophic organisms photosynthesize carbohydrates (e.g. sugar, etc.) and oxygen which is in fact a waste product out of carbon dioxide, water and light. Carbon dioxide is also used by big scale industries for the production of urea derivatives, beverages, wine, fire extinguishers, dry ice, food additive, etc.

## 2.2 Environmental importance of the CO oxidation reaction

Over decades the exposure of the environment to carbon monoxide increased until it reached a earnestly harmful level for the population. Therefore, the amount of CO that big scale industries, cars, etc. are allowed to produce, was and still is regulated by national or supranational bodies. If, for example, all cars that are used daily by millions of people all over the world drove without having a three-way catalyst, the resulting pollutant emissions would seriously harm people's health. And although nowadays most cars are equipped with a three-way catalyst, it is presumed that hundreds of thousands of people die annually from the consequences of traffic-related air pollution.

Combustion products of car engines mainly contain carbon monoxide, nitrogen monoxides, unburned hydrocarbon and water vapour. The three-way catalyst converts these products into carbon dioxide, water vapour and nitrogen by oxidising unburnt hydrocarbon into carbon dioxide and water, reducing nitrogen oxides to nitrogen and oxygen and oxidising carbon monoxide to carbon dioxide:



A typical three-way catalyst consists of a ceramic monolith with a honeycomb structure, a dumping layer, a stainless steel housing, a support material, the washcoat and the catalytically active particles. The monolith has a very rough surface to provide enough space for the washcoat which is the carrier for the catalytically active noble metal particles. The washcoat is made of aluminium oxide (like  $Al_2O_3$ ), titanium dioxide, silicon dioxide or a mixture of them. Furthermore, cerium oxide is added which can store or evolve oxygen if necessary. Alumina has a large surface in the gamma modification (150 - 175 m<sup>2</sup>/g [6]), which can change at higher temperatures into the alpha modification, that provides less catalytically active area. Further, rhodium and other noble metals can diffuse into it. The catalytically active nano particles used in the three-way catalyst are palladium, platinum and rhodium. Palladium is a very good catalyst for the oxidation process of carbon monoxide and hydrocarbons, but a less active catalyst for the reduction of ni-

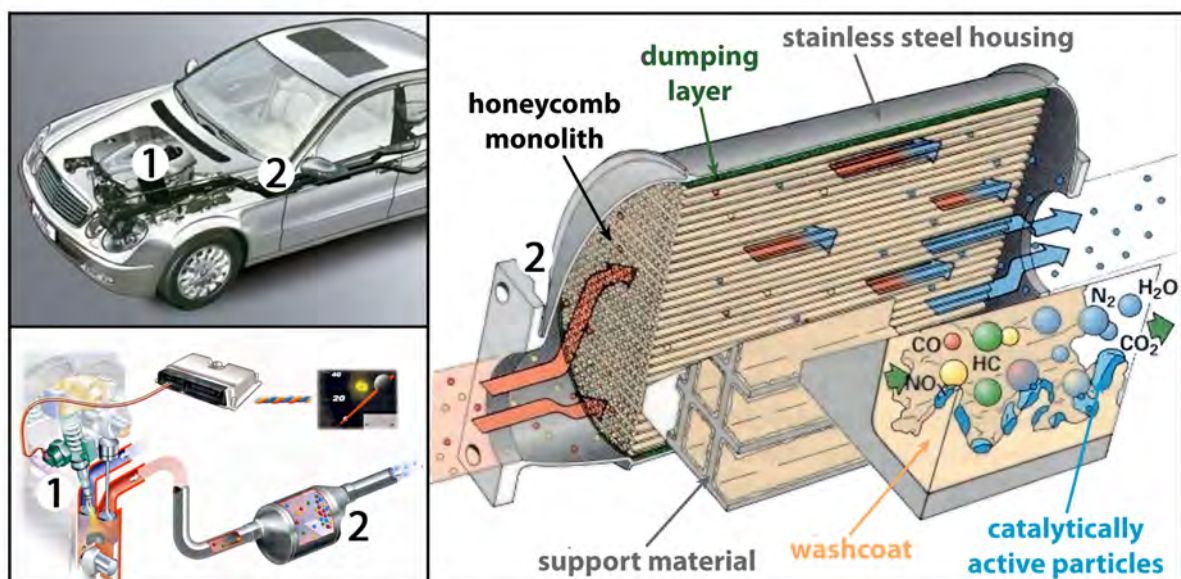


**Fig. 2.1:** Schematic illustration of the three-way catalyst. (The original pictures were adapted from Ref. [3] - [5].)

trogen monoxide. Platinum is the most active common catalyst for the reduction and the oxidation processes inside the three-way catalyst, but it is also quite insensitive to contaminations like sulphur. Rhodium is very expensive, but it has unique structural and chemical properties, which make it a very active catalyst for nitrogen monoxide reactions. The three-way catalyst is most efficient while working at temperatures between 350 and 650°C. Below 350°C the catalyst is as inefficient as ineffective and if the catalyst reaches higher temperatures, like 800°C, there is a danger of sintering the catalytic nano particles together and thereby reducing their catalytically active surface. Especially ineffectivity at lower temperatures became a big problem since modern cars which are based on the hybrid technology or electric engines only sporadically use the internal combustion engine which normally heats the three-way catalyst up to its working temperature. As a result, the catalyst remains below its working temperature most of the time, and is therefore not able to catalyse the reactions effectively. While some car producers try to avoid this problem by using an electrical heating which requires a heavy and voluminous battery, others try to use a second, smaller three-way catalyst that can be heated up very quickly but therefore cannot deal with high flow rates. Both expensive attempts show the environmental importance of this topic and the necessity of further research in this field in order to understand more details about the catalytic reactions inside the tree-way catalyst.

## 2.3 Elementary steps of the CO oxidation reaction

The heterogeneous catalysed CO oxidation reaction on platinum group metals follows the Langmuir-Hinshelwood mechanism, which means that the reaction occurs between all reactants adsorbed on the catalyst surface<sup>3</sup>.

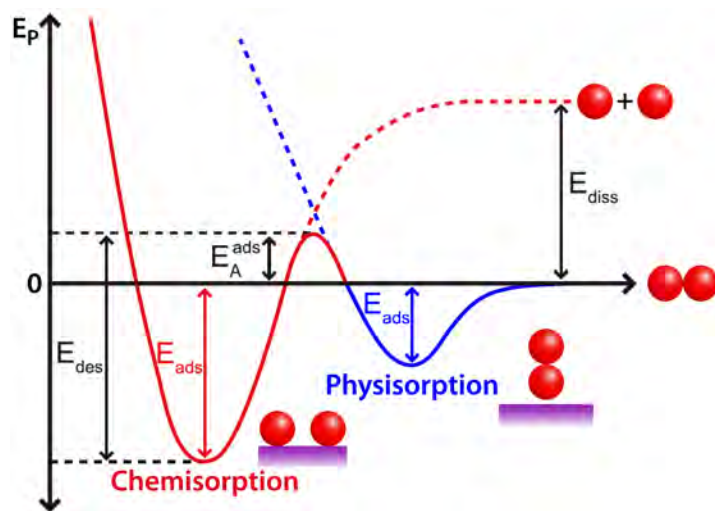


Fig. 2.2: Energy diagram of adsorption processes.

As shown in Fig. 1.3, the reaction can be described as the oxidation of adsorbed carbon monoxide ( $A$ ) by adsorbed atomic oxygen ( $B$ ) into carbon dioxide ( $AB$ ). The first step of an adsorption process is the approaching of a particle to the surface at a distance such that the van der Waals force between the particle and the surface becomes relevant. As a result, the particle is bonded quite weakly and reversibly to the surface. The bonding energy is usually smaller than  $0.4\text{ eV}$  per particle and therefore, only has negligible intra molecular effects on the adsorber. This phenomenon is called *physisorption* and can occur in nearly all solid-gas systems. In some systems already physisorbed particles can form chemical bonds between them and the surface after overcoming an additional activation energy  $E_A^{ads}$ . This process is called *chemisorption*. Chemisorbed particles have far higher binding energies that can be as high as  $2\text{ eV}$  per particle. If this high energy leads to an internal bond-breaking of the adsorbed molecules, as in the case of the oxygen adsorption process on platinum group metals, the adsorption process is known as *dissociative adsorption*. In the case of CO oxidation, molecular carbon monoxide and molecular oxy-

<sup>3</sup>The Langmuir-Hinshelwood mechanism is described in detail in Chapter 2.4 “The Langmuir-Hinshelwood mechanism of the CO oxidation reaction”.

## 2 CO oxidation reaction on platinum group metal

gen (which dissociates during the dissociative adsorption and is bonded to the surface as atomic oxygen) both adsorb on platinum group surfaces before they react with each other.

Adsorbed particles can desorb after the activation energy of desorption  $E_{des}$ , which is the sum of the adsorption energy  $E_A$  and the activation energy  $E_A^{ads}$ , has been introduced to the system.

The probability of adsorption after a particle collides with the surface is described by the sticking probability  $S$ , which is the quotient of the number of particles that adsorbed after their collision with the surface and the number of all collisions between particles and the surface, which could lead to an adsorption process.

$$S = \frac{N_{ads}}{N_{total \ number \ of \ collisions}} \quad (2.6)$$

The adsorption rate  $R_{ads}$  is defined as

$$R_{ads} = \frac{dN_{ads}}{dt} = S \cdot Z = \frac{S \cdot p}{2 \cdot \pi \cdot m \cdot k \cdot T} \quad (2.7)$$

where  $Z$  is the rate of the impinging particles, which is according to the kinetic gas theory given as  $Z = \frac{p}{\sqrt{2 \cdot \pi \cdot m \cdot k \cdot T}}$ , where  $p$  is the pressure,  $T$  is the temperature,  $k$  is the Boltzmann constant and  $m$  is the mass of the impinging particles.

The desorption rate  $R_{des}$  is, analogous to  $R_{ads}$ , defined as

$$R_{des} = -\frac{dN_{ads}}{dt}. \quad (2.8)$$

The relation between the covered and the uncovered sites on the surface can be described by the relative surface coverage  $\Theta$ , which is the quotient of the number  $N_{ads}$  of the adsorption sites where particles are already adsorbed and the number  $N_{max}$  of all existing adsorption sites of the surface. Taking eq. (2.7) into account  $\Theta$  is proportional to  $p$  and  $\frac{1}{T}$ .

$$\Theta = \frac{N_{ads}}{N_{max}} \quad (2.9)$$

Therefore,

$$N_{free} = N_{max} \cdot (1 - \Theta) \quad (2.10)$$

describes the number of all free adsorption sites of the surface.

## 2.4 The Langmuir-Hinchelwood mechanism of the CO oxidation reaction

The CO oxidation reaction on platinum group metals follows the Langmuir-Hinchelwood mechanism, which means that the reaction occurs between the reactants adsorbed on the catalyst surface.

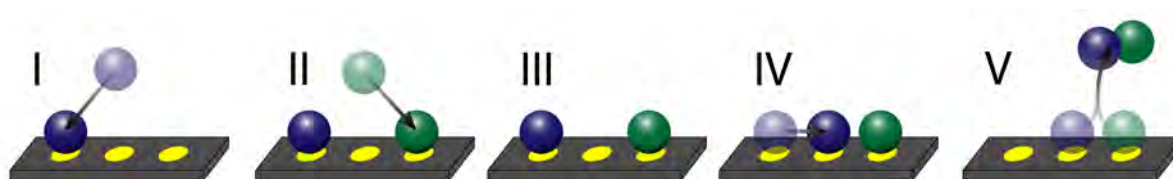


**Fig. 2.3:** Principle of the Langmuir Hinchelwood mechanism:

I:  $A$  adsorbs at the catalyst.

II:  $B$  adsorbs at the catalyst

III:  $A$  and  $B$  are adsorbed.

IV:  $A$  diffuses next to  $B$ .

V: After the reaction of  $A$  with  $B$   $AB$  desorbs.

The amount of carbon dioxide produced per time unit  $\frac{dR}{dt}$  depends on the reaction rate constant  $k$ , which is e.g. influenced by the rate of CO diffusion and the surface coverage of carbon monoxide and oxygen.

$$\frac{dR}{dt} = k \cdot \Theta_A \cdot \Theta_B \quad (2.12)$$

Carbon monoxide needs only one free adsorption site to adsorb on the catalytically active surface, while oxygen, contrary to carbon monoxide, needs two free adjacent adsorption sites to adsorb on the catalyst. This difference leads to different absorption behaviours of CO and oxygen which result in two possible steady states of the surface which differ in their catalytic reactivity<sup>4</sup>. The influence of the surface coverage of carbon dioxide on  $\Theta_{CO}$  and  $\Theta_{O_2}$ , and, therefore, also on  $\frac{dR}{dt}$  is negligible, because the binding energy of carbon dioxide to the catalytic surface is so small that  $CO_2$  desorbs almost immediately after its formation.

<sup>4</sup>For further information see chapter 2.5 “Bistability and the kinetic phase diagram”.

## 2 CO oxidation reaction on platinum group metal

The Langmuir-Hinshelwood mechanism of the CO oxidation reaction can be described as follows, with “\*” standing for a free adsorption site:

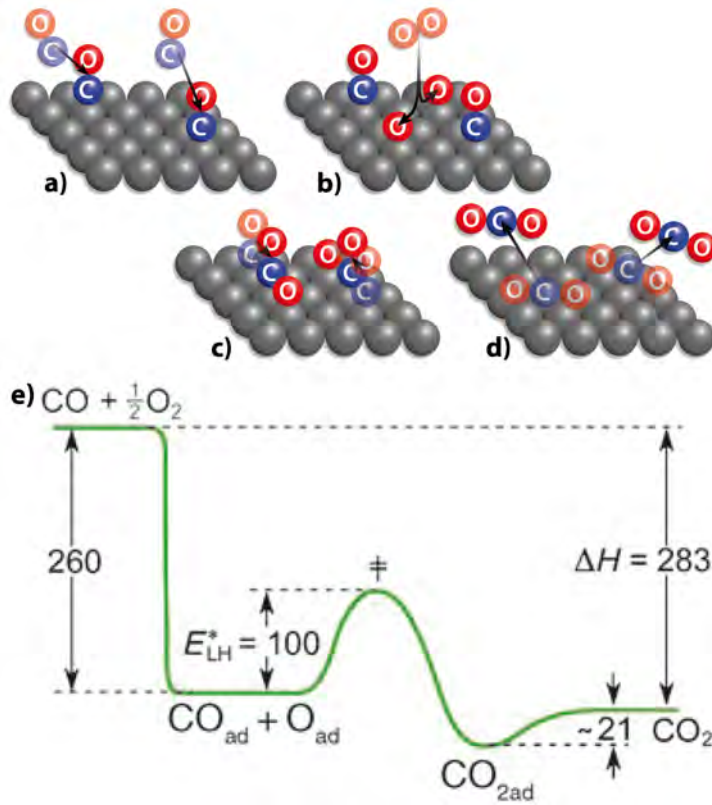
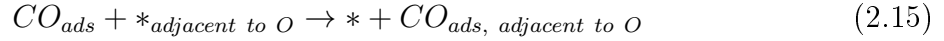
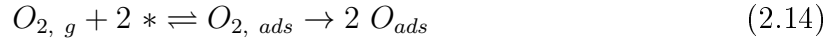


**Fig. 2.4:** Langmuir-Hinshelwood mechanism of the CO oxidation reaction and energy diagram of the CO oxidation reaction:

- a) CO adsorption at the catalyst.
- b) Dissociative adsorption of oxygen.
- c) Diffusion of CO to a free lattice site next to the bonded oxygen.
- d) Desorption of the CO<sub>2</sub> formed.
- e) Energy diagram of the CO oxidation reaction. (The diagram was taken from Ref. [7].)

## 2.5 Bistability and the kinetic phase diagram

If the surface is mainly covered with atomic oxygen, there are still some free adsorption sites between the adsorbed atomic oxygen, because molecular oxygen cannot adsorb on one single adsorption site. Contrary to molecular oxygen, molecular carbon monoxide can

## 2 CO oxidation reaction on platinum group metal

adsorb on one single free adsorption site and react with an adjacent bound atomic oxygen to carbon dioxide that desorbs immediately after its formation. Therefore, a catalytic surface covered mainly with atomic oxygen is catalytically active, i.e. it is in a *steady state of high reactivity*. If the surface is mainly covered with carbon dioxide, there can hardly be pairs of free adjacent adsorption sites. As a result, the adsorption of molecular oxygen is blocked by the densely adsorbed carbon monoxide and the CO oxidation reaction can hardly occur. This surface *poisoned* by carbon monoxide is in a *steady state of low reactivity*.

As shown in eq. (2.7) and eq. (2.9), the surface coverage of carbon monoxide and oxygen can be adjusted by changing the surface temperature and the partial pressures of both reactants. Therefore, it is possible to set well-defined reaction conditions at the beginning of an experiment that determine the steady state of the catalytic surface.

At the beginning of the experimental procedure which can be seen in Fig. 2.5, the catalytic surface is mainly covered with atomic oxygen due to the low carbon monoxide pressure, i.e. the sample is in the steady state of high reactivity. In this steady state an increase of the carbon monoxide pressure leads, in accordance with eq. (2.12), to a higher carbon monoxide adsorption rate.

At a certain temperature-related proportion of the partial carbon monoxide and the partial oxygen pressure, which is called transition point  $\tau_A$ , the sample switches into the steady state of low reactivity. Because all measurements performed within this thesis were arranged at constant partial oxygen pressures and at constant temperatures,  $\tau_A$  can be treated as partial carbon monoxide pressure.

At  $\tau_A$  the increased coverage of CO reaches a point at which the densely adsorbed carbon monoxide blocks the adsorption of oxygen. The already adsorbed atomic oxygen reacts with adsorbed carbon monoxide, whereupon the surface remains mainly CO-covered. Thus, the sample switches into the steady state of low reactivity, in which a further increase of partial CO pressure does not increase the CO<sub>2</sub> production rate any more.

If the partial CO pressure is reduced again to  $\tau_A$ , there are still not enough pairs of free adsorption sites for a significant increase of the oxygen adsorption rate. To increase the adsorption rate of oxygen significantly the partial CO pressure has to be reduced to the second transition point  $\tau_B$  (where the partial CO pressure is significant lower than at  $\tau_A$ ) at which the decreased carbon monoxide surface coverage enables the system to switch back into the mainly oxygen-covered steady state of high reactivity. Therefore, the plot of the reaction rate (Fig. 2.5) shows a hysteresis.

Between  $\tau_A$  and  $\tau_B$  the system shows a bistable behaviour: it can be either in the active

## 2 CO oxidation reaction on platinum group metal

or in the inactive state, depending on its prehistory.

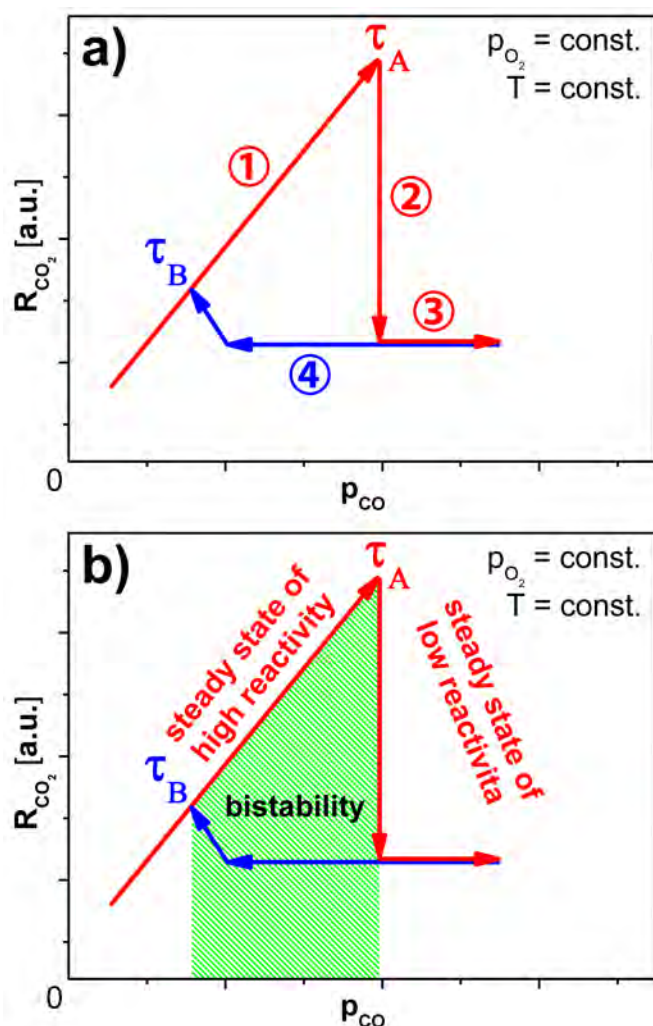


**Fig. 2.5:** Schema of the isobaric and isothermic hysteresis of the CO<sub>2</sub> production rate in the catalytic CO oxidation during cyclic variation of the CO pressure:

a) ① The surface starts as oxygen-covered. An increase of  $p_{CO}$  increases  $R_{CO_2}$ . ② At the transition point  $\tau_A$  the CO-coverage reaches a certain value at which CO blocks the adsorption of O<sub>2</sub>. As a result the CO<sub>2</sub> production rate decreases significantly. ③ Further increase of  $p_{CO}$  does not change the CO<sub>2</sub> production rate. ④ If  $p_{CO}$  is further reduced, the system reaches the second transition point  $\tau_B$ , at which the reduced CO-coverage enables the system to switch back to the oxygen-covered state.

b) Schematic explanation of the bistability behaviour: On the left hand side of  $\tau_B$  the sample is in the steady state of high reactivity. On the right hand side of  $\tau_A$  it is in the steady state of low reactivity. Between  $\tau_B$  and  $\tau_A$  it depends on the sample's prehistory whether it is in the steady state of high or in the steady state of low reactivity.

While the schematic plot of the carbon dioxide production rate shown in Fig. 2.5 illustrates the catalytic behaviour of the catalytic system at a certain constant temperature, a so-called *kinetic phase diagram* can characterize the catalytic behaviour of the catalyst at a certain temperature range. A kinetic phase diagram shows the two steady states and the bistability area of a catalyst at a certain partial oxygen pressure by combining the kinetic transition points  $\tau_A$  and  $\tau_B$  from hysteresis plots of the CO<sub>2</sub> production rate measured at different temperatures, as shown in Fig. 2.6.

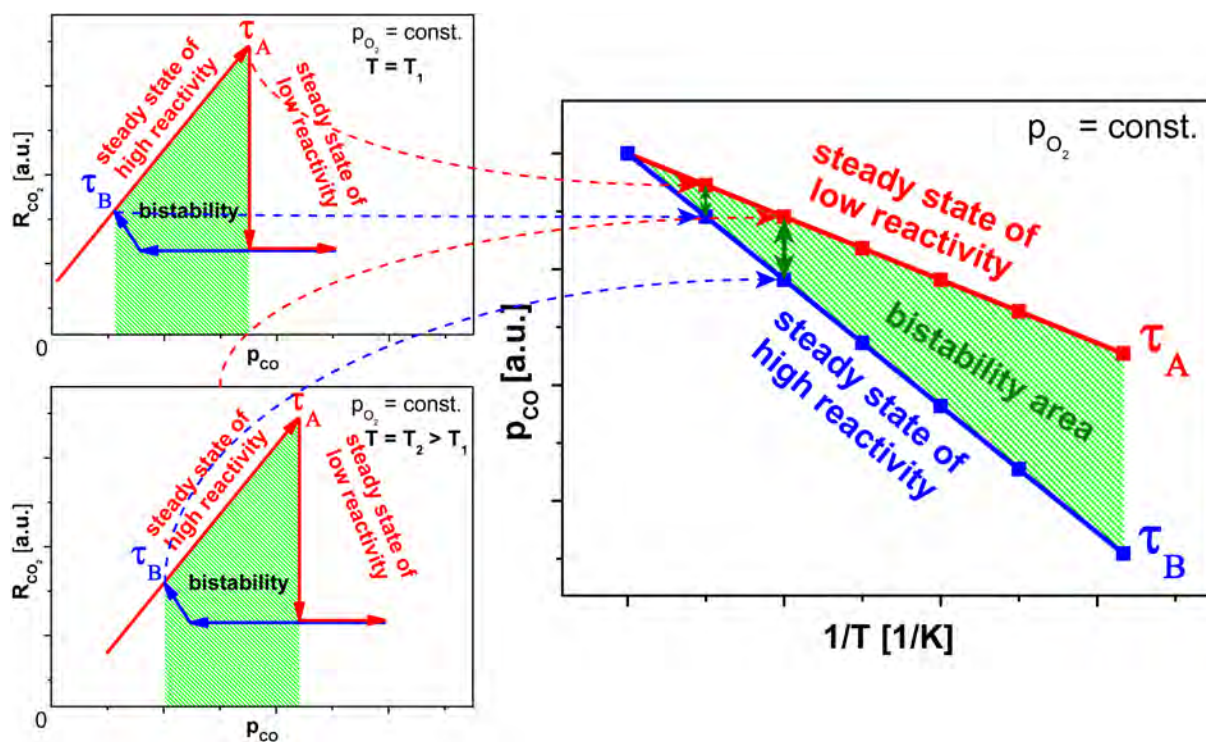


**Fig. 2.6:** Principle of the construction of a kinetic phase diagram:

A Kinetic phase diagram for a certain constant  $O_2$  pressure is deduced from the kinetic transition points  $\tau_A$  and  $\tau_B$  corresponding to the hysteresis plots of the  $CO_2$  production rate, measured at different temperatures.

# 3

## Experimental

---

### 3.1 The ultrahigh vacuum system

All experiments performed within this thesis were arranged in an ultrahigh vacuum (UHV) system with a base pressure of  $10^{-9}$  *mbar*. The UHV system consists of two separated chambers (XPS<sup>5</sup> chamber and PEEM<sup>6</sup> chamber) which are connected through the load lock. Therefore, it is possible to set nearly the same pressure conditions in the whole UHV system. Another advantage of the load lock is the possibility to place a new sample inside or to take an old sample out of the UHV system without breaking the vacuum in the two main chambers. The sample can also be transferred between the chambers and the load lock inside the UHV system by using a transfer rod.

The setup also makes it possible to change the four main parameters for the studied reaction: the catalytically active surface (sample), the partial gas pressures of the reactants and the temperature which can be set by heating the sample using either radiation heating or electron impact heating. The heating system in both manipulators allows rising the sample temperature to more than 1200 *K*.

---

<sup>5</sup>See chapter 3.2.1 “X-ray Photoelectron Spectroscopy”.

<sup>6</sup>See chapter 3.2.2 “Photoemission Electron Microscopy”.

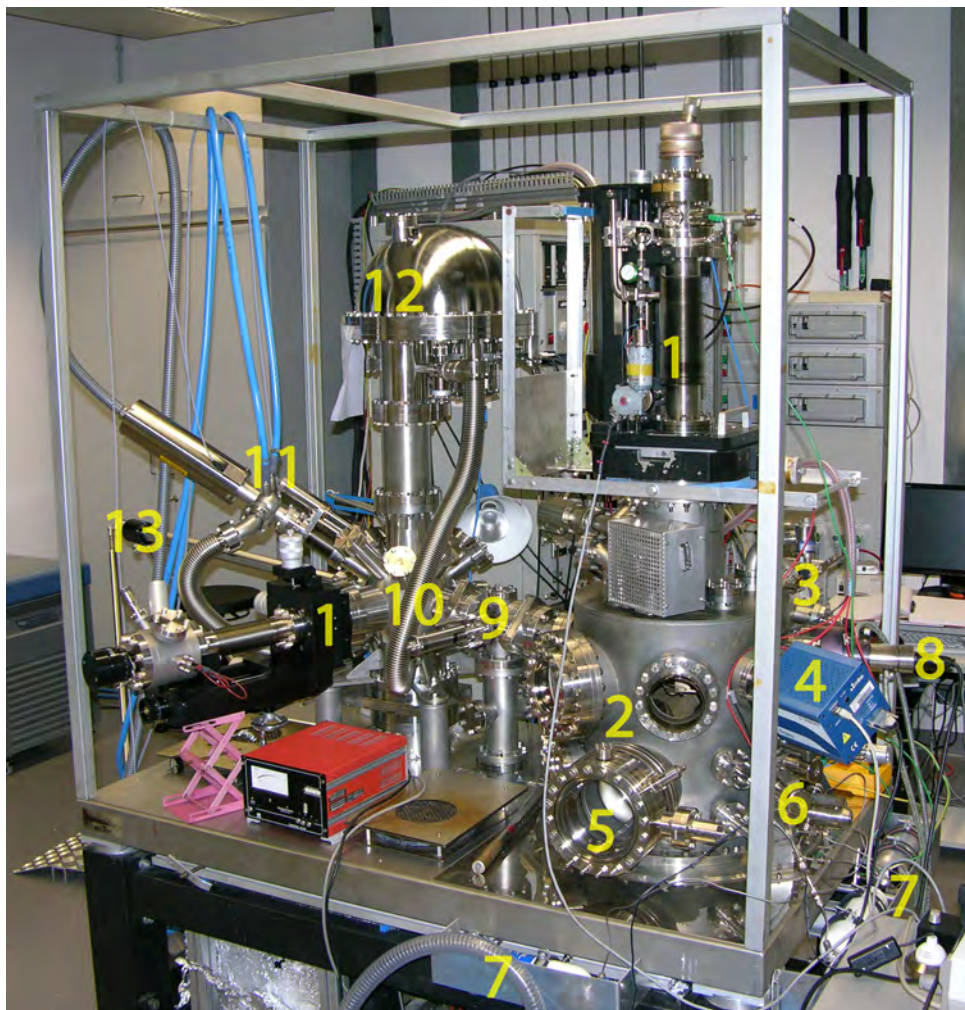


**Fig. 3.1:** The front of the experimental setup:

1 - manipulator; 2 - PEEM-chamber; 3 - PEEM; 4 - mass spectrometer; 5 - LEED; 6 - sputtergun and leak valves; 7 - gastanks; 8 - deuterium lamp; 9 - load lock; 10 - XPS-chamber; 11 - X-ray source; 12 - hemispherical electron energy analyser; 13 - transfer rod.

### 3.1.1 Vacuum pumps

The base pressure below  $10^{-8}$  mbar in the XPS chamber is provided by an ion getter pump (StarCell 300, Varian) and a titan sublimation pump (TSP, Varian). Additionally, the turbo molecular pump (HiPace 80, Pfeiffer Vacuum) that is connected to the load lock, whose fore-vacuum of  $10^{-2}$  to  $10^{-3}$  mbar is achieved by a rotary pump (Duo 5, Pfeiffer Vacuum), can pump the XPS chamber if the gate valve between the chamber and the load lock is open. Analogously the pumps of the PEEM chamber can pump up the XPS-chamber if the gate valve between the XPS chamber and the load lock and the gate valve between the load lock and the PEEM chamber are open.

### 3 Experimental

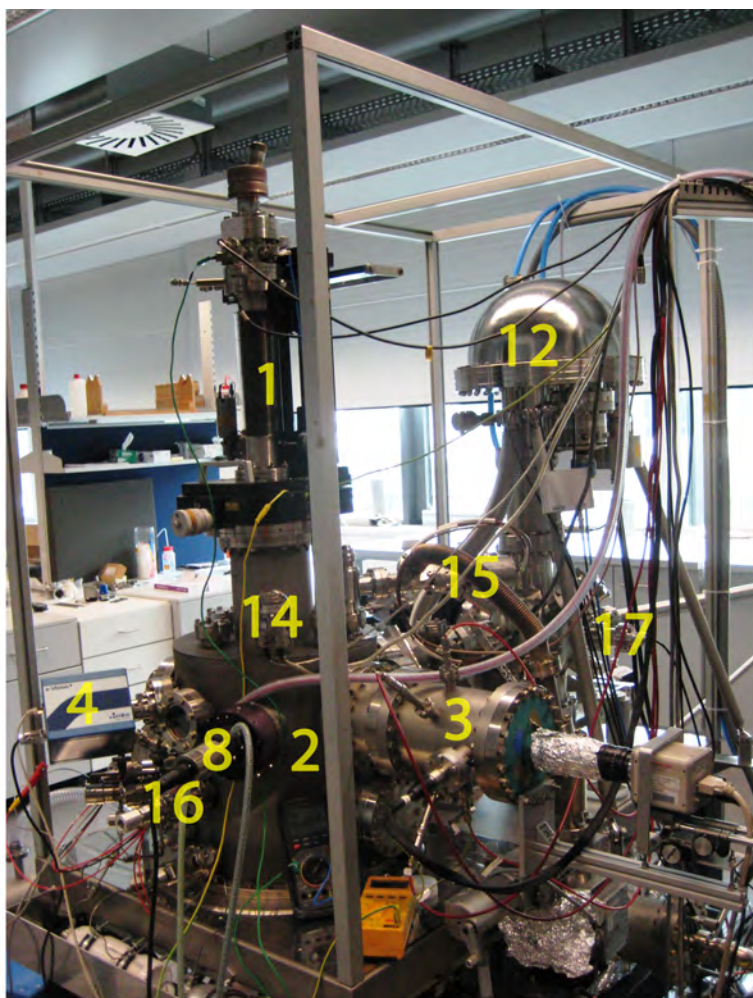


**Fig. 3.2:** Back of the experimental setup:

1 - manipulator; 2 - PEEM-chamber; 3 - PEEM; 8 - deuterium lamp; 12 - hemispherical electron energy analyser; 14 - spinning rotor manometer; 15 - Bayard-Alpert hot cathode ionization gauge; 16 - external temperature measurement; 17 - ionization gauge.

In the PEEM chamber the same base pressure is provided by an ion getter pump (VacIon Plus 500, Varian) and a turbo molecular pump (TMU 260, Balzers), whose fore-vacuum of  $10^{-2}$  to  $10^{-3}$  *mbar* is again provided by a rotary pump (TriVac D8B, Leybold). This pump also provides the fore-vacuum for the second turbo molecular pump (TMU 071P, Pfeiffer Vacuum) that is used for differential pumping of the PEEM chamber and the PEEM. Therefore, it is possible to increase the total pressure in the PEEM chamber up to  $10^{-4}$  *mbar* while the pressure in the PEEM does not exceed  $5 \cdot 10^{-7}$  *mbar*. A titan sublimation pump is also connected to the PEEM chamber, to avoid a contamination by

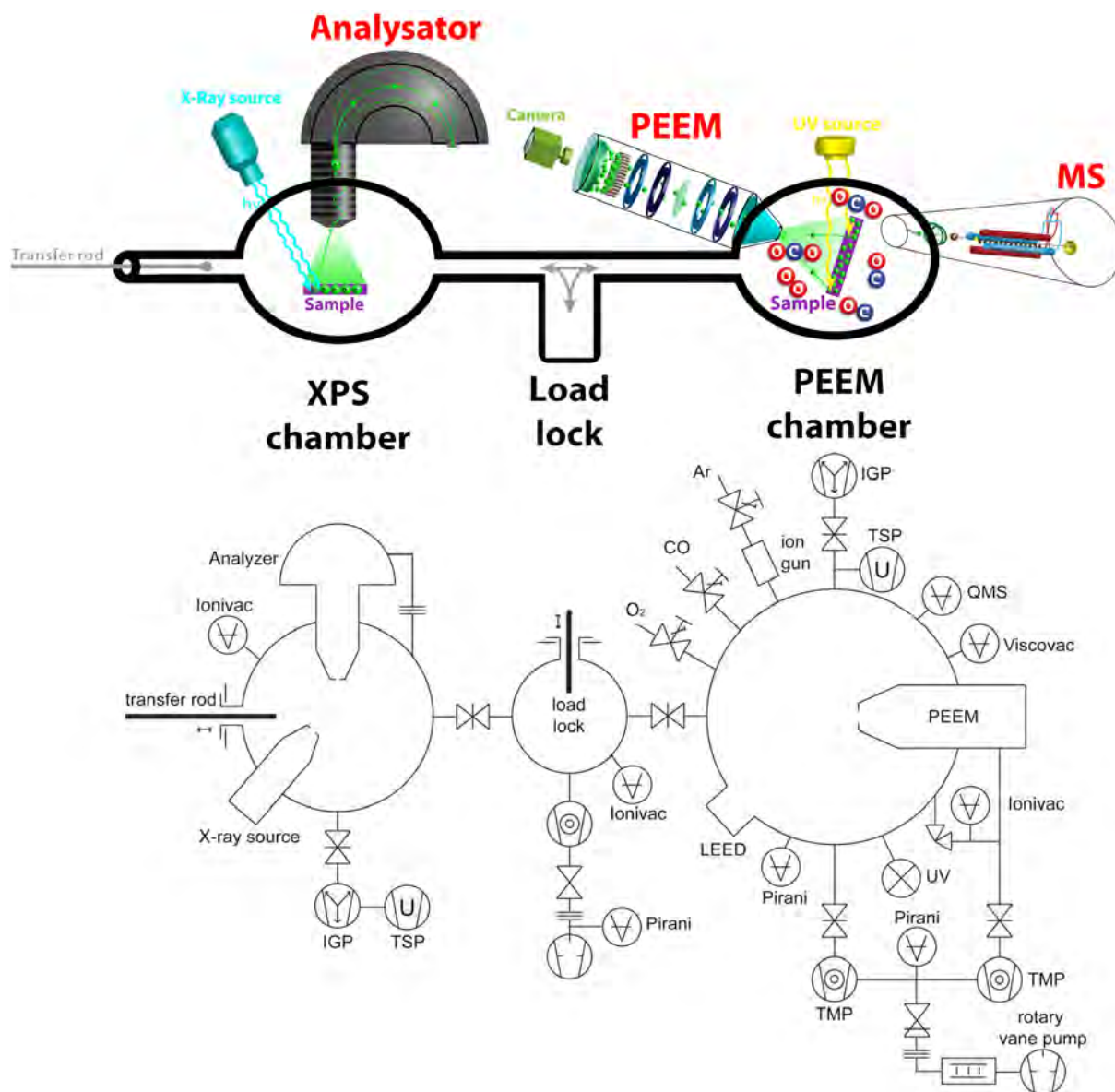


**Fig. 3.3:** Scheme of the experimental setup.

water which could hardly be pumped away by the turbo molecular and the ion getter pump.

### 3.1.2 Pressure measurement

An ionization gauge (MVC-3, Vacom) measures the pressure in the XPS chamber and in the load lock. The pressure in the PEEM chamber can be controlled by three different devices: the total pressure is monitored by the spinning rotor gauge (Viscovac, Leybold)

### 3 Experimental

and a Bayard-Alpert hot cathode ionization gauge (Varian) which also can measure the pressure inside the PEEM individually. The quadrupole mass spectrometer (e-Vision<sup>+</sup>, MKS Spectra Products) can measure the total pressure and the partial pressures inside the PEEM chamber at the same time. All fore-vacuums can be controlled by thermal conductivity Pirani gauges (ThermoVac, Leybold). Moreover, the pressure in the ion getter pumps is also measured indirectly by the ion current of the pumps.

#### 3.1.3 Gas inlets and ion sputter gun

Three gas cans (1 L MINICAN) are connected to the PEEM chamber by three leak valves (Balzers/Varian). This setup enables to set particular reaction conditions by dosing carbon monoxide (99,97%, Linde) and oxygen (99,999%, Messer Austria) into the PEEM chamber. The mounted Ar<sup>+</sup> ion sputter gun (IQE 11/35, SPECS) is used to sputter the surface of the sample. The argon flux is regulated by the leak valve that connects the argon can (99,999%, Messer Austria) to the sputter gun.

#### 3.1.4 Sample transfer

The sample can be transferred between the load lock and the two chambers by using the transfer rod. The transfer tool of the transfer rod can be connected to the transfer clutch of the sample holder plate by putting the tool over the clutch and locking it by turning the transfer rod by 90°. After the sample has been transferred to its final position (XPS chamber, PEEM chamber or load lock), the transfer tool is unlocked and the transfer rod can be disconnected.

#### 3.1.5 XPS chamber

The XPS chamber is equipped with an X-ray source (XR 50, SPECS), a hemispherical electron energy analyser (Phoibos 100, SPECS) and a manipulator (Standard LN2, SPECS) which is rotatable (360°), freely movable by 25 *mm* in direction x and y and freely movable by 100 *mm* in direction z.

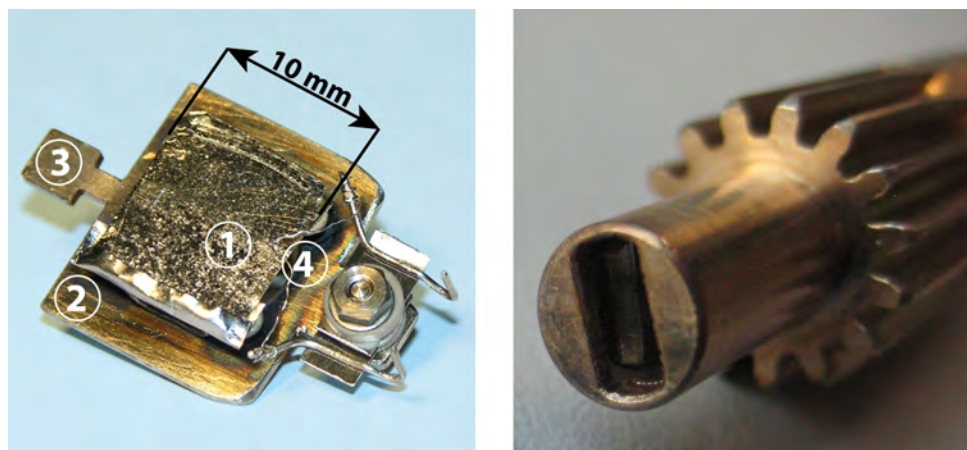


**Fig. 3.4:** Model system sample and transfer tool:

*Left:* The model system sample (impregnated Pd-powder into an  $\text{Al}_2\text{O}_3$ -foil, ①) is mounted onto the sample plate (②) containing a transfer clutch (③) and a NiCr/Ni type K thermo couple (④), which is spot-welded to the sample.

*Right:* Transfer tool.

### 3.1.6 PEEM chamber

The PEEM chamber is named after the mounted photoemission electron microscope (PEEM-150, STAIB Instruments) which is equipped with a water-cooled deuterium discharge UV lamp (D200, Heraeus) for providing the electron excitation<sup>7</sup>. The manipulator in the PEEM chamber is freely rotatable ( $360^\circ$ ), freely movable by  $\pm 25 \text{ mm}$  in direction x and y and freely movable by  $\pm 100 \text{ mm}$  in direction z. The sample holder can additionally be tilted by a few degrees to place the sample exactly parallel to the first lens of the PEEM lens system.

## 3.2 Methods

The data used in the present thesis were obtained by **X-ray Photoelectron Spectroscopy** (XPS), **Photoemission Electron Microscopy** (PEEM) and **Quadrupol Mass Spectrometry** (QMS).

<sup>7</sup>See chapter 3.2.2 “Photoemission Electron Microscopy”.

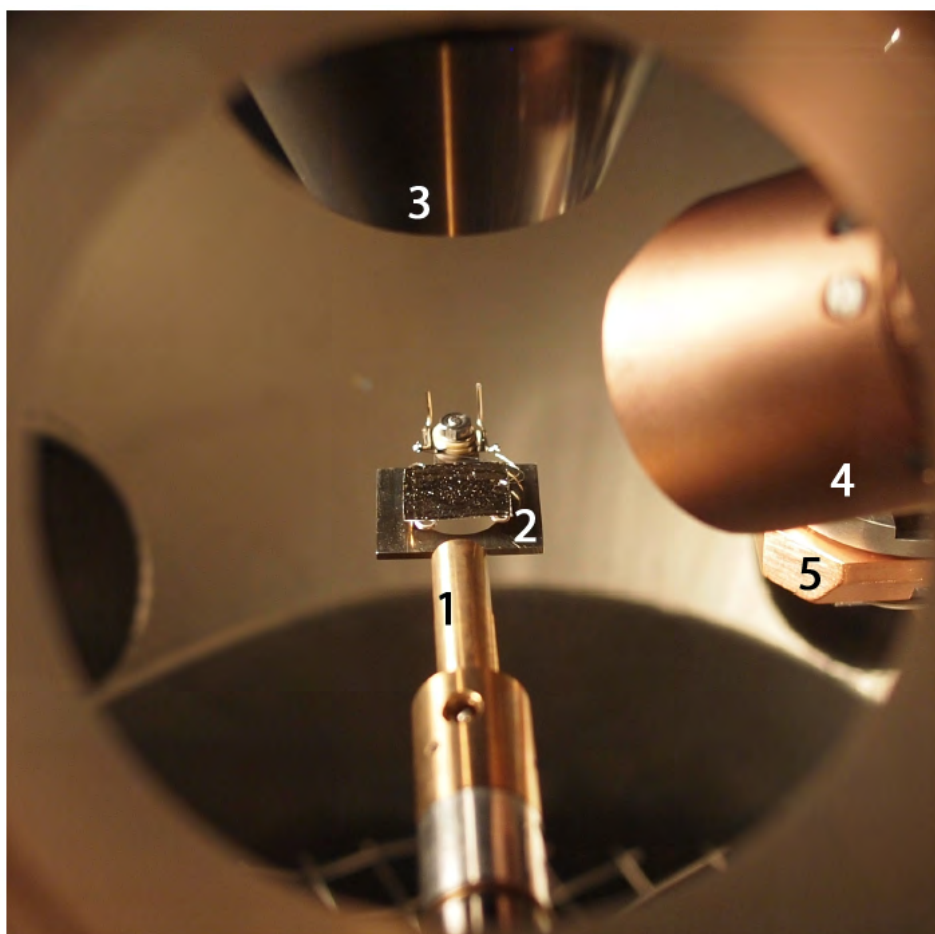


**Fig. 3.5:** View through a CF40 window into the XPS chamber:  
1 - transfer rod, 2 - sample, 3 - hemispherical electron energy analyser, 4 - XPS-source, 5 - manipulator.

### 3.2.1 X-ray Photoelectron Spectroscopy

As early as 1907, P. D. Innes recorded the first broad bands of photoelectrons which were emitted from an X-ray-illuminated metal sample due to the photoeffect<sup>8</sup>. After a significant improvement of the equipment, Kai Siegbahn could record the first high-energy-resolution XPS-spectrum in 1954 and thereby opened the way for XPS which is also known as **E**lectron **S**pectroscopy for **C**hemical **A**nalysis (ESCA). The X-rays are usually generated by a Mg-K $\alpha$ -source (1253.6 eV) or a Al-K $\alpha$ -source (1486.6 eV) which was also used in the present thesis. The kinetic energy of the photoelectrons which are emitted by the sample due to the photoeffect<sup>9</sup> is analysed by an energy analyser

<sup>8</sup>See chapter 3.2.1.1 “The photoeffect”.

<sup>9</sup>See chapter 3.2.1.1 “The photoeffect”.

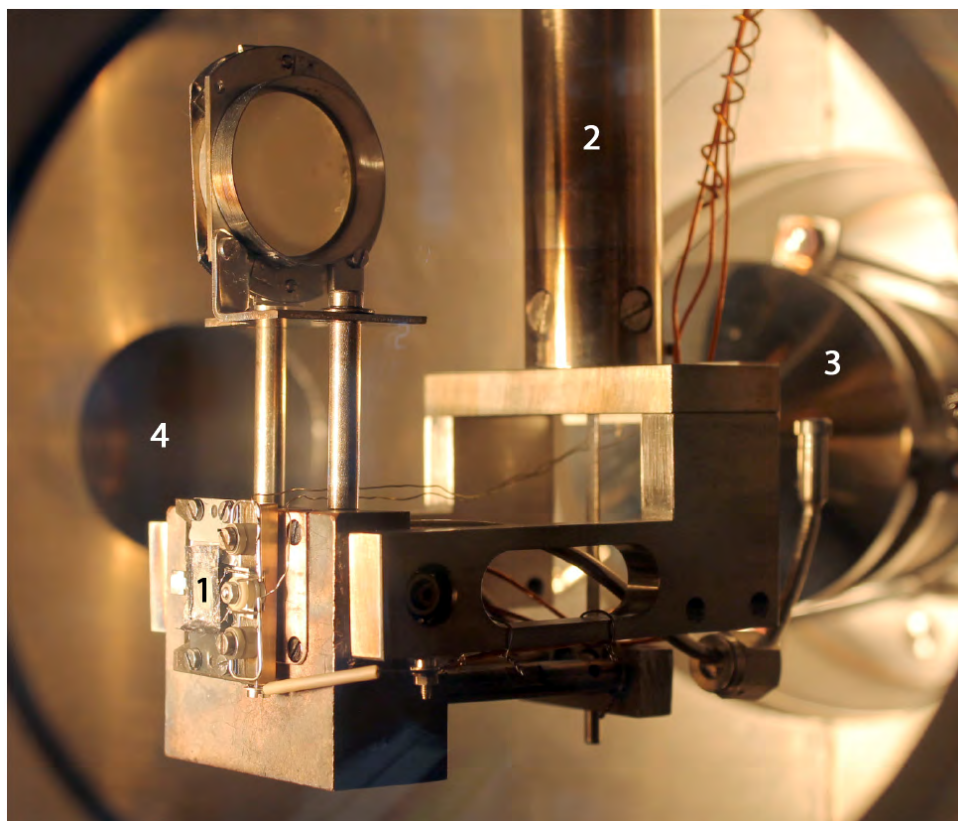


**Fig. 3.6:** View through a CF40 window into the PEEM-chamber:  
1 - sample, 2 - manipulator, 3 PEEM, 4 - flange to the load lock.

in order to evaluate their binding energy<sup>10</sup>. As the binding energy of a photoelectron corresponds to a specific atomic orbital, XPS can evaluate qualitative information about the composition of the sample<sup>11</sup>. Furthermore, the area of the detected peaks contains quantitative information about the occurrence of a certain species in the sample<sup>12</sup>.

### 3.2.1.1 The photoeffect

Hertz and Hallwachs detected in 1887 that the illumination by electromagnetic radiation, such as UV-light, of a metal sample can lead to the emission of photoelectrons. Nearly

<sup>10</sup>See chapter 3.2.1.2 “Principle of the electron energy analysis”.

<sup>11</sup>See chapter 3.2.1.5 “The XPS-spectrum”.

<sup>12</sup>See chapter 3.2.1.5 “The XPS-spectrum”.

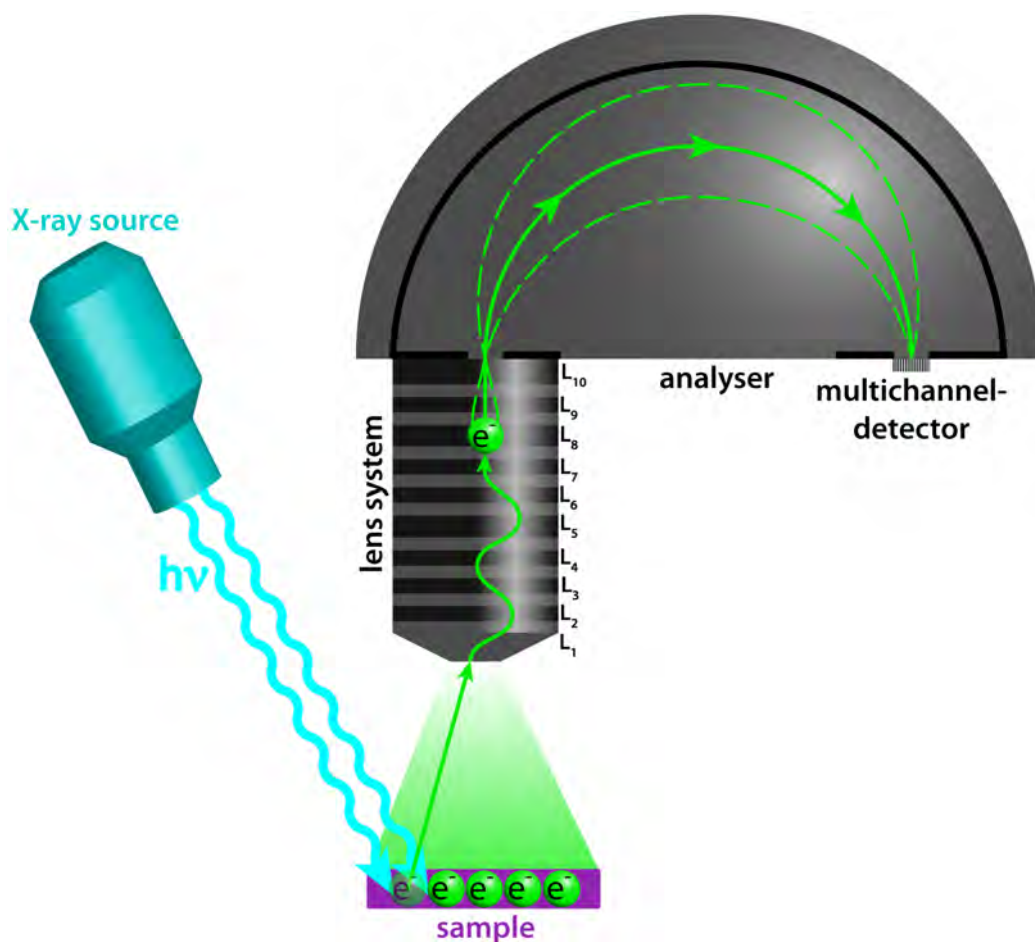


**Fig. 3.7:** Working principle of an XPS:

The sample emits photoelectrons due to illumination by X-rays. The kinetic energy of these photoelectrons is measured by an energy analyser in order to calculate their initial binding energy which contains chemical information about the sample. The different parts and the working principle of the energy analyser are described in Chapter 3.2.1.4 “Hemispherical Electron Energy Analyser”.

thirty years later Einstein explained the photoeffect and was honoured for his thesis with the Nobel Prize in 1922. The central equation of Einstein’s thesis is

$$E_{kin} = h\nu - \Phi - E_B \quad (3.1)$$

with  $E_{kin}$  standing for the kinetic energy of the photoelectron,  $h\nu$  for the energy of the electromagnetic radiation,  $\Phi$  for the local work function of the sample and  $E_B$  for the binding energy of the photoelectron. The work function is different for each element and also related to different surface properties like the crystallographic orientation of the surface or adsorbates.

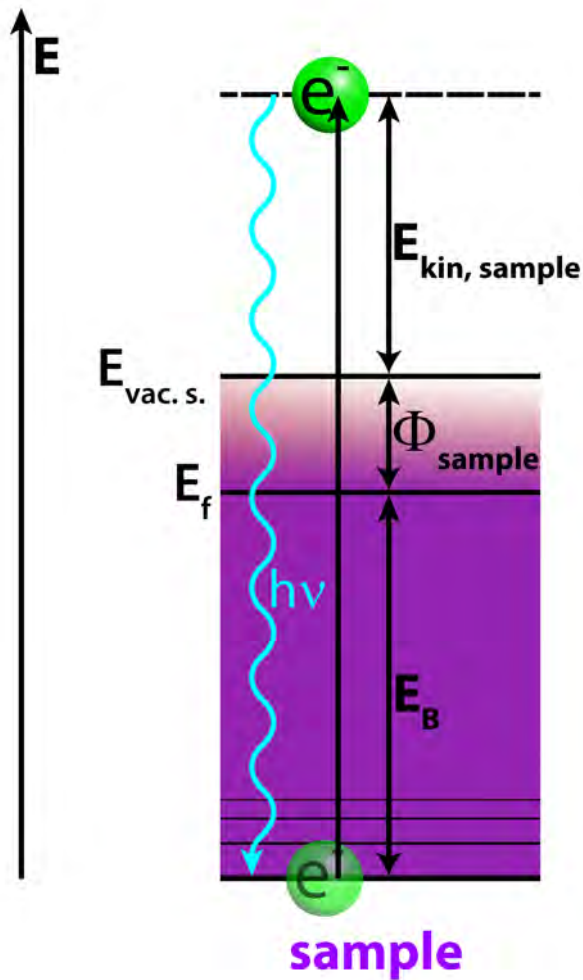


**Fig. 3.8:** Energy diagram of the photoeffect:  $E_{kin, sample}$  is the kinetic energy of the photoelectron emitted,  $E_{vac. s.}$  the vacuum level of the sample,  $h\nu$  the energy of the electromagnetic radiation,  $E_f$  the fermi level,  $\Phi_{sample}$  the work function of the sample and  $E_B$  the binding energy of the electron.

If a core electron is emitted from the sample, it leaves a vacancy behind which can be filled by an electron from a higher energetic level. The energy difference between its old and its new energy level is emitted as X-ray fluorescence which can be detected by an external detector or absorbed by another electron of the atom. If this absorption leads to the emission of the second electron, the emitted electron is called Auger electron. While the kinetic energy of photoelectrons is related to the energy of the irradiated radiation, the kinetic energy of the Auger electrons is independent from external conditions.

Auger electrons are named after the electron shells the first and the third electron are emitted from and the second electron had his origin in. If e.g. the first electron was emitted from the K shell, the second initial stayed in the L shell and the third is emitted from the M shell, the Auger electron is called KLM Auger electron.

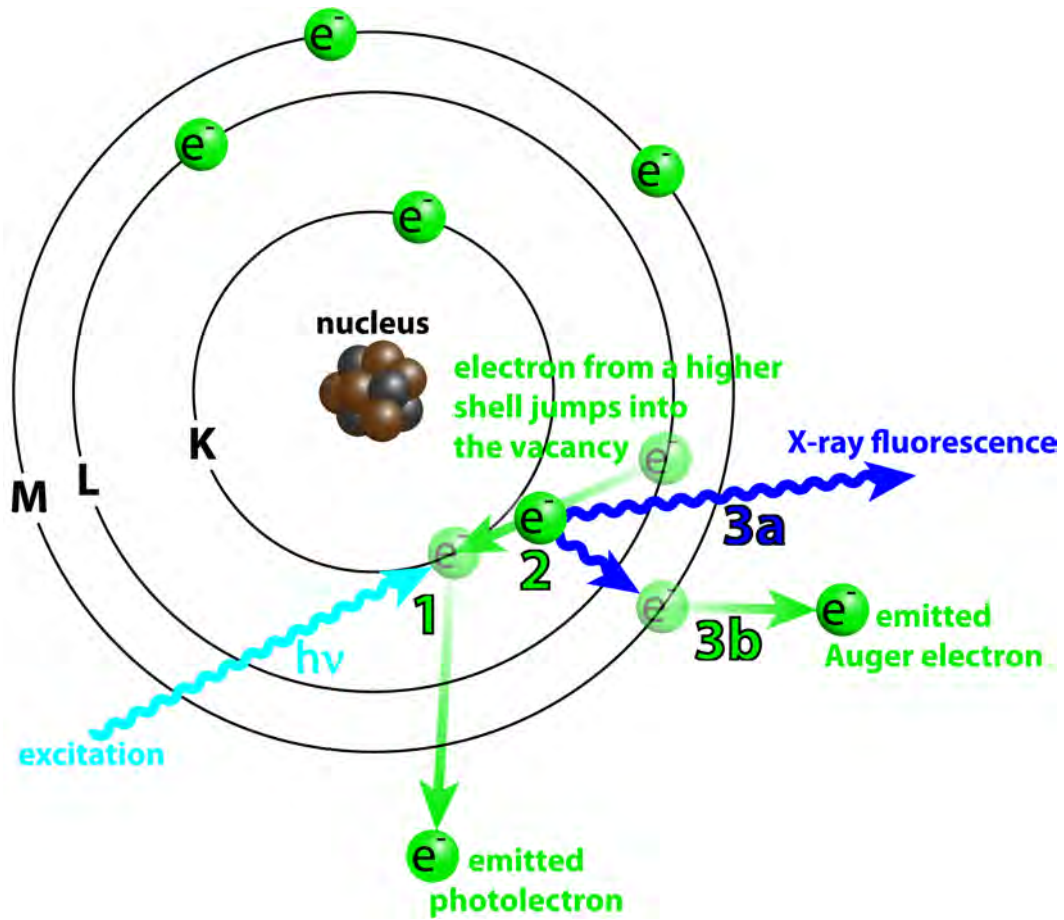


**Fig. 3.9:** Principle of the emission of a characteristic X-ray photon (3a) or a KLM-Auger-electron (3b).

### 3.2.1.2 Principle of the electron energy analysis

After a photoelectron is emitted from the sample, it has, according to eq. (3.1), the kinetic energy  $E_{Kin, sample}$ .

$$E_{Kin, sample} = h\nu - \Phi_{sample} - E_B. \quad (3.2)$$

Therefore, the binding energy can be obtained if  $E_{Kin, sample}$  and  $\Phi_{sample}$  are measured while keeping  $h\nu$  at a known constant value. While the kinetic energy of photoelectrons can be measured easily by a proper energy analyser, measuring the work function is quite difficult.

For the explanation of the working principle of an energy analyser, it is necessary to elucidate the Volta effect which describes the phenomenon that two metals with different work function values equal their fermi levels, if they are connected with an electrical

### 3 Experimental

conductor. In the following it will be shown that the energy analyser can determine the initial binding energy of the photoelectrons without knowledge about the work function of the sample, since the energy analyser and the sample are connected by an electrical conductor.

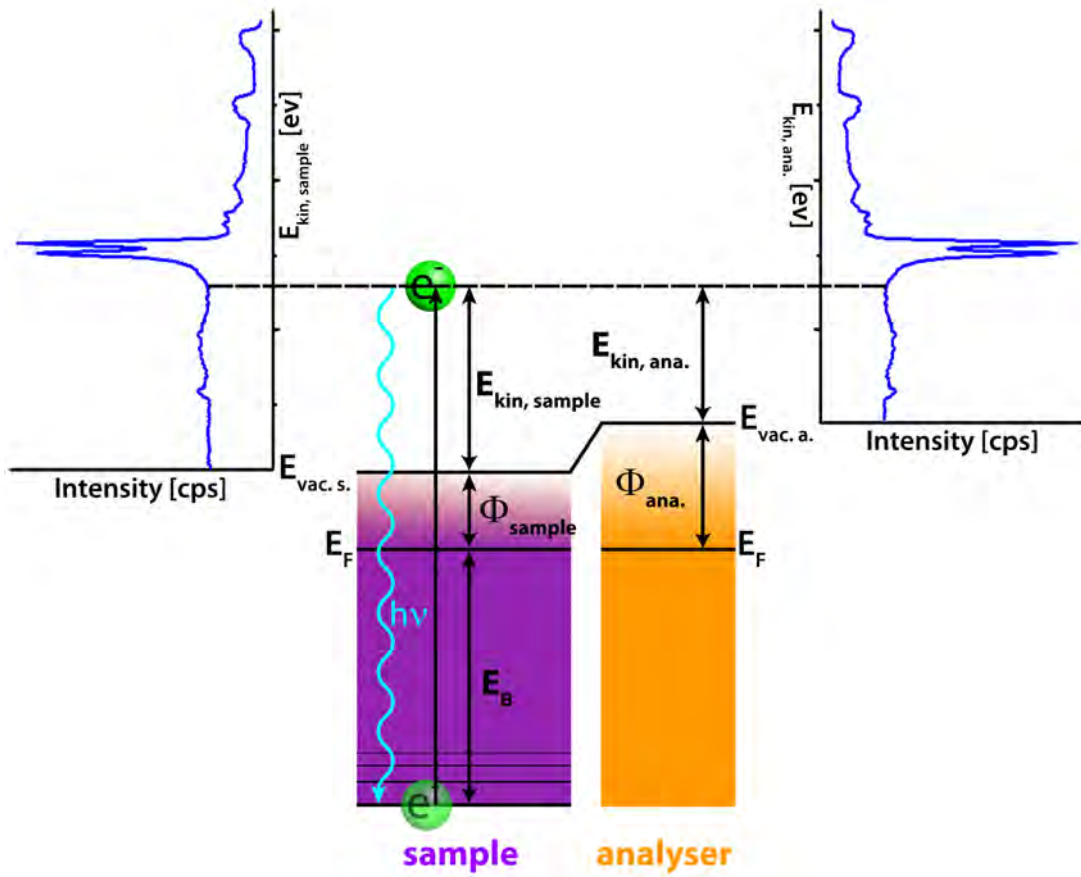


**Fig. 3.10:** Working principle of an XPS-analyser:  
Due to the Volta effect, the fermi levels of the sample and the analyser are equal.

While the photoelectrons fly from the sample to the spectrometer, their kinetic energy changes due to the contact potential between the sample and the analyser, which leads to the independence of  $E_B$  from  $\Phi_{sample}$ .

$$E_{Kin, Ana.} = h\nu - \Phi_{sample} - E_B - (\Phi_{Ana.} - \Phi_{sample}) \quad (3.3)$$

$$E_{Kin, Ana.} = h\nu - E_B - \Phi_{Ana.} \quad (3.4)$$

$$E_B = h\nu - E_{Kin, Ana.} - \Phi_{Ana.} \quad (3.5)$$

### 3 Experimental

Thus the binding energy of the photoelectrons can be calculated if the energy analyser measures  $E_{Kin, Ana.}$  and the work function of the analyser and the excitation energy are known.

#### 3.2.1.3 The surface sensitivity of XPS

The reason for the surface sensitivity of XPS is the short inelastic mean free path  $\lambda$  of electrons inside the metal sample. Some electrons that lost too much kinetic energy in inelastic collisions, might not have enough energy to be emitted from the sample, while other electrons might still have enough energy to be emitted and reach the detector. These inelastically scattered photoelectrons result in the *background*<sup>13</sup> of XPS-measurements, which contains no information about the sample. The relation between  $\lambda$  and the kinetic energy of the electrons is described by the *universal curve*, which shows its minimum for most metals at electron energies between 15 and 150 eV. As shown in Fig. 3.11, the mean free path of electrons inside a metal bulk lies between 0.5 and 2 nm.

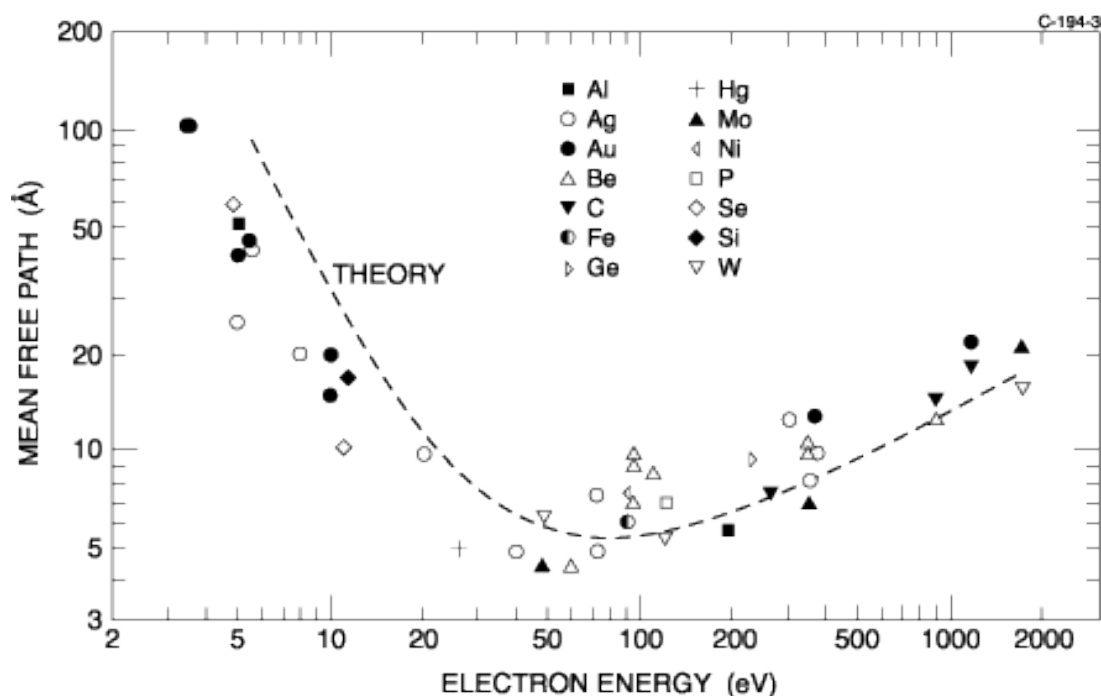


**Fig. 3.11:** The universal curve from Ref. [8]:  
Theoretical calculations of the mean free path in comparison with experimental results.

<sup>13</sup>See chapter 3.2.1.5 “The XPS-spectrum”.

### 3 Experimental

The probability  $P$  of an electron to emit from a depth  $d$  can be calculated by the equation

$$P(d) = e^{-\frac{d}{\lambda}}. \quad (3.6)$$

Therefore, approximately 63% of emitted photoelectrons originate from a depth  $d < \lambda$ , circa 86% from a depth  $d < 2 \cdot \lambda$  and nearly 95% from a depth  $d < 3 \cdot \lambda$ . This means, that almost 95% of the information contained by an XPS-spectrum refers to the first 20 layers of the sample.

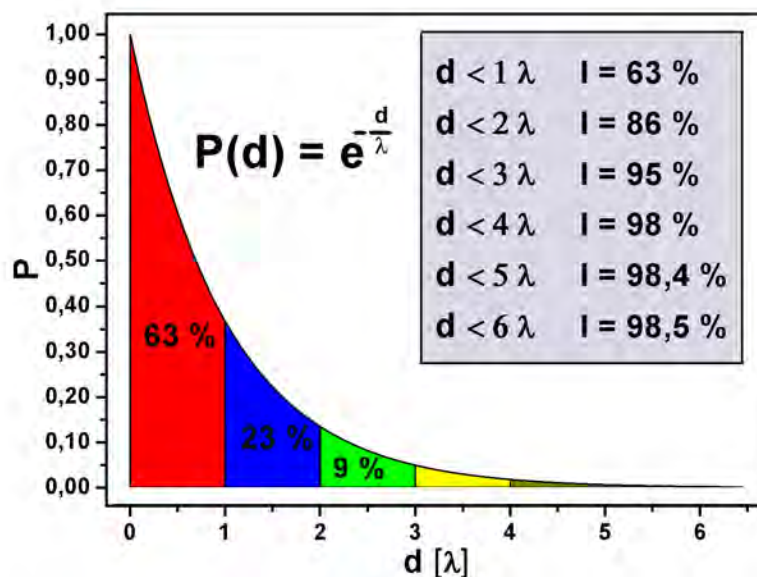


**Fig. 3.12:** Relation between the number of photo electrons emitted from a metal, their mean free path and their depth.

There are two possibilities to make XPS even more surface sensitive or to measure a depth profile of the sample: the *variation of the excitation energy* and the *angle resolved XPS*. By modifying the excitation energy also the kinetic energy and the mean free path of the electrons inside the sample can be modified according to eq. (3.1) and Fig. 3.11. Taking eq. (3.6) into account, also the information depth is influenced by this variation. Alternatively, one can use angle resolved XPS as illustrated in Fig. 3.13. By tilting the

### 3 Experimental

sample by a certain angle  $\varphi$  with respect to the analyser, the information depth  $d$  decreases to the effective information depth  $d^*$ .

$$d^* = \lambda \cdot \cos(\varphi) \quad (3.7)$$

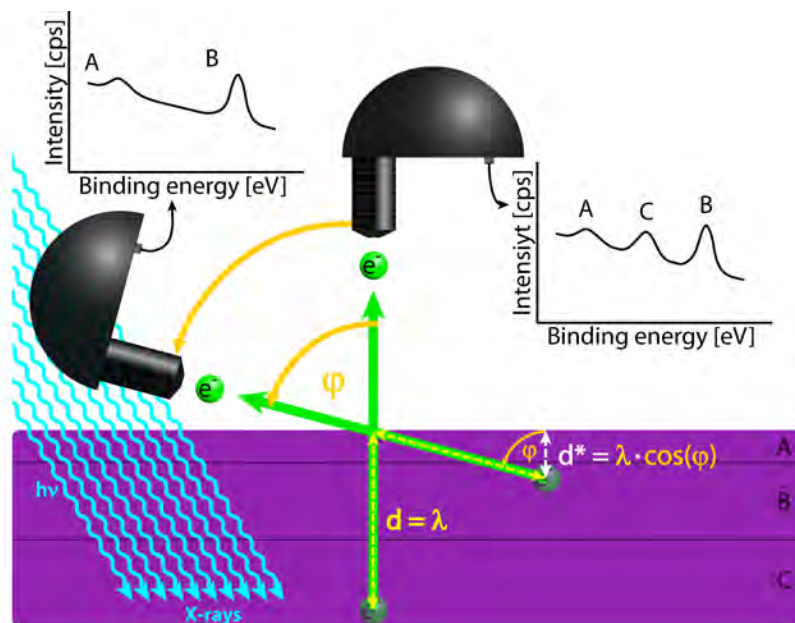


**Fig. 3.13:** Angle-resolved XPS:

The tilting angle  $\varphi$  between the analyser and the sample leads to an increase of the surface sensitivity, because the information depth  $d$  decreases to  $d^*$ . Therefore, the peak, which corresponds to the layer C in the graph, disappears after the tilting.

#### 3.2.1.4 Hemispherical Electron Energy Analyser

Due to their different initial binding energies photoelectrons have different kinetic energies, even if they were illuminated by the same source. An energy analyser counts the number of photoelectrons emitted from a certain region of the sample with a predefined kinetic energy to gain information about the investigated area.

Emitted photoelectrons enter the energy analyser through a complex lens system<sup>14</sup>, which performs three tasks:

<sup>14</sup>The lens system of the energy analyser that was used for all measurements in the present thesis, consists of ten lenses.

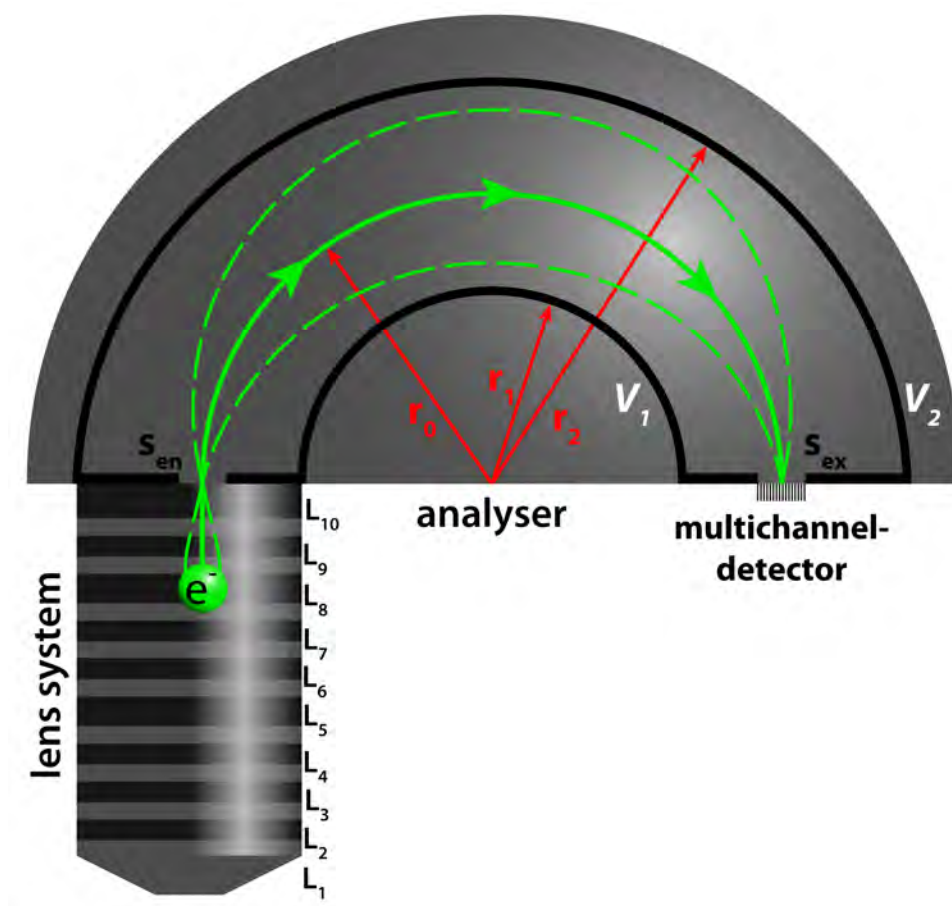


**Fig. 3.14:** Schematic cross section of a Hemispherical Electron Energy Analyser: The scheme includes the lenses of the lens system ( $L_1 - L_{10}$ ), the entrance slit  $S_{en}$ , the spherical capacitor with radii  $r_1$  and  $r_2$ , to which the voltages  $V_1$  and  $V_2$  are applied, the nearly semicircular trajectory of the electrons, whose kinetic energy is close to the *pass energy*, the exit slit  $S_{ex}$  and the multichannel-detector.

1. Adjusting the investigated region photoelectrons have to be emitted from in order to reach the detector.
2. Focusing the beam of photoelectrons on the entrance slit  $S_{en}$  which the photoelectrons have to pass to enter the hemispherical analyser.
3. Accelerating or slowing down all photoelectrons. Only those photoelectrons that had a certain velocity when they entered the lens system will enter the hemispherical analyser with the set *pass energy*. Photoelectrons that have a different kinetic energy than the pass energy cannot reach the detector. If the acceleration voltage is changed, only photoelectrons that enter the lens system with a certain different velocity, will enter the analyser having the *pass energy*.

### 3 Experimental

When the photoelectrons pass the entrance slit they enter a constant electrostatic field that is created by the spherical capacitor with radii  $r_1$  and  $r_2$  to which the voltages  $V_1$  and  $V_2$  are applied. This field deflects the photoelectrons whose kinetic energy is close to the pass energy, along a semicircular flight path with the radius  $r_0$  to the exit slit  $S_{ex}$ . The photoelectrons that pass the exit slit are detected by the multichannel-detector, while the electrons whose kinetic energy differs too much from the pass energy collide with the spherical capacitor.

Therefore, the energy analyser can measure the kinetic energy distribution of the photoelectrons (which is related to the initial binding energy distribution) that are emitted from a certain region of the sample by variation of the acceleration voltage of the lens system. As a result, the analyser can measure the binding energies with nearly constant energy resolution, because all photoelectrons reach the detector with approximately the same kinetic energy.

#### 3.2.1.5 The XPS-spectrum

The plot of the kinetic energy distribution for the emitted photoelectrons (counts per second against the kinetic energy) is called XPS-spectrum. Because each occurring peak corresponds to a certain orbital of an element, the XPS-spectrum can be used to analyse the sample after the spectrum has been calibrated using the Fermi edge or some known peak.

Beside the main peaks from the atomic orbitals in the XPS-spectrum, like Pd 3s, Pd 3p, Pd 3d, Pd 4s and Pd 4p (see Fig. 3.15), additional peaks occur for several reasons. Four types of them shall be mentioned in this thesis:

- Peaks of *Auger electrons* (see chapter 3.2.1.1 “The photoeffect”) occur above approximately 1000 eV. They can be clearly identified because their peaks cannot be shifted by changing the excitation energy.
- If the excitation source is non-monochromatic, the radiation consists of one characteristic line and several minor compounds at higher photon energies. These additional lines lead to so-called *X-ray satellite peaks* which are always shifted towards lower binding energies. The intensity of the shifted peak and the amount of the shift which is identical for all peaks in the spectrum is source depending and can therefore, be prognosticated.

### 3 Experimental

- If a photoelectron excites another electron of its atom during its emission process, the kinetic energy of the photoelectron is reduced by the energy difference of the second atom's excited state and its basic state. The reduced kinetic energy of the photoelectron leads to the so-called *shake-up lines* which occur at higher binding energies than the main peaks.
- If inelastically scattered photoelectrons leave the sample, their reduced energy leads to an increase of the XPS-signal at higher binding energies than the binding energy of the orbital the photoelectron was emitted from. This increase is called *background*.

Peaks corresponding to atomic orbitals with an angular momentum quantum number  $l \neq 0$  (i.e., p, d, f) are split up into two peaks due to their spin-orbit coupling. The total angular momentum  $j$  is the sum of  $l$  and the spin momentum quantum number  $s$ , which is  $\pm\frac{1}{2}$ . Therefore, most orbitals have two different energy states with different probabilities of occupancy which can be described by the multiplicity  $M$ .

$$M = 2 \cdot j + 1. \quad (3.8)$$

In the case of the p-state ( $l = 1$ ,  $s = \pm\frac{1}{2}$ ) the total angular momentum  $j$  can either be  $\frac{1}{2}$  or  $\frac{3}{2}$ , while the corresponding multiplicities result in 2 and 4. Therefore, the ratio of the peak areas of  $p_{1/2}$  to  $p_{3/2}$  is 4 : 2 respectively 2 : 1. An example of the split 3p peak can be seen in Fig. 3.15c. Analogously, the peak areas of  $d_{3/2}$  and  $d_{5/2}$  split up at a ratio of 2 : 3 while the areas of  $f_{5/2}$  and  $f_{7/2}$  divide up at a ratio of 3 : 4.

The binding energy of core electrons is also related to the chemical surrounding of the atom. Thus, modifications of the chemical surrounding, e.g. the forming of new bonds or a change of the oxidation state or adsorbates can be seen in the XPS-spectrum by a *chemical shift* of the corresponding peaks. If for example two atoms form a new bond, the valence electrons of the less electronegatively charged partner will be drawn closer to the more electronegatively charged partner. In the case of an oxidation process, the valence electrons of the oxidised reagent which are part of the new atom binding will move closer to the newly bound oxygen. Due to the increased spacing between the valence electrons of the oxidised reagent and its nucleus, the shielding-effect of these valence electrons decreases. As a consequence core electrons of the oxidised reagent experience an increased effective nuclear charge which causes their peaks to shift to higher binding energies. Analogously, the transition of the valence electrons leads to a reduced effective nuclear charge of the oxygen nucleus which also results in a peak shift to lower binding energies of the oxygen peak. If a sample is only partly oxidised or if different oxidation states occur, the peak is

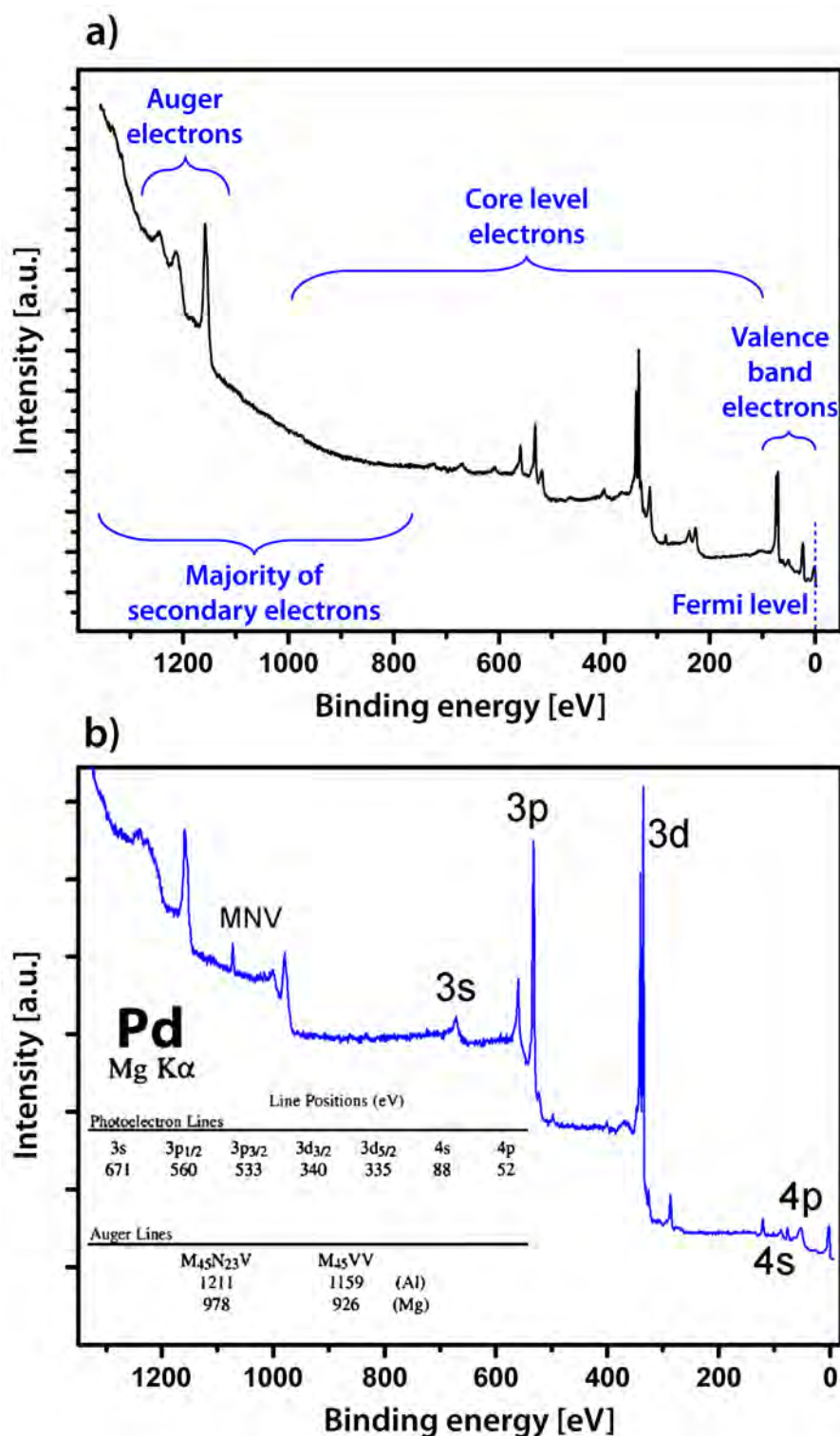


**Fig. 3.15:** The XPS-spectrum:  
a) General structure of the XPS-spectrum. Although the majority of the emitted photoelectrons are inelastically scattered secondary electrons with a low kinetic energy, only the core level electrons provide chemical information about the sample.  
b) XPS-spectrum of palladium. The Al-K $\alpha$  anode does not provide sufficient energy to initiate the emission of photoelectrons from Pd 1s, Pd 2s and Pd 2p.

fitted with several smaller peaks. These peaks can be compared and evaluated to archive the requested quantitative information.

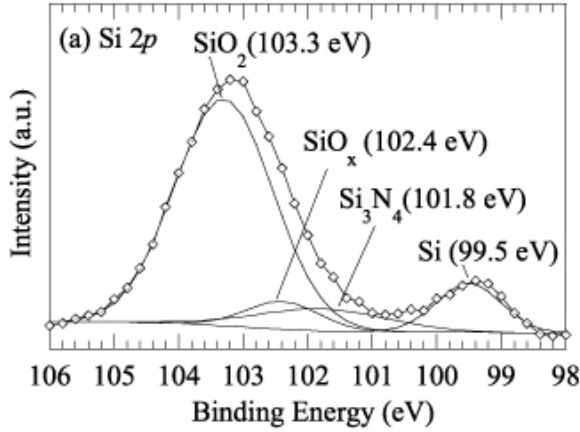


**Fig. 3.16:** Example of chemical shifts for different oxidation states of Si and for Si<sub>3</sub>N<sub>4</sub> from Ref. [2]. The measured signal was fitted with four different peaks.

The quantitative information about the occurrence of certain species in the sample can be evaluated by analysing the area and the height of the detected peaks. Besides the properties of the studied peak, also the sensitivity factor  $SF$  has to be considered for a scientific evaluation. The sensitivity factor is related to the phenomenon that the probability of emitting a photoelectron varies for different atomic orbitals. The sensitivity factor  $SF$  is defined as

$$SF = f \cdot \sigma \cdot \varphi \cdot \lambda \cdot A \cdot T \quad (3.9)$$

with  $f[\frac{\text{photons}}{\text{cm}^2 \cdot \text{s}}]$  standing for the photon flux,  $\sigma [\text{cm}^2]$  for the atomic cross section of the adsorption of a photon by the orbital,  $\varphi$  for the tilting angle between the analyser axis and the sample,  $\lambda$  for the mean free path of the photoelectrons in the sample,  $A$  for the illuminated area of the sample and  $T$  meaning the detector sensitivity.

Further the equation

$$n = \frac{I}{SF} \quad (3.10)$$

with  $I$  meaning the measured intensity can be used for evaluating the real number of atoms from a certain species within the area studied  $n [\text{cm}^{-3}]$ .

### 3.2.2 Photoemission Electron Microscopy

Although the first photoemission electron microscope (PEEM) was developed in the early 1930s [9], its scientific breakthrough in respect to catalysts started, according to Ref. [10] - [12], in the 1990s. The PEEM can image a solid state surface by using an electrostatic lens system to focus emitted photoelectrons<sup>15</sup> on a phosphorous screen. The formed image is often monitored by a CCD-camera which is connected to a data storage and

<sup>15</sup>See chapter 3.2.1.1 “The photoeffect”.

processing system. One of the main advantages of PEEM is the parallel imaging principle, which means that the image-forming photoelectrons are emitted by different surface sites simultaneously. Therefore, dynamic surface processes, e.g. adsorption, diffusion, reaction fronts, etc., can be studied in real time.

### 3.2.2.1 Working principle of the PEEM

Due to the illumination of the sample by electromagnetic radiation like UV-light (e.g. from a mercury or deuterium lamp) or X-rays (e.g. from Al/Mg-K $\alpha$ -sources or synchrotron radiation), photoelectrons are emitted from the surface via the photoeffect<sup>16</sup>. A scheme of an emitted photoelectron spectrum<sup>17</sup> which always has the width of  $h\nu - \Phi$  with  $h\nu$  meaning the photon or more specifically the excitation energy and  $\Phi$  meaning the sample work function, can be seen in Fig. 3.17. In the case of UV-PEEM, which was used in the experiments presented in this thesis, the difference between the energy of the exciting radiation and the sample's work function is mostly only a few eV. Therefore, the width of this spectrum shrinks, leading to a spectrum that is dominated by secondary (mainly inelastically scattered) electrons, as can be seen in Fig 3.18b. For example, a spectrum resulting from the illumination of a clean Pt(110) surface<sup>18</sup> by UV-light emitted from a deuterium lamp only contains a range of approximately 0,9 eV.

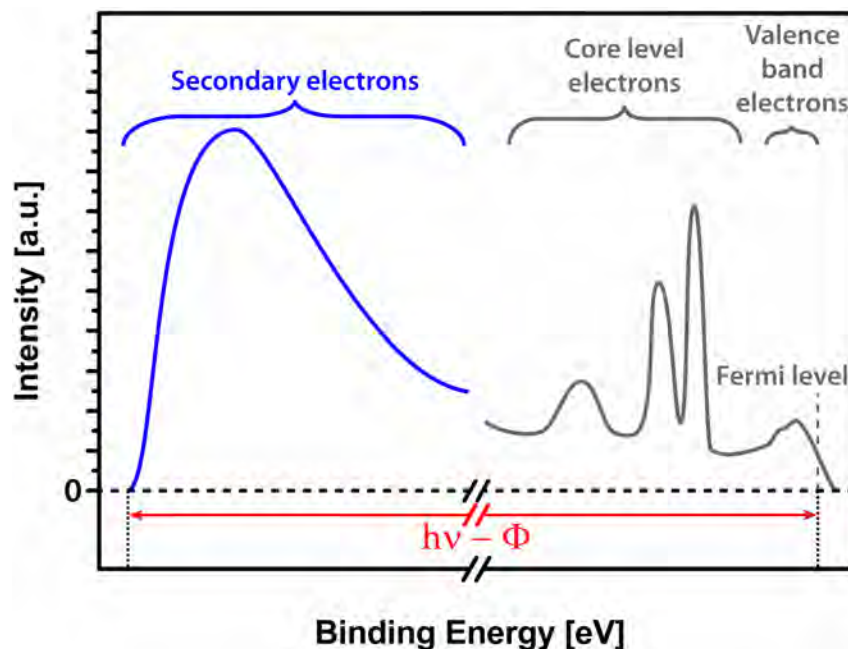


**Fig. 3.17:** General scheme of a photoelectron spectrum: The width of the spectrum depends on the excitation energy  $h\nu$  and the sample work function  $\Phi$ . The large number of secondary electrons contribute essentially to the PEEM image.

<sup>16</sup>See chapter 3.2.1.1 “The photoeffect”.

<sup>17</sup>See chapter 3.2.1.5 “The XPS-spectrum”.

<sup>18</sup>See chapter 4 “The model system: Pd powder on Pt foil”.

### 3 Experimental

If a sample whose local work function is heterogeneous is illuminated by electromagnetic radiation, the resulting spectra have different widths ( $h\nu - \Phi$ ). The energy range influences the peak area, meaning the number of electrons emitted from the surface, as shown in Fig. 3.18. Figure 3.18a schematically shows a metallic sample containing two areas with different local work functions, while Fig. 3.18b illustrates the expected electron spectra which correspond, due to the illumination by UV-light, mainly to the secondary (inelastically scattered) electrons. Fig. 3.18c shows the resulting PEEM image of the sample surface. The sample region with the lower work function emits more electrons (bigger peak area) than the region with the higher work function (smaller peak area). The difference in the local electron emissions results in the contrast of the PEEM image of the sample, as shown in Fig. 3.18c.

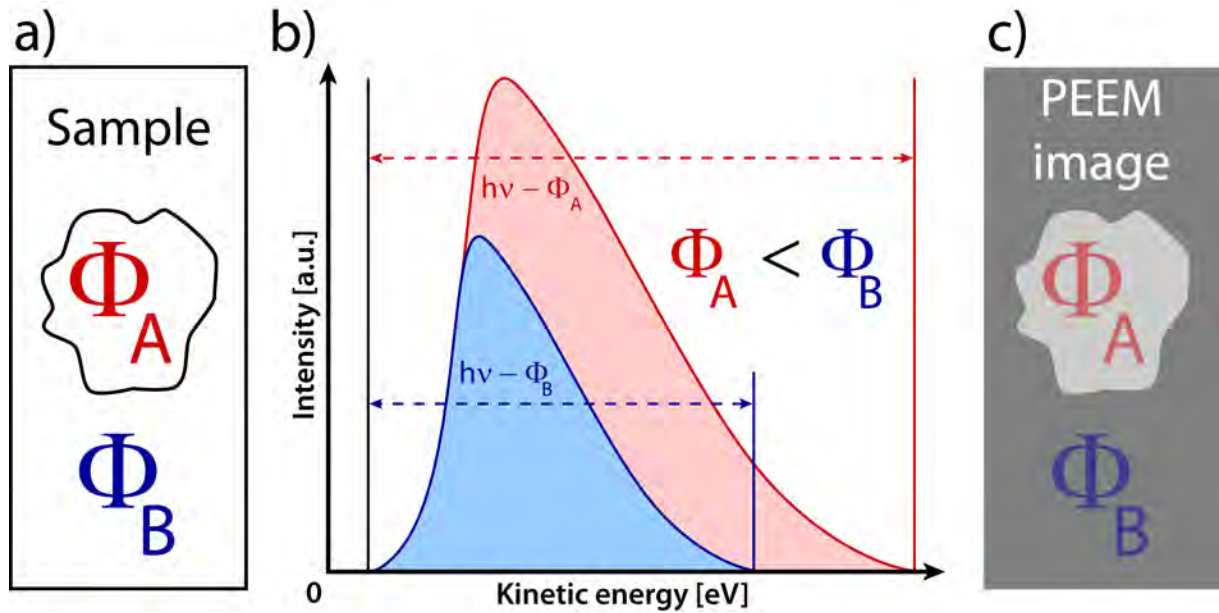


**Fig. 3.18:** Scheme of the contrast formation in PEEM:

- The metallic sample containing two regions with different work functions  $\Phi_A$  and  $\Phi_B$ .
- The photoelectron emission spectra of the two regions differ due to the difference between their work functions. The region with the lower work function ( $\Phi_A$ ) emits more electrons, which results in the photoelectron spectrum in the bigger area of the peak corresponding to the secondary electrons.
- The local brightness of the resulting PEEM image reflects the number of locally emitted electrons from the surface.

After Ref. [13].

The photoemission current can also be described by the Fowler-theory [14] which says that the emitted photoelectron flux  $j$  from a certain area of a surface depends on the

### 3 Experimental

energy of the illuminating light  $h\nu$  and the local work function of the sample area  $\Phi$ , namely

$$j \sim (h\nu - \Phi)^2. \quad (3.11)$$

The emitted photoelectrons are accelerated, formed and magnified by a lens system onto the detector. The detector mainly consists of a microchannel plate (MCP) which amplifies the weak signal without losing its spatial resolution, and a phosphorous screen which converts the electron beam into visible light. The formed magnified image can be monitored either visually or by use of a camera. For real time imaging the temporal resolution is primarily limited by the image brightness. Since increasing the frame rate reduces the exposure time, i.e. the number of photoelectrons which can excite the phosphorous screen, the temporal resolution at significant image brightness is solely limited by the frame rate of the camera.

#### 3.2.2.2 Layout of a UV-PEEM

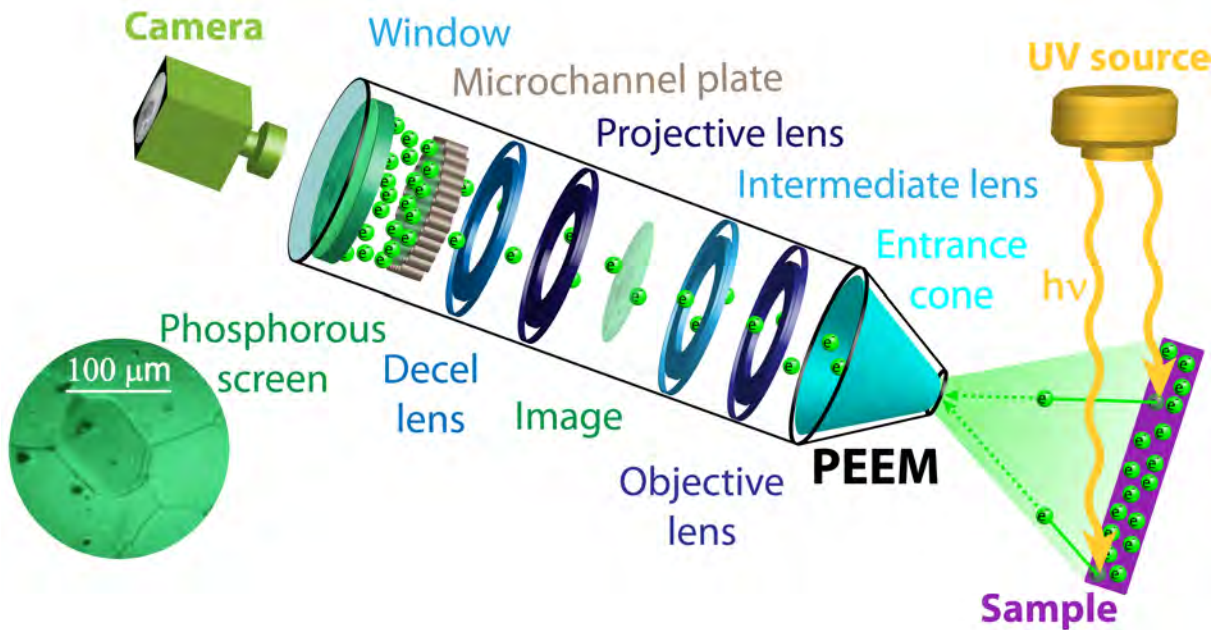


**Fig. 3.19:** Layout of a UV-PEEM:

Due to the illumination of the sample by UV-light photoelectrons are emitted. These photoelectrons are focused by an electrostatic lens system, amplified by a microchannel plate and projected onto a phosphorous screen. As a result a magnified picture of the sample forms on the phosphorous screen which can be recorded by a CCD camera.

### 3 Experimental

The PEEM-150 (STAIB Instruments) which was used in this thesis<sup>19</sup> enables the imaging of sample areas with diameters of approximately 500  $\mu m$ . The UV-source (deuterium lamp with  $E_{max} = 6,8 eV$ ) illuminates the sample under an incident angle of circa  $75^\circ$  due to the small distance between the sample and the entrance cone which in the used setup is approximately 5 to 10  $mm$ . The photoelectrons emitted<sup>20</sup> are accelerated by an anode voltage which is applied to the entrance cone. The photoelectrons passing the entrance cone are focused onto an image of the studied sample-area by the first two lenses of the lens system (objective and intermediate lens), whereby the objective lens is applied with a voltage of 2 to 4  $kV$  and the intermediate lens is applied with a voltage of 15 to 20  $kV$ . The weak electron signal should be amplified without losing its spatial resolution in order to provide sufficient intensity for imaging the sample surface. A microchannel plate (MCP) which is a kind of array of channeltrons<sup>21</sup> meets this requirement and is, therefore, usually used for amplifying the signal. A disadvantage of the MPC is its relatively low sensitivity maximum for impinging electrons which lies mostly between 200 and 2000  $eV$ . Therefore, the kinetic energy of the photoelectrons has to be decreased subsequently by the projective lens (1,58  $kV$ ) and the decelerating lens (1,25  $kV$ ) before the electrons impact on the MCP. The electron beam leaving the MCP as an amplified signal is accelerated by a voltage of 3  $kV$  onto the phosphorous screen which converts the magnified electron image into visible light. The screen is monitored from outside the UHV-system through a window by a CCD-camera (Hamamatsu Digital Camera C9300). This setup enables real-time images or videos of the surface with a spatial resolution in the low  $\mu m$  range and a temporal resolution in the low  $\mu s$  range.

#### 3.2.2.3 Evaluation of PEEM images

The contrast of PEEM images depends on the local work function, as shown qualitatively in Fig. 3.18 and eq. (3.11). Therefore, using PEEM provides the possibility to follow most phenomena and processes related to changes of the local work function. The black and white snap-shots shown in Fig. 3.20 which were taken during the kinetic transition of the platinum foil in the CO oxidation exemplify some phenomena which can be studied by the analysis of local grayscale values. For example the influence of different adsorbates on the local image brightness<sup>22</sup> and the role of different (hkl) planes can be seen.

---

<sup>19</sup>See chapter. 3.1 “The ultrahigh vacuum system”.

<sup>20</sup>See chapter 3.2.1.1 “The photoeffect”.

<sup>21</sup>See chapter 3.24 “The detector of the QMS”.

<sup>22</sup>See table 4.1.

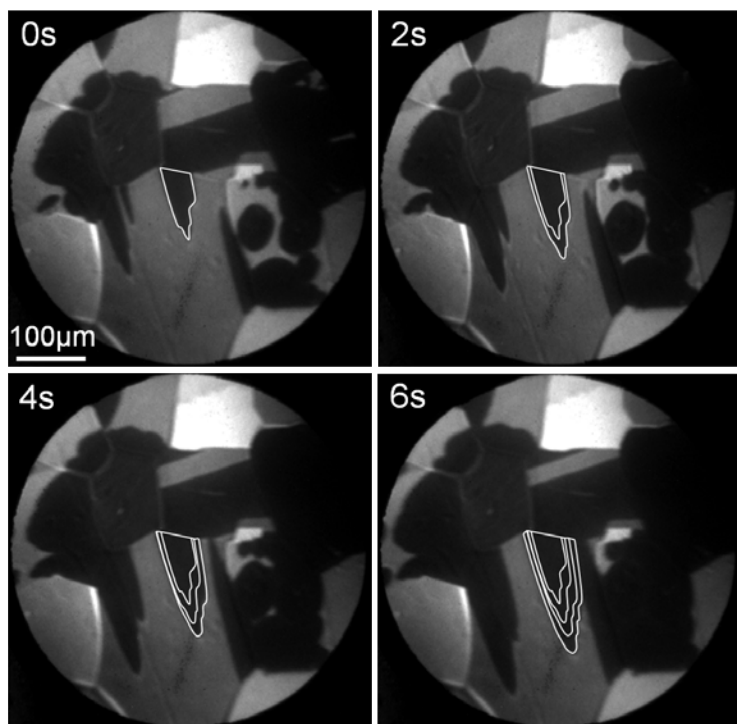


**Fig. 3.20:** PEEM snapshots taken during the catalytic CO oxidation reaction on a platinum foil:

During a kinetic transition oxygen (dark areas) displaces the CO coverage (bright areas) on all domains of the platinum foil. The propagation of one reaction front is respectively marked.

From Ref. [15]

### 3.2.3 Quadrupole Mass Spectrometry

Under UHV conditions, mass spectrometry (MS) can evaluate the composition of a gaseous phase or the components of molecules by determining the number of particles which possess a certain mass-to-charge ratio. In addition, MS can measure partial pressures and the total pressure simultaneously.

After a molecule enters the mass spectrometer, it is ionised, e.g. by electron ionization (EI). Afterwards an analyser filters the sample's ions based on their mass-to-charge ( $\frac{m}{z}$ ) ratio, so that only ions with a certain  $\frac{m}{z}$ -ratio reach the detector at the end of the analyser. Therefore, the detected signal contains information about the components of the gaseous phase. The plot of the signals for several  $\frac{m}{z}$ -ratios is called MS-spectrum.

Because mass spectrometers can only measure gases, solid or liquid samples have to be vaporized before they can be quantified. Big molecules, like proteins, have to be dissolved in special solvents before they can be measured by MS, otherwise, they would not be stable under UHV-conditions. By sputtering these solvents by electrospray ionization into the mass spectrometer, an aerosol is formed, which can be detected like molecules of a gaseous phases.

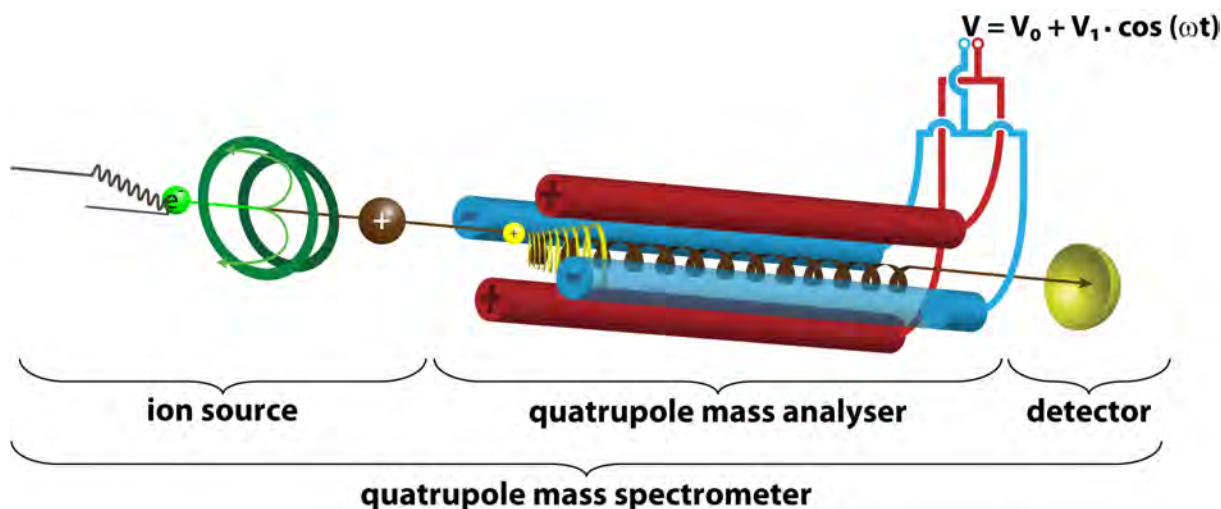


**Fig. 3.21:** Working principle of a QMS:

Inside the QMS two particles with different mass-to-charge-ratios are shown. The brown one can reach the detector on a stable spiral trajectory because of its mass-to-charge ratio. On the contrary the radius of the yellow trajectory expands until the yellow ion hits an electrode and is thus filtered out.

In the present thesis a quadrupole mass spectrometer (QMS) was used to measure the  $\text{CO}_2$  production rate at different reaction conditions, the partial pressures of the reactants ( $\text{CO}$  and  $\text{O}_2$ ) during the reaction, the compounds of the residual gas and the helium partial pressure in the UHV-system during a leak check.

The QMS uses an electron beam which is thermally emitted by a filament to ionize particles. The ions are filtered by a quadrupole mass filter<sup>23</sup> and detected by a Faraday cup<sup>24</sup>. If the pressure drops below  $2,6 \cdot 10^{-11} \text{ mbar}$ , an additional electron multiplier can be attached to measure pressures up to  $6,7 \cdot 10^{-14} \text{ mbar}$ <sup>25</sup>.

### 3.2.3.1 The Ion source of the QMS

Ion sources of mass spectrometers use often electron ionisation, fast-atom-bombardment (FAB), electrospray ionisation (ESI) or Matrix-assisted laser desorption/ionization (MALDI) to ionize particles. The charged particles are immediately accelerated to the quadrupole filter and the detector.

<sup>23</sup>See chapter 3.2.3.2 “The quadrupole mass analyser of the QMS”.

<sup>24</sup>See chapter 3.2.3.3 “The detector of the QMS”.

<sup>25</sup>See chapter 3.2.3.3 “The detector of the QMS”.

### 3 Experimental

#### 3.2.3.2 The quadrupole mass analyser of the QMS

Although, at the moment they enter the quadrupole mass analyser, all ions have nearly the same velocity vector which is parallel to the axis of the QMS, only a part of them reaches the detector. The quadrupole mass filter consists of four parallel cylindrical electrodes, arranged in a uniform cross. A DC  $V_0$  and an AC  $V_1$ , with the angular frequency  $\omega$ , are applied to the electrodes, so that opposite electrodes are poled identically. Therefore, the voltage on one electrode-pair is

$$V^+ = V_0 + V_1 \cdot \cos(\omega t), \quad (3.12)$$

while

$$V^- = -V_0 - V_1 \cdot \cos(\omega t) \quad (3.13)$$

is applied to the other pair. The time-dependent quadrupole field that is formed diverts all particles, dependent on their  $\frac{m}{z}$ -ratio. This can qualitatively be shown by combining the Lorentz force (3.14) and Newton's second law (3.15).

In the following  $\vec{F}$  stands for the force vector which effects the particles inside a mass spectrometer,  $q$  denoting the charge of the particles,  $\vec{v}$  means their velocity,  $\vec{a}$  stands for their acceleration,  $\vec{E}$  means the of the strength electric field and  $\vec{B}$  denoting the density of the magnetic flux.

$$\vec{F} = q \cdot (\vec{E} + \vec{v} \times \vec{B}) \quad (3.14)$$

$$\vec{F} = m \cdot \vec{a} \quad (3.15)$$

$$m \cdot \vec{a} = q \cdot (\vec{E} + \vec{v} \times \vec{B}) \quad (3.16)$$

$$\frac{m}{q} \cdot \vec{a} = (\vec{E} + \vec{v} \times \vec{B}) \quad (3.17)$$

The quantitative magnitude of the acceleration of an ion between an electrode-pair is given by the Mathieu function, with  $x$  meaning the deflection of the ion from the middle between the two positive electrodes,  $y$  standing for the deflection of the ion from the middle between the two negative electrodes and  $r_0$  for the half of the distance between two electrodes with identical loading.

$$\frac{d^2x}{d\tau^2} + [\zeta + 2 \cdot \xi \cdot \cos(2 \cdot \tau)] \cdot x = 0 \quad (3.18)$$

$$\frac{d^2y}{d\tau^2} - [\zeta + 2 \cdot \xi \cdot \cos(2 \cdot \tau)] \cdot y = 0. \quad (3.19)$$

### 3 Experimental

The quantities  $\omega t$ ,  $\omega dt$ ,  $\zeta$  and  $\xi$  are defined as follows.

$$\omega \cdot t = 2 \cdot \tau \quad (3.20)$$

$$\omega \cdot dt = 2 \cdot d\tau \quad (3.21)$$

$$\zeta = \frac{4 \cdot q \cdot V_0}{m \cdot \omega^2 \cdot r_0^2} \quad (3.22)$$

$$\xi = \frac{2 \cdot q \cdot V_1}{m \cdot \omega^2 \cdot r_0^2} \quad (3.23)$$

The detailed discussion of the solution of the Mathieu function would exceed the scope of this work. It shall only be stated that the solutions are periodic functions which can be stable or unstable for a certain setting of the parameters  $\zeta$ ,  $\xi$  and the  $\frac{m}{z}$ -ratio. Therefore, some particles can pass the quadrupole field, while the amplitude of others increases until they collide with an electrode.

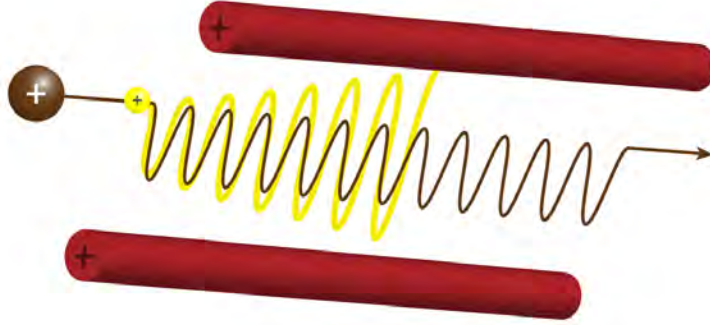


**Fig. 3.22:** Deflection of particles in the quadrupole field whose mass-to-charge-ratio is too small: The amplitude of particles whose mass-to-charge-ratio is too small (yellow) grows exponentially due to the alternating field until it hits a positively charged electrode. Particles which have the correct or a bigger mass-to-charge-ratio, remain on a stable trajectory due to their inertia.

Positively charged ions in the quadrupole field keep oscillating around the potential minimum in the middle of the two positively charged electrodes, because the electric field that corresponds to the direct current always accelerates the ion towards the middle. The magnitude of this acceleration is proportional to the reciprocal value of the distance between the ion and the electrode. The alternating field additionally simulates ions whose  $\frac{m}{z}$ -ratio is too small to an additive oscillation, which leads to an exponential increase of their amplitude and finally to a collision of the ion and an electrode. Because of their inertia, ions possessing the right or a bigger  $\frac{m}{z}$ -ratio are not affected significantly by the additional field.

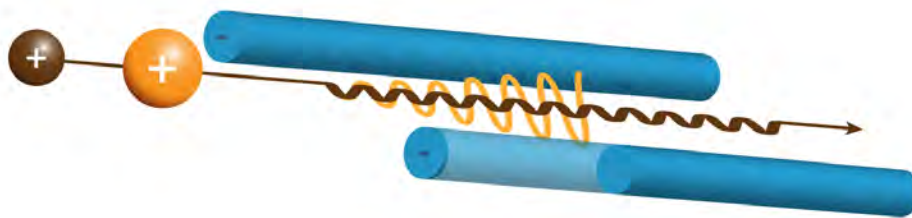


**Fig. 3.23:** Deflection of particles in the quadrupole field whose mass-to-charge-ratio is too big: Particles whose mass-to-charge-ratio is too big (orange) hit a negatively charged electrode, because their trajectory is not stabilized by the alternating field.

Positively charged ions also interact with the potential maximum between the two negatively charged electrodes which arises from the direct current. The corresponding force accelerates the ions radially outwards, while an additional force which relies on the alternating current accelerates them back to the middle. The trajectory of ions with the right or a smaller  $\frac{m}{z}$ -ratio can be sufficiently stabilized, while the inertia of ions whose  $\frac{m}{z}$ -ratio is too big impedes them from oscillating around the potential maximum.

Because both described oscillations superimpose in the quadrupole field with constant parameters ( $V_0$ ,  $V_1$  and  $\omega$ ), only ions which have a certain  $\frac{m}{z}$ -ratio can pass a quadrupole mass analyser on a spiral trajectory, while all others collide with one of the four electrodes. Therefore, partial pressures of different compounds of the gaseous phase or the total pressure in the UHV-system can be measured by varying the parameters of the quadrupole field. Most QMS vary only  $\omega$  or  $V_0$  and  $V_1$ .

Two important disadvantages of a QMS should also be mentioned here: A QMS cannot distinguish between two particles having the same  $\frac{m}{z}$ -ratio but different masses and charges, e.g.  $m_2 = 3 \cdot m_1$  and  $z_2 = 3 \cdot z_1$ . The second disadvantage concerns the difficulties of interpreting a QMS-spectrum, because some particles could be ionized several times (e.g.  $\text{CO}^{++}$ ), big molecules could split up into fragments and so on.

### 3.2.3.3 The detector of the QMS

The detector of a QMS is mostly a Faraday cup (FC) which may be supported by a secondary electron multiplier (SEM).

The FC is a metal cup positioned in the ions' trajectory. If an ion collides with the detector, electrons from the metal cup neutralize the ion. Because an electric field prevents the

### 3 Experimental

loss of secondary electrons emitted from the cup, the measurement of the electron current which is needed to keep the potential of the detector constant is related to the incoming ion current. Advantages of the FC are its robustness and its ability to measure the charge flow absolutely, although it needs relatively high pressures ( $10^{-5}$  to  $10^{-3}$  mbar) to detect a workable signal.

An SEM can convert weak ion signals into intensive electron beams. Therefore, an FC which is supported by an SEM can deliver good results at far lower pressures than a single FC could. If an ion impacts to the first dynode of the SEM, the resulting secondary electrons are further multiplied inside the SEM. A dynode is one electrode of a series of electrodes inside an SEM that is coated with special materials which lead to the emission of three to ten secondary electrons per impact. Furthermore, an acceleration voltage is applied to the dynodes, whereby the voltage drop between each two successive electrodes is equal. This drops results in an acceleration of the emitted electrons from a dynode to its successive one, whereby the impacting secondary electrons lead again to the emission of further electrons.

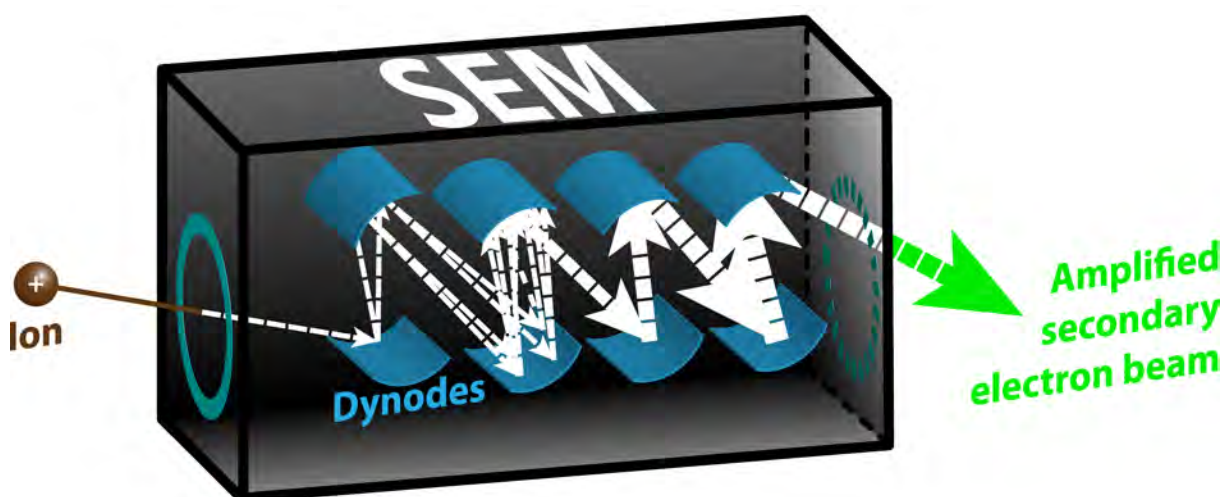


**Fig. 3.24:** Working principle of an SEM:

An SEM amplifies a weak signal by a process called secondary electron emission. If one particle, e.g. an ion or an electron, impacts to a dynode, it induces the emission of several secondary electrons which are, due to a voltage drop, accelerated to the next dynode. The amplified signal leaves the SEM as an electron beam.

The number of electrons inside the SEM increases exponentially with the number of dynodes. If, e.g., an SEM contains ten dynodes and each emits, on average, four secondary electrons, each impacting ion results in an electron beam of  $4^{10}$  electrons, which is a signal amplification of about one million. This enormous signal amplification is the SEM's

biggest strength, but also its greatest weakness because the resulting electron beam can harm and even destroy the detector, if the SEM is used at too high pressures.

Like an SEM, also channeltrons amplify weak signals by using a similar method. A channeltron is a curved glass capillary, which, similar to dynodes, is coated with a semiconductor to enable the emission of several secondary electrons per impact. Contrary to an SEM, it consists of only one component and therefore the voltage of about 3 kV drops continuously. Thus all secondary electrons emitted are amplified to the detector, but due to the curving of the channeltron most secondary electrons collide again with the coating and therefore, amplify the signal further.

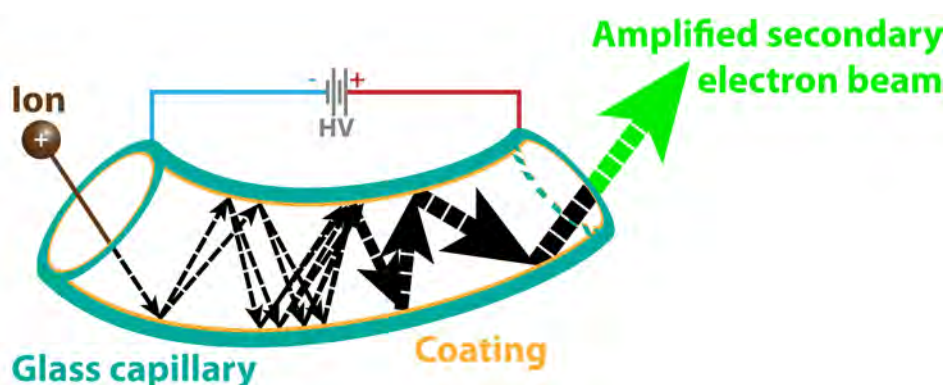


**Fig. 3.25:** Working principle of a channeltron:

A channeltron amplifies weak signals like an SEM. Particles of the weak signal hit the coating of the glass capillary and induce the emission of secondary electrons which hit the coating several times before they leave the channeltron as an electron beam which can be clearly detected.

Also neutral particles can distort the detected signal which should ideally be only ion-related, by knocking secondary electrons out of the coating. This distortion can be prevented by mounting the channeltron in the *off axis* geometry. In this case a conversion dynode, to which about 4 kV are amplified, and the entrance of the channeltron are mounted vis-à-vis and parallel to the origin trajectory of the particles. While neutral particles are not affected by the charged electrode and, therefore, pass by the entrance of the channeltron, ions are accelerated to the conversion dynode. The impact of the ions on the electrode induces the emission of secondary electrons which enter the channeltron and leave it as an electron beam which reaches the detector<sup>26</sup>.

<sup>26</sup>See Fig. 3.26.

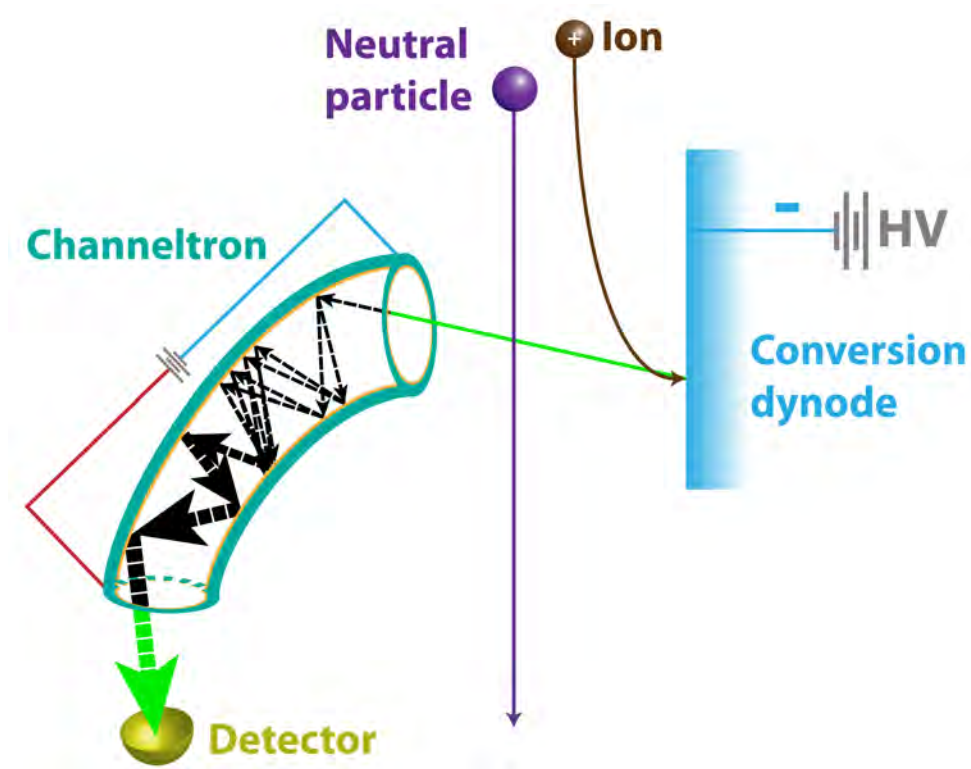


**Fig. 3.26:** To prevent the distortion of the signal by neutral particles, most channeltrons are mounted in the *off axis* geometry.

# 4

## The model system: Pd powder on Pt foil

---

Real catalysts do not consist of perfect single crystals or clearly defined polycrystalline metal foils. In turn, real commercial catalysts contain mainly nano particles which are supported by oxidic material like  $\text{Al}_2\text{O}_3$ . Despite intensive studies the role of the supporting material in the catalytic behaviour of the used powders has not been not understood in all its details until now.

In this thesis questions concerning the relevance of spatial coupling and the role of different supports, e.g. a platinum foil or  $\text{Al}_2\text{O}_3$ , in the CO oxidation reaction are studied. Further, the influence of the composition and the morphology of the compounds of model systems on their catalytic behaviour is discussed. Additionally, the influence of the size and the shape of palladium powder agglomerates on their reactivity in the CO oxidation reaction were investigated.

### 4.1 Platinum and palladium

Although platinum (Pt) and palladium (Pd) are quite rare and expensive materials, their highly catalytic activity makes them very interesting for chemical processes. Both belong to the platinum group which further consists of the elements ruthenium (Ru), rhodium (Rh), osmium (Os) and iridium (Ir). Pt and Pd both belong to the tenth group of the

#### 4 The model system: Pd powder on Pt foil

periodic table of the elements and therefore show a rather similar chemical behaviour.

The total electronic configuration of  $_{78}\text{Pt}$  is  $1s^2 2s^2 2p^6 3s^2 3p^6 4s^2 3d^{10} 4p^6 5s^2 4d^{10} 5p^6 4f^{14} 5d^9 6s^1$ , while  $_{46}\text{Pd}$  has the total electronic configuration of  $1s^2 2s^2 2p^6 3s^2 3p^6 4s^2 3d^{10} 4p^6 4d^{10}$ .

Both crystallize in a face-centred cubic (fcc) crystal lattice with a lattice constant of approximately  $3,92 \text{ \AA}$  for Pt and approximately  $3,88 \text{ \AA}$  for Pd. Because the three low Miller index planes (100), (110) and (111) have the lowest surface energy [16], they mainly crystallize upon heating. The different (hkl) planes vary in their surface density of atoms, which leads, as predicted by Smoluchowski [17], to different work functions and to different adsorption sites for molecules that adsorb from a gaseous phase. For example CO can adsorb on all planes of Pt group metals on top of a single surface atom or create a bridge bound between two surface atoms, while only Pt(110) and Pt(111) surfaces provide adsorption places, where CO can coordinate fourfold between four atoms of the first layer. Furthermore, the work function of clean Pt(110) and Pt(110) surfaces differ by  $0,45 \text{ eV}$ .

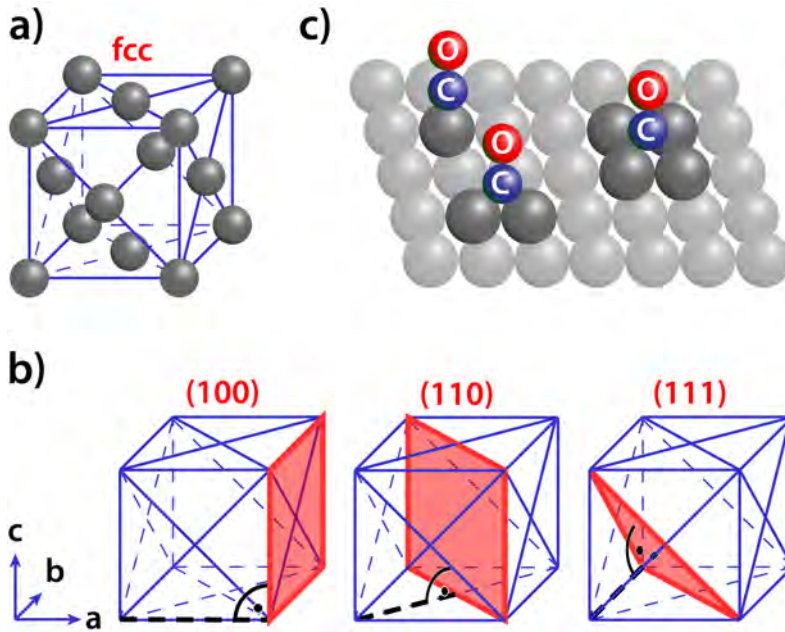


**Fig. 4.1:** Surface crystallography of Pt and Pd and their adsorption sites for CO:

a) Platinum and palladium crystallize in a face-centred cubic crystal lattice.

b) Different low index (hkl) planes of the fcc unit cells.

c) CO can adsorb on top (upper left corner), bridge bound (bottom left) or fourfold (middle right).

**Tab. 4.1:** Comparison of the work function values for different clean and adsorbate-covered low index Pt planes taken from Refs. [18] - [22].

Pt(hkl)	clean [eV]	CO-covered [eV]	oxygen-covered [eV]
Pt(100)	5,84	6,04	6,3
Pt(110)	5,49	5,8	6,5
Pt(111)	5,93	6,13	6,38

## 4.2 The sample

For obtaining new insights into the topics named at the beginning of this chapter, a new model system was developed to compare its catalytic behaviour with three different model systems: a polycrystalline palladium foil (Alfa Aesar, 99.9%), a polycrystalline platinum foil (MaTecK, 99.99%) and the more complex system consisting of palladium powder (Fluka AG) supported by an  $\text{Al}_2\text{O}_3$  foil.

For creating the new sample, the same palladium powder which was used for the Pd/ $\text{Al}_2\text{O}_3$  system was impregnated into the polycrystalline platinum foil which has already been studied as a second system. The  $10 \times 10 \text{ mm}^2$  large and  $0,25 \text{ mm}$  thick platinum foil was cleaned by mechanical polishing, additionally flame-annealed in air and furthermore cleaned in an ultrasonic bath with acetone before the Pd powder was impregnated into it at room temperature under a pressure of three tons. Afterwards the sample was placed in the UHV-system and annealed for several hours at 1000 to 1100 °C for forming domains with clear crystallographic orientations.

Further the sample was prepared before each experiment by several cycles of sputtering, annealing and heating in oxygen. The chemical purity was controlled by XPS-measurements using alumina  $K\alpha$  radiation (1486,6 eV). Two measured XPS-spectra which verify that palladium powder was successfully impregnated on only half of the platinum foil and that the foil surface was already clean, are shown on the next page in Fig. 4.2.

After the purity of the sample was proven, a certain region of the sample with a diameter of approximately  $500 \mu\text{m}$  was destined to be studied by PEEM. The chosen region includes two palladium powder agglomerates of different size and shape and several domains of the Pt foil, among others a Pt(100) and a Pt(110) domain which were studied in detail. The Pt(100) and the Pt(110) domain could be localized by considering Tab. 4.1 and the behaviour of the occurring reaction fronts during the CO oxidation<sup>27</sup>.

---

<sup>27</sup>See Fig. 5.2.

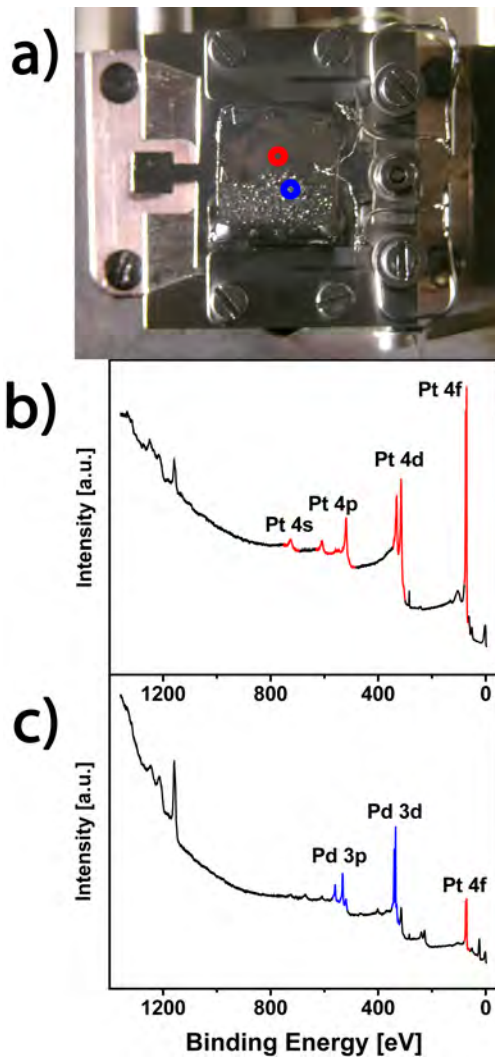


**Fig. 4.2:** The composition of the Pd/Pt model system was proven by XPS:

a) The sample placed in the XPS chamber.

b) The XPS-spectrum from the upper half of the sample shows only the characteristic Pt-peaks (*Pt 4f*, *Pt 4d*, *Pt 4p* and *Pt 4s*).

c) The XPS-spectrum from the lower half of the sample shows primarily the significant peaks of the impregnated Pd powder (*Pd 3d* and *Pd 3s*), but also peaks from the Pt foil visible between the powder agglomerates. Because some peaks of Pt and Pd superimpose, only the *Pt 4f* peak was marked as a representative example for the occurrence of Pt.

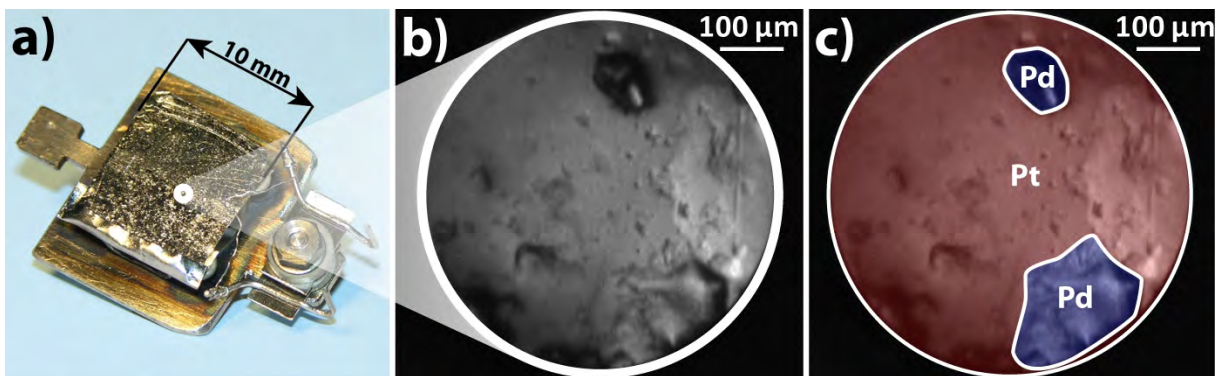


**Fig. 4.3:** Composition of the sample:

a) The sample mounted on the sample holder plate.

b) PEEM image of the sample-region studied.

c) The field of view is colour-marked for better differentiation: The Pd powder agglomerates are marked blue while the Pt foil is marked red.

# 5

## CO oxidation reaction on the Pd/Pt model system

---

This chapter describes the experimental procedure and the results of the CO oxidation experiments. The global kinetic behaviour of the CO oxidation reaction catalysed by the Pd/Pt model system and the local kinetics of the Co oxidation reaction on two low Miller index domains of the Pt foil and on Pd powder agglomerates are presented. The results concerning the Pd-part of the sample are compared with three different model systems in order to clarify the role of the support and of the morphology of the catalytically active Pd powder in the CO oxidation reaction.

### 5.1 Experimental procedure

In order to provide the same reaction conditions for each measurement, the Pd/Pt sample was always prepared by the same cleaning procedure before the experiments. First, the sample was sputtered by  $\text{Ar}^+$  ions for 15 minutes to remove remaining reactants of the last experiment, impurities which segregated from the bulk to the surface and adsorbates. The partial argon pressure during the sputtering was  $6 \times 10^{-6} \text{ mbar}$ , the energy of the ions was 1 *kV*. This setting led to a typical  $\text{Ar}^+$  ion current of 4 to 4,5  $\mu\text{A}$ . The sputtering was followed by annealing the sample for twenty minutes at 1073 *K* to smoothen the sample surface. The last step was to heat the sample for twenty minutes in oxygen at a partial

oxygen pressure of  $8 \times 10^{-7}$  mbar at a temperature between 623 and 773 K to remove carbonaceous contaminants. The effectiveness of the cleaning procedure was verified by XPS.

During the PEEM measurements the quadrupole mass spectrometer was used to control the gaseous phase inside the UHV system, i.e. the partial oxygen pressure of  $1,3 \times 10^{-5}$  mbar which was held constant during all experiments, the actual partial CO pressure and the partial CO<sub>2</sub> pressure used as an indicator for the CO<sub>2</sub> production rate.

The global and local kinetic behaviour of the CO oxidation reaction were studied by cyclic variations of the CO pressure at constant temperature and constant oxygen pressure<sup>28</sup> and by so-called ignition experiments which simulate a “cold start” of a three-way catalyst by heating up the “cold” sample at constant partial pressures of oxygen and CO until the catalytic ignition takes place.

## 5.2 Global kinetic behaviour of the CO oxidation reaction catalysed by the Pd/Pt model system

The global reaction behaviour of the Pd/Pt system during the cyclic variation of the CO pressure at constant temperature and constant oxygen pressure was monitored by a quadrupole mass spectrometer (QMS). The data received show that the plot of the CO<sub>2</sub> production rate ( $R_{CO_2}$ ) as a function of the partial CO pressure forms a hysteresis curve<sup>29</sup>, as shown in Fig. 5.1.

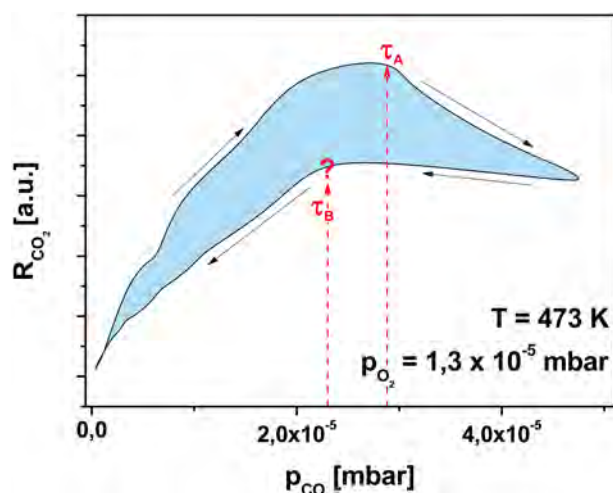


**Fig. 5.1:** Plot of the global production rate of CO<sub>2</sub> as a function of the partial CO pressure:

The hysteresis plot of  $R_{CO_2}$  was measured at 473 K and a partial oxygen pressure of  $1,3 \times 10^{-5}$  mbar. The production rate of CO<sub>2</sub>, measured by the QMS, represents the total CO<sub>2</sub> production of both compounds of the sample (Pd and Pt), i.e. the superposition of the Pd and Pt production rate curves. The overlap of the Pd and the Pt hysteresis curves only enables the determination of  $\tau_A$  of the model system, but not  $\tau_B$  (see text).

<sup>28</sup>See chapter 2.5 “Bistability and the kinetic phase diagram”, specially Fig. 2.5.

<sup>29</sup>See Fig. 2.5.

By analysing the hysteresis curve in Fig. 5.1, the transition point  $\tau_A$  (kinetic transition point from the steady state of high reactivity to the steady state of low reactivity) can be determined. Unfortunately, it seems impossible to determine  $\tau_B$  (kinetic transition from the steady state of low reactivity to the steady state of high reactivity), because of the smoothed and diffuse character of the curve. To clarify the behaviour of the system, it is necessary to perform measurements which enable separate local analyses of the Pd and the Pt part of the sample. This can be done, as recently shown [23] by using PEEM. The analyses of PEEM video-sequences taken in situ during the CO oxidation allow the determination of local kinetic transitions for individual regions of a surface, e.g. for individual  $\mu\text{m}$ -sized domains of a polycrystalline Pt foil.

Thus, it was reasonable to perform a PEEM study of different parts of the chosen field of view shown in Fig. 5.2. The field of view contains, among others, two Pd powder agglomerates and two low Miller index Pt domains.

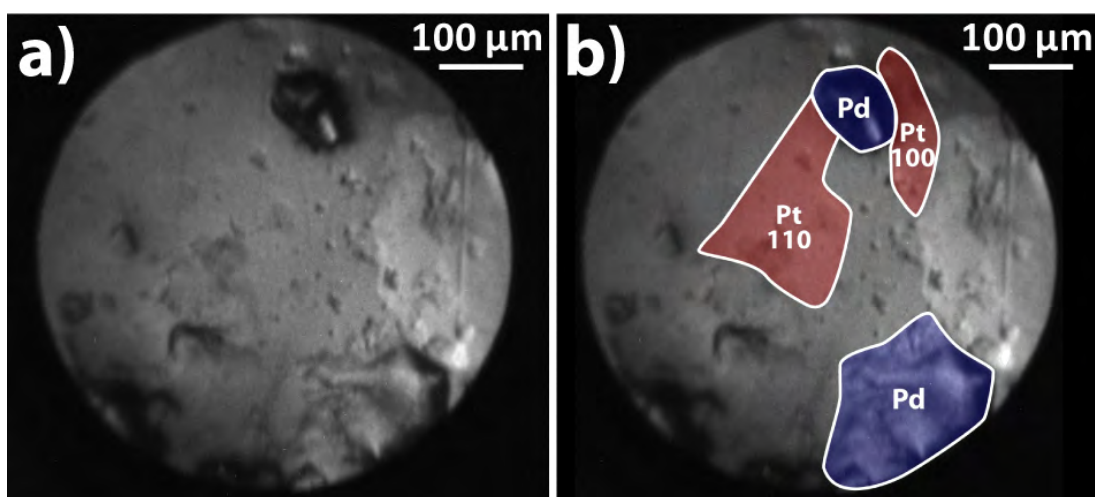


**Fig. 5.2:** A section of the Pd/Pt model system sample imaged by PEEM:

a) Image of the surface of the Pd/Pt system “as it is“. The two Pd powder agglomerates within the field of view are clearly visible due to the contrast, while the Pt domains had to be localised by comparing their local intensities at differently coverages with literature values of the work function of different covered low Miller index Pt planes.

b) The same as a), but the two Pd powder agglomerates, Pt(100) and Pt(110), are marked.

The Pd agglomerates within the field of view can be easily distinguished from the Pt foil by the material contrast (different work function) and their different structure<sup>30</sup> as it can be seen in Fig. 5.2. By comparing literature values of clean and adsorbate-covered low Miller index Pt planes<sup>31</sup> with PEEM images of the clean, oxygen-covered and CO-covered

<sup>30</sup>See chapter 3.2.2.3 “Evaluation of PEEM images”.

<sup>31</sup>See table 4.1.

## 5 CO oxidation reaction on the Pd/Pt model system

surface, a Pt(100) and a Pt(110) domain could be localised within this field of view. The identification of the Pd agglomerates and the Pt domains enables the local analyses of the reaction kinetics on these four regions.

Figure 5.3 shows PEEM snapshots of the CO oxidation on the Pd/Pt sample taken at 473 K and a partial oxygen pressure of  $1,3 \times 10^{-5}$  mbar corresponding to the same measurement shown in Fig. 5.1.

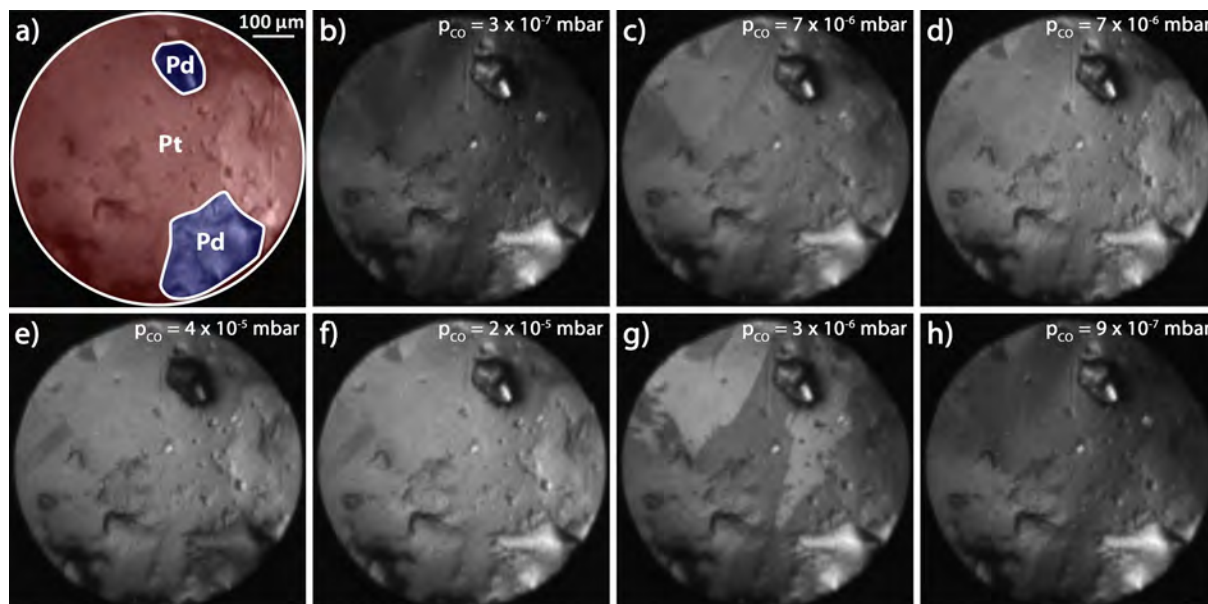


**Fig. 5.3:** PEEM snapshots of the kinetic transitions during the CO oxidation on the Pd/Pt model system at 473 K and a partial oxygen pressure of  $1,3 \times 10^{-5}$  mbar:

- A coloured image of the field of view.
- The whole sample is oxygen-covered, i.e. the sample is in the steady state of high reactivity.
- The kinetic transition from the oxygen-covered to the CO-covered surface begins on the Pt part (increasing brightness), because CO prevails in the competitive adsorption process due to increased CO pressure. Pd remains oxygen-covered.
- Pt is fully CO-covered, while Pd still remains oxygen-covered.
- The transition to the CO-covered Pd surface begins (contrary to Pt the brightness is decreasing).
- Due to the cyclic variation of the CO pressure (decreasing stage) oxygen again prevails in the competitive adsorption process on Pd, meaning Pd transits back to the steady state of high reactivity (increasing brightness). Pt remains CO-covered.
- The same kinetic transition occurs on the Pt surface (decreasing brightness).
- The whole sample is oxygen - again.

The snapshots in Fig. 5.3 show qualitatively that the Pd and the Pt part of the sample seem to retain their independence in respect to the kinetic transitions during the CO

oxidation reaction. The detailed quantitative analysis of the digitized video-frames might clarify this ultimately.

### 5.3 Local kinetics of the CO oxidation on the Pt part of the sample

As it could be seen from Fig. 5.3, the kinetic transitions on the Pt part of the Pd/Pt model system can be distinguished from those of the Pd part by PEEM. In the following kinetic transitions on the Pt part of the sample are studied in detail.

Kinetic transitions can be monitored by PEEM because adsorbed CO and oxygen influence the local work function of the surface<sup>32</sup> and therefore, the local PEEM image brightness<sup>33</sup> differently. The present chapter is focused on quantitative evaluations of local PEEM intensities of the two low Miller index Pt domains shown in Fig. 5.2. For the evaluation, the intensities inside the used rectangular regions of interest (ROIs) which filled as large an area of the domains as possible, were integrated. The ROIs inside the Pt(100) domain were  $40 \times 100 \mu\text{m}$ , while the ROIs concerning Pt(110) were  $80 \times 110 \mu\text{m}$ .

The CO oxidation experiments were similar to the measurements shown in Fig. 5.1 and Fig. 5.3: the partial CO pressure was changed cyclically in the range of  $5 \times 10^{-7}$  to  $5 \times 10^{-5} \text{ mbar}$ , while the partial oxygen pressure was set to  $1,3 \times 10^{-5} \text{ mbar}$  and the temperature was held constant. The plot of the PEEM intensity of the Pt(100) domain during such an experiment performed at  $473 \text{ K}$  and corresponding snapshots are shown in Fig. 5.4 a. Following the hysteresis-like PEEM intensity curve it is possible to determine the local transition points for the Pt(100) domain: at the beginning of the experiment the Pt surface is oxygen-covered (high work function, low brightness) and thus is in the catalytic steady state of high reactivity (frame 1 and the corresponding point 1 on the plot). In this stage an increase of the partial CO pressure leads to an increased CO adsorption rate (the dissociative adsorption of oxygen leaves enough free adsorption sites for CO), which causes an increase of the  $\text{CO}_2$  production rate. If the partial CO pressure reaches a certain value, it leads to an overbalance of CO in the competitive coadsorption with oxygen and to the dominance of CO in the adsorption process. Therefore, the surface coverage changes from oxygen-covered to CO-covered. This process is the kinetic transition from the catalytically active to the inactive surface. The transition point  $\tau_A$ ,

---

<sup>32</sup>See table 4.1.

<sup>33</sup>See chapter 3.2.2.3 "Evaluation of PEEM images".

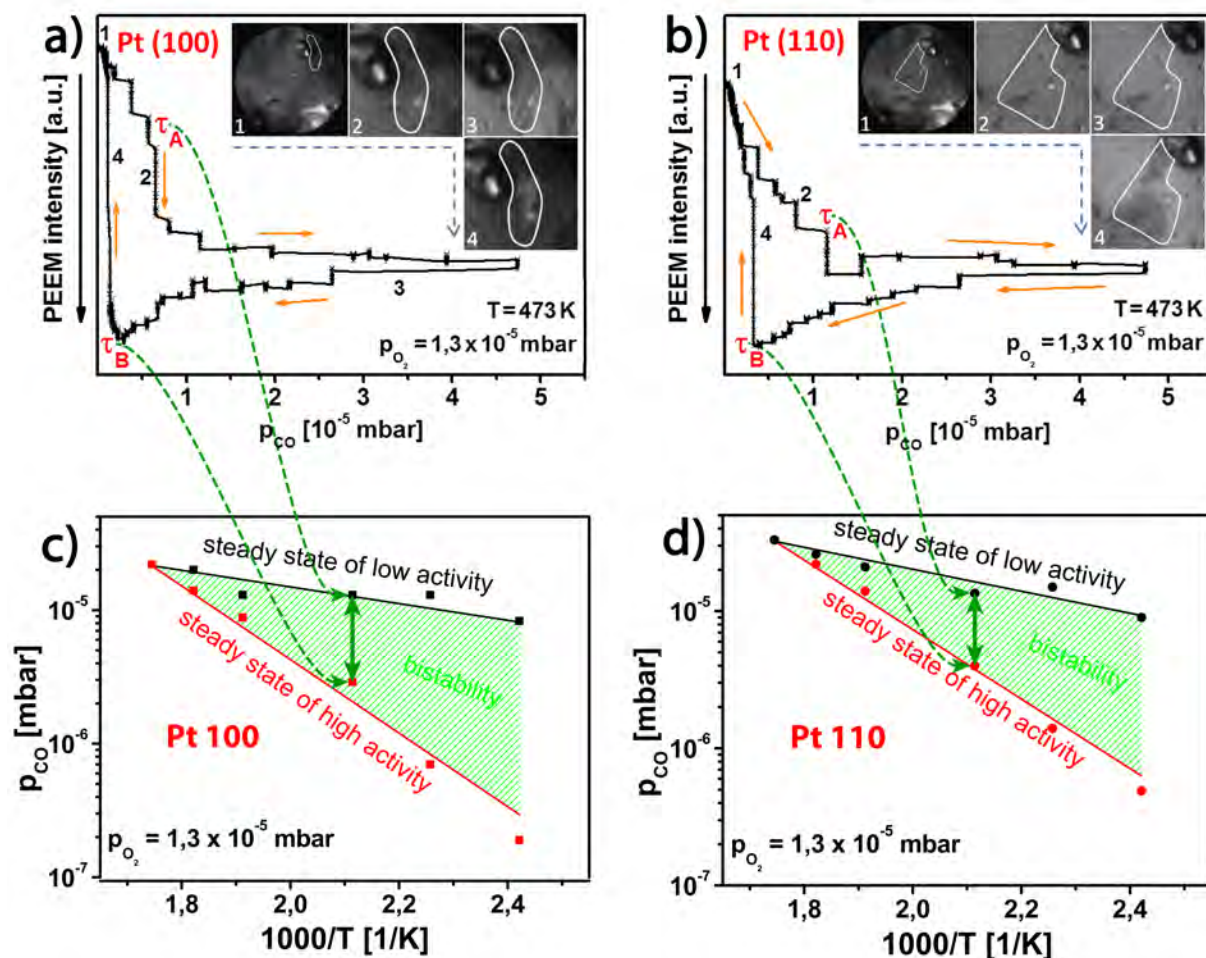


**Fig. 5.4:** Hysteresis plot for the the local PEEM intensity of Pt(100) and Pt(110) domains during the CO oxidation at a constant temperature with a cyclic variation of the CO pressure and the corresponding kinetic phase diagrams:

a) At the beginning of the experiment the Pt(100) domain is oxygen-covered (high work function, low intensity, point 1 in the plot and frame 1), i.e. the sample is in the steady state of high reactivity. The kinetic transition from the oxygen-covered to the CO-covered surface occurs at  $\tau_A$  (decreasing work function, increasing brightness, point 2 in the plot and frame 2). A further increase of  $p_{\text{CO}}$  does not change the image brightness nor the  $\text{CO}_2$  production rate (low work function, high intensity, point 3 in the plot and frame 3). At the decreasing stage of the cyclic  $p_{\text{CO}}$  variation, oxygen again prevails at  $\tau_B$  in the competitive adsorption process and thus the sample transits back to the steady state of high reactivity (decreasing work function, increasing brightness, point 4 in the plot and frame 4).

b) The same as in a), but for Pt(110).

c) The transition points obtained from the hysteresis curves are used to construct the kinetic phase diagrams for Pt(100) which characterise the catalytic behaviour of the reaction system within a certain temperature and pressure range.

d) The same as in c) but for Pt(110).

where the image brightness increases abruptly (due to the decrease of the work function), is well visible in the PEEM plot (frame 2 and the corresponding point 2 on the plot). The domination of the CO adsorption leads to the decrease of the CO<sub>2</sub> production rate, because oxygen can hardly adsorb on the CO-covered surface (both reactants have to adsorb before they can react with each other<sup>34</sup>).

After the system has reached the steady state of low reactivity, any further increase of the partial CO pressure does not significantly change the intensity (see frame 3 and the corresponding point 3 on the plot) nor the CO<sub>2</sub> production rate. When the partial CO pressure is reduced again to  $\tau_A$ , the surface still remains CO-covered, because there are still not enough pairs of free adsorption sites for a significant increase of the dissociative oxygen adsorption. Only after the partial CO pressure reaches the reversed transition point  $\tau_B$ , oxygen prevails again in the competitive adsorption process (increase of the work function, decrease of the brightness) and the system “jumps over” into the steady state of high reactivity (see frame 4 and the corresponding point 4 on the plot).

Such a hysteresis-like PEEM intensity curve characterizes the system at a particular temperature. In order to characterise the catalytic behaviour of the system within a certain temperature range, the transition points, which are related to a series of measurements performed at the same partial oxygen pressure but at different temperatures can be combined to a so called kinetic phase diagram which shows the evaluated transition points in a  $p_{CO}/T^{-1}$  phase space as shown schematically in Fig. 2.6. The kinetic phase diagram for the Pt(100) domain is shown in Fig. 5.4 c.

The same analyses were performed for the Pt(110) domain. The intensity plot and corresponding frames are shown in Fig. 5.4 b. Also the corresponding kinetic phase diagram was constructed and is shown in Fig. 5.4 d. It is clearly visible that the diagrams for Pt(100) and Pt(110) are different. It is interesting to compare the present results for a combined Pd/Pt model system sample with the literature, where such measurements were performed for the pure Pt sample [24].

The comparison between the kinetic phase diagrams for the Pt(100) and Pt(110) domains as measured for the Pd/Pt model system with the previous results obtained for the corresponding domains on a pure Pt foil [24] is shown in Fig. 5.5.

Figure 5.5 exhibits a very good agreement between the actual data and earlier measurements. This confirms an independence of the CO oxidation reaction on the individual domains of the Pt foil and demonstrates also an independence of the reaction process on the different Pt domains from the presence of the Pd agglomerates. This means that

---

<sup>34</sup>See chapter 2.4 “The Langmuir-Hinshelwood mechanism of the CO oxidation reaction”.

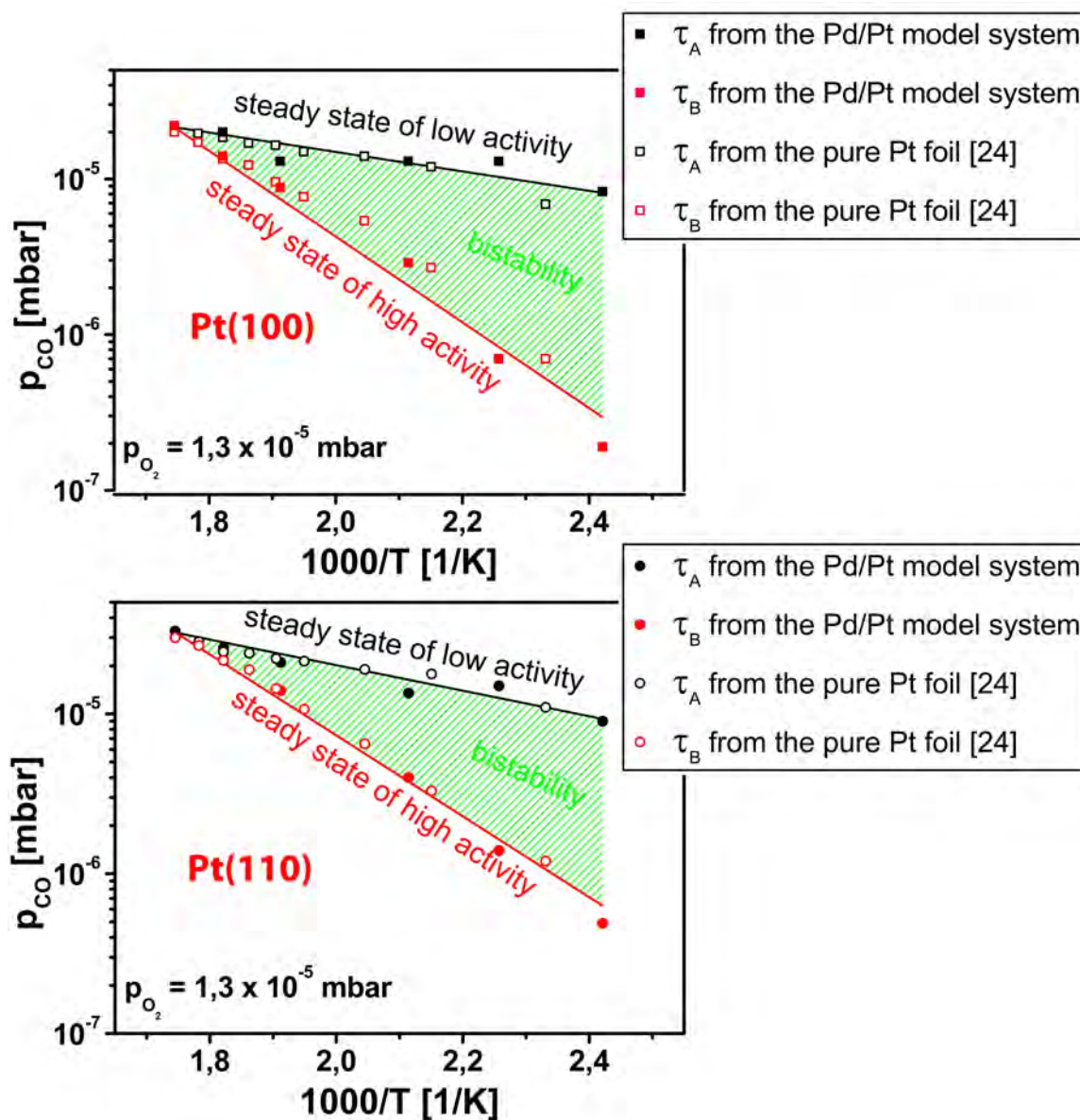


**Fig. 5.5:** Comparison of the the kinetic phase diagrams for Pt(100) and Pt(110) domains of the Pd/Pt model system with the previous results for a clean Pt foil:

The great agreement of the diagrams lead to the insight, that no coupling occurs between the different sample regions (e.g. Pt(100)), Pt(110) and Pd).

under the present conditions no coupling between the different regions of the combined sample could be observed within  $\mu m$  distances.

## 5.4 CO oxidation on the Pd part of the sample

In the present chapter the results concerning the CO oxidation reaction on the Pd-part of the sample are discussed. The first part of this chapter deals with the local kinetics of the CO oxidation reaction on the Pd powder agglomerates, the second part discusses the influence of the size and the shape on the kinetic behaviour of these powder agglomerates and in the third part the catalytic behaviour of the Pd/Pt model system is compared with other model systems containing Pd.

### 5.4.1 Local kinetics of CO oxidation on a Pd part of the combined sample

The CO oxidation experiments on the Pd/Pt sample were performed in order to evaluate the local kinetics for the Pt domains and for the Pd agglomerates under exactly the same reaction conditions. As shown in the previous chapter (see Fig. 5.3), kinetic transitions occur on Pd similar as they do on Pt, however, the transition points are observed at differing partial CO pressures. Similarly to the Pt part of the sample, also the Pd agglomerates are, at the beginning of the experiment, covered with oxygen, until the increasing partial CO pressure reaches a certain value, at which the CO adsorption becomes the preferred process in the competitive coadsorption with oxygen and the kinetic transition  $\tau_A$  from the high reactivity state to the low reactivity state occurs. The Pd agglomerates also show a similar behaviour to the Pt domains in the steady state of low reactivity: again, the reversed kinetic transition occurs at a differing values of  $\tau_B$ .

The analyses of the local kinetics for the Pd part of the sample were performed in the same way to the evaluation for the Pt domains (Chap. 5.3 Local kinetics of the CO oxidation on the Pt part of the sample). The bigger Pd powder agglomerate within the field of view shown in Fig. 5.6 which will be called *Pd I* in the following, was analysed by plotting the integrated image intensities within ROIs, whose sizes were  $75 \times 50 \mu m$ , as functions of the partial CO pressure. One important point is that the change of an oxygen-covered Pd surface to the CO-covered Pd surface increases the local work function (contrary to Pt, where CO adsorption decreases the work function) and, consequently, that the reversed transition decreases the local work function (again contrary to Pt surfaces, where this behaviour is opposite). This can be seen by a comparison of the PEEM intensity curves for Pt (Fig.5.4) and for Pd (Fig. 5.7) which belong both to the same experiment (cyclic variation of the CO preassure at 473 K and a partial oxygen pressure of  $1,3 \times 10^{-5} mbar$ ).

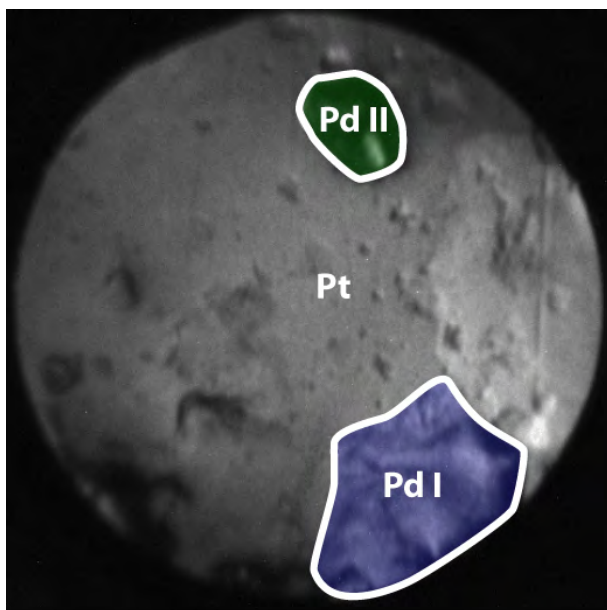


**Fig. 5.6:** PEEM field of view containing two Pd powder agglomerates (Pd I and Pd II).

To keep the same visual appearance of the hysteresis-like curves, the orientation of the PEEM intensity axis in the Fig. 5.7 was set in the opposite direction in comparison to Fig. 5.4.

The local transition points  $\tau_A$  and  $\tau_B$  for the Pd agglomerates can be evaluated by analysing the “steps” in the hysteresis-like PEEM intensity curve as described above for Pt.

The local transition points  $\tau_A$  and  $\tau_B$  for the Pd agglomerates can be evaluated by analysing the “steps” in the hysteresis-like PEEM intensity curve as described above for Pt and as it can be seen in Fig. 5.4: at the beginning of the experiment, the whole Pd surface is oxygen-covered (low work function, high brightness) and thus stays in the catalytic steady state of high reactivity (frame 1 and the corresponding point 1 on the plot). Similar to other Pt group metals, the dissociative adsorption of oxygen on Pd leaves enough free adsorption sites for CO so that an increase of the partial CO pressure leads to an increased CO adsorption rate which causes an increase of the CO<sub>2</sub> production rate. When the partial CO pressure reaches a certain value, CO becomes overbalanced in the competitive coadsorption with oxygen and dominates the adsorption process from now on. The following change of the surface coverage from oxygen-covered to CO-covered is the kinetic transition from the catalytically active to the inactive surface. The transition point  $\tau_A$ , where the image brightness decreases abruptly (due to the increase of the work function), is clearly visible in the PEEM intensity plot (frame 2 and the corresponding point 2 on the plot). Since oxygen can hardly adsorb on a CO-covered surface and both

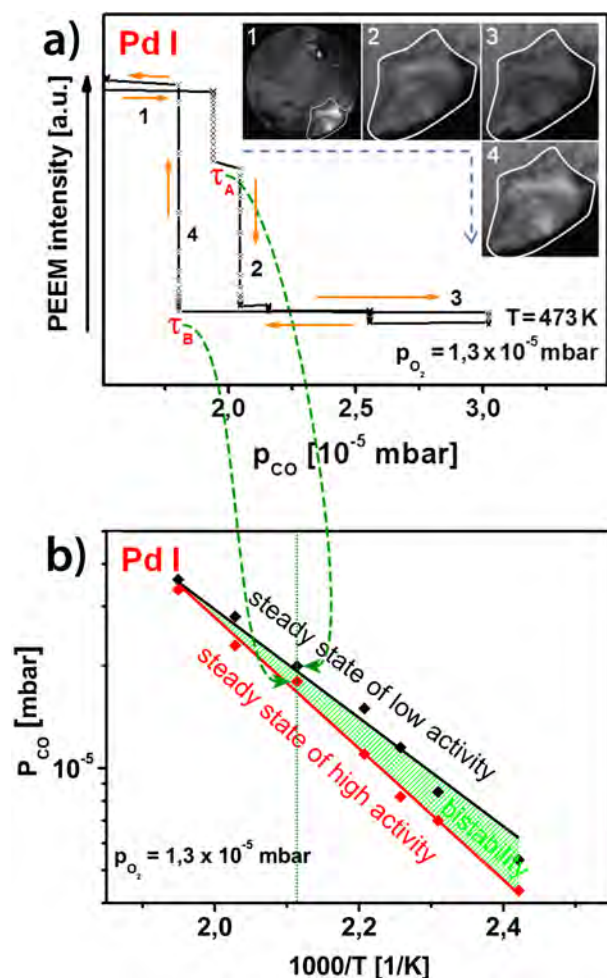


**Fig. 5.7:** Hysteresis plot for the local PEEM intensity for the Pd agglomerate Pd I and corresponding frames during the CO oxidation at a constant temperature with a cyclic variation of the CO pressure and the corresponding kinetic phase diagram:

a) At the beginning of the experiment the Pd powder agglomerate is oxygen-covered (low work function, high intensity, point 1 in the plot and frame 1), i.e. the sample is in the steady state of high reactivity. The kinetic transition from the oxygen-covered to the CO-covered surface occurs at  $\tau_A$  (increasing work function, decreasing brightness, point 2 in the plot and frame 2). A further increase of  $p_{CO}$  does not change the image brightness nor the  $CO_2$  production rate (high work function, low intensity, point 3 in the plot and frame 3). At the decreasing stage of the cyclic  $p_{CO}$  variation, oxygen prevails again in the competitive adsorption process and the kinetic transition back to the steady state of high reactivity occurs (increasing work function, decreasing brightness, point 4 in the plot and frame 4).

b) The transition points obtained from the hysteresis curve were used to construct the kinetic phase diagram for Pd I, which characterises its catalytic behaviour within a certain temperature and pressure range. The dotted line shows the isothermal variation of the partial CO pressure.

reactants have to adsorb before they react to  $CO_2$ <sup>35</sup>, the  $CO_2$  production rate decreases. Because the surface is already CO-covered, a further increase of the partial CO pressure neither changes the PEEM intensity nor the  $CO_2$  production rate significantly (see frame 3 and the corresponding point 3 on the plot). A reduction of the partial CO pressure to  $\tau_A$  does not lead to a change of the coverage because there are, similarly to Pt, still not enough pairs of free adsorption sites for a significant increase of the dissociative oxygen adsorption. For reaching the reversed transition point  $\tau_B$ , where oxygen prevails again in the competitive adsorption process (decrease of the work function, increase of the bright-

<sup>35</sup>See chapter 2.4 “The Langmuir-Hinshelwood mechanism of the CO oxidation reaction”.

ness), the pressure has to be further reduced (see frame 4 and the corresponding point 4 on the plot).

The transition points evaluated by analysing the obtained PEEM intensity curves can be combined in one plot named kinetic phase diagram. The corresponding diagram for Pd I is shown in Fig. 5.7.

The shapes of the kinetic phase diagrams for the Pt domains (shown in Fig. 5.4) and for Pd I (shown in Fig. 5.7) differ obviously. The diagrams for Pt(100) and Pt(110) are significantly broader than those for Pd and are additionally shifted to lower CO pressures. The clear differences between the diagrams indicate that not only the different Pt domains of the Pd/Pt model system retain their independence in respect to their catalytic reactivity in the CO oxidation reaction, but that also Pd agglomerates remain independent under the present conditions.

#### 5.4.2 The role of the size and shape of Pd agglomerates in the CO oxidation

Kinetic phase diagrams and hysteresis curves can be used to compare the catalytic properties of different surfaces. Since PEEM provides data for all regions within the field of view such diagrams can be measured locally for different regions of the same sample during one experiment to obtain a comparison of different surfaces at exactly the same reaction conditions. The catalytic behaviour of the two Pd powder agglomerates (Pd I and Pd II) which differ in size and shape can be compared. Figure 5.8 shows such a comparison for a measurement performed at a partial oxygen pressure of  $1,3 \times 10^{-5}$  mbar and at 473 K.

The quantitative agreement in the catalytic behaviour of the two different Pd agglomerates which is visible in Fig. 5.8b indicates that differences in size and shape in the  $\mu\text{m}$ -range have no influence on the reactivity of the catalytically active Pd powder.

Kinetic phase diagrams cannot only be obtained from isothermal measurements via a cyclic variation of the CO pressure (following the vertical line in the diagram in Fig. 5.7), but also from isobaric measurements, where the temperature is cyclically changed (following the horizontal line in the diagram in Fig. 5.9). This type of experiments is also called ignition-extinction measurements. During an ignition experiment the “cold” sample is heated up at constant partial pressures of oxygen and CO, until the catalytic ignition (sudden increase of the CO<sub>2</sub> rate) takes place. Afterwards, the temperature decreases

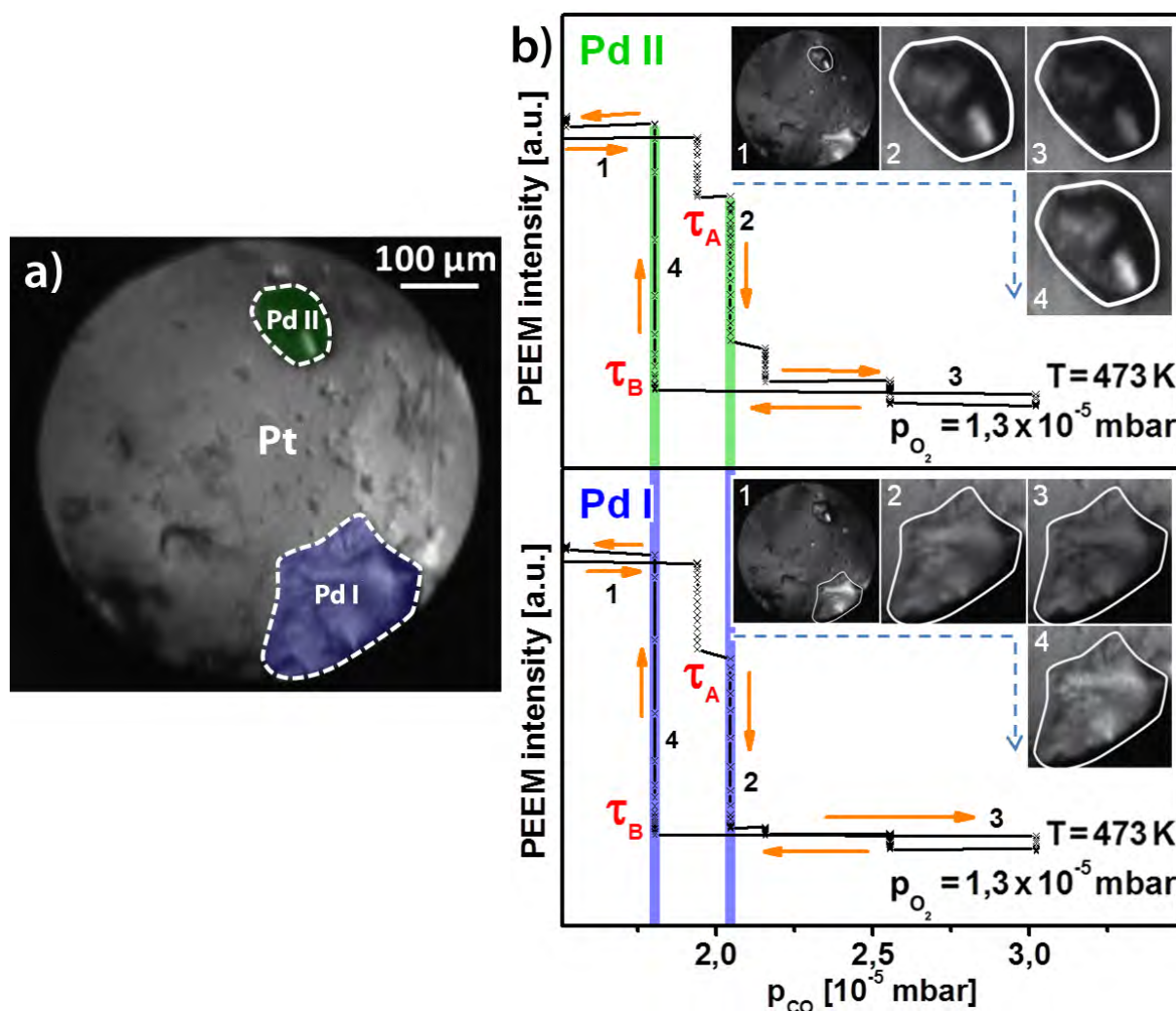


**Fig. 5.8:** Comparison of the catalytic behaviour of two different Pd agglomerates under exactly the same reaction conditions:

a) The PEEM image of the sample region contains two Pd powder agglomerates (Pd I and Pd II).

b) The locally measured hysteresis-like PEEM intensity plots obtained by a cyclic variation of the CO pressure at constant temperature of 473 K and a constant partial oxygen pressure of  $1,3 \times 10^{-5}$  mbar. Additionally to the local PEEM intensities, also corresponding frames are shown.

again to evaluate the catalytic extinction. Such experiments model the behaviour of a three-way automotive catalyst at “cold start” and are therefore, of practical importance. Figure 5.9 shows a PEEM intensity curve from such an ignition-extinction experiment as a function of temperature and corresponding PEEM-snapshots. The measurement was performed at a constant partial oxygen pressure of  $1,3 \times 10^{-5}$  mbar and a constant partial

CO pressure of  $8,2 \times 10^{-6}$  mbar. The temperature was changed cyclically from 353 to 613 K and vice versa with a rate of 0,6 K/s. The ROIs placed inside the Pd powder agglomerate were  $80 \times 80 \mu\text{m}$ .

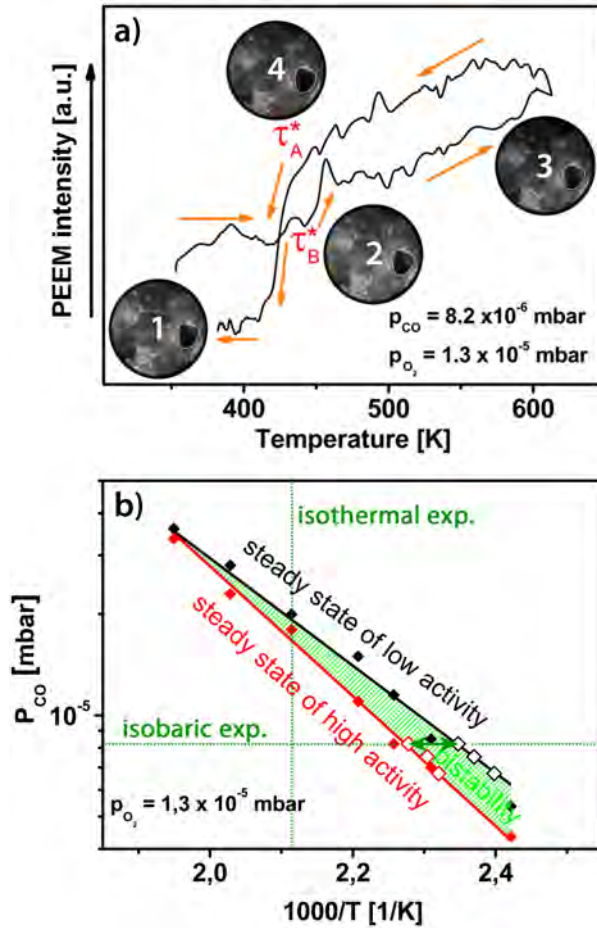


**Fig. 5.9:** Ignition-extinction experiments in the CO oxidation on the Pd part of the sample:

a) Hysteresis plot for the local PEEM intensity of the Pd part of the sample at constant partial oxygen and partial CO pressure and during a cyclic variation of the temperature. At the beginning of the experiment the Pd powder surface is CO-covered (high work function, low intensity, frame 1), i.e. the sample is in the steady state of low reactivity. The kinetic transition from the CO-covered to the oxygen-covered surface occurs at  $\tau_B^*$  (decreasing work function, increasing brightness, frame 2). A further increase of the temperature changes the image brightness, but the sample remains in the steady state of high reactivity (still low work function, high intensity, frame 3). During the decreasing part of the cyclic temperature variation the reversed transition to the steady state of low reactivity occurs at  $\tau_A^*$ .

b) The kinetic phase diagram is equal to Fig. 5.7b but the transition points  $\tau_A^*$  and  $\tau_B^*$  obtained from the ignition-extinction hysteresis-like curves are added. The points added agree with the kinetic phase diagram obtained from isobaric measurements. The dotted lines show one isobaric variation of the temperature and one isothermal variation of the pressure.

At the beginning of the experiment the “cold” sample surface is CO-covered (high work function, low brightness) and thus is in the catalytic steady state of low reactivity (frame 1). Following the temperature ramp, CO starts to desorb from the surface. Due to enhanced oxygen adsorption, the isobaric kinetic transition  $\tau_B^*$  (frame 2) from the CO-covered surface to the oxygen-covered surface occurs. Due to the change of the coverage from CO to oxygen (decrease of the local work function), the image brightness increases significantly, as it can be seen at  $\tau_B^*$  in Fig. 5.9. Raising the temperature further increases

the image brightness, but the sample still remains in the steady state of high reactivity (frame 3). During the descending part of the cyclic temperature variation the surface remains in the steady state of high reactivity till the kinetic transition occurs at  $\tau_a^*$ . At the transition point  $\tau_A^*$  the catalytic extinction takes place, i.e. CO prevails again in the competitive adsorption process and the sample transits back into the steady state of low reactivity (frame 4). The catalytic extinction is reflected in an abrupt drop of the PEEM intensity in the hysteresis-like curve, as shown in Fig. 5.9a.

The obtained transition points  $\tau_A^*$  and  $\tau_B^*$  accurately match the kinetic phase diagram shown in Fig. 5.7b. Therefore, it can be suggested that both the isothermal and the isobaric procedure to obtain a kinetic phase diagram provide the same results, at least for the CO oxidation under the present conditions.

### 5.4.3 Reaction front propagation during the catalytic CO oxidation on Pd

It is known that reaction fronts occur in heterogeneous catalysed processes on different flat catalytically active surfaces, e.g. on the surface of single crystals [7] or on domains of polycrystalline foils [15]. However, the observation of the reaction front propagation on catalytic powder samples has not been reported yet.

#### 5.4.3.1 Reaction fronts

The mathematical models of reaction-diffusion systems are often used to model the propagating fronts of differently phases within a system, e.g. the border between burnt and unburnt trees in a forest fire, the spreading of epidemics or the border between different covered surface areas during the CO oxidation reaction. A reaction-diffusion system can be described by the nonlinear differential equation

$$\underbrace{\frac{\partial c_i}{\partial t}}_{\text{Concentration}} = \underbrace{F_i(\lambda, \vec{c})}_{\text{Reaction}} + \underbrace{D_i \frac{\partial^2 c_i}{\partial x^2}}_{\text{Diffusion}} \quad (5.1)$$

where  $\vec{c}$  is a vector containing the various concentrations of participating chemical species,  $F_i$  contains information about the kinetics of the species  $i$ ,  $\lambda$  is a set of parameters like partial pressures or temperatures and  $D_i$  contains information about the diffusion processes of the species  $i$  [25].

According to Ref. [26], the reaction-diffusion system of the CO oxidation on a metal

## 5 CO oxidation reaction on the Pd/Pt model system

surface can be described by eq. (5.2) for CO and e.q. (5.3) for oxygen, where the concentration is represented by the surface coverage  $\Theta$ . In both equations  $D$  is the diffusion coefficient,  $k_{ads.}$  the adsorption rate,  $p$  the partial pressure,  $k_{des.}$  the desorption rate and  $k_{reaction}$  the reaction rate.

$$\underbrace{\frac{\partial}{\partial t} \Theta_{CO}}_{\text{Concentration}} = \underbrace{D_{CO} \cdot \frac{\partial^2}{\partial r^2} \Theta_{CO}}_{\text{Diffusion}} + \underbrace{k_{ads. CO} \cdot p_{CO} \cdot s_{CO} \cdot [1 - (\frac{\Theta_{CO}}{\Theta_{CO max}})^3]}_{\text{Adsorption}} - \underbrace{k_{des. CO} \cdot \Theta_{CO}}_{\text{Desorption}} - \underbrace{k_{reaction} \cdot \Theta_{CO} \cdot \Theta_O}_{\text{Reaction}} \quad (5.2)$$

In the case of the surface-catalysed CO oxidation reaction the diffusion rate of CO is far higher than that of oxygen. Therefore, the diffusion process of oxygen can be neglected.

$$\underbrace{\frac{\partial}{\partial t} \Theta_O}_{\text{Concentration}} = \underbrace{0}_{\substack{\text{Diffusion} \\ \text{of oxygen} \\ \text{is neglected}}} + \underbrace{k_{ads. O} \cdot p_O \cdot s_O \cdot (1 - \frac{\Theta_{CO}}{\Theta_{CO max}} - \frac{\Theta_O}{\Theta_{O max}})^2}_{\text{Adsorption}} - \underbrace{k_{reaction} \cdot \Theta_{CO} \cdot \Theta_O}_{\text{Reaction}} \quad (5.3)$$

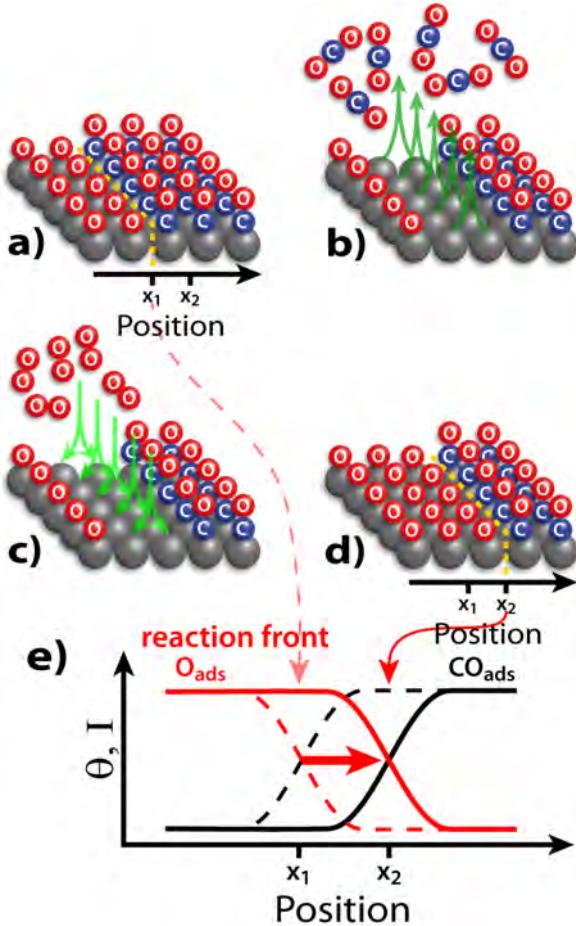


**Fig. 5.10:** Formation of a reaction front in the CO oxidation reaction on Pd:

a) The left-hand part of the surface is oxygen-covered, while the right-hand part is CO-covered. The line between the CO- and the oxygen-covered surface marks the reaction front (position  $x_1$ ).

b) The atomic oxygen and the CO-molecules adsorbed along the reaction front react forming  $\text{CO}_2$ , which desorbs immediately, leaving free lattice sites behind.

c) Oxygen adsorbs dissociatively at free adsorption sites, because due to the reaction conditions oxygen adsorption is the preferred process in the competitive coadsorption with CO.

d) The reaction front has moved from position  $x_1$  to  $x_2$ .

e) The same but in terms of  $\Theta$  (coverage) and  $I$  (PEEM brightness in the case of a Pd surface).

The origin of the reaction front during the CO oxidation is schematically depicted in Fig. 5.10. In Fig. 5.10a the main part of the surface is CO-covered, while only a small part is oxygen-covered. The border line between the CO-covered and the oxygen-covered part of the surface marks the reaction front. The CO-molecules and the adjacently bound atomic oxygen next to them react with each other and desorb as  $\text{CO}_2$ . Each  $\text{CO}_2$  formed leaves two free lattice sites behind (Fig. 5.10b). Because the dissociative adsorption of oxygen is due to the reaction conditions the preferred process in the competitive co-adsorption with CO, oxygen adsorbs dissociatively on the free adsorption sites (Fig. 5.10c). Thus the part of the oxygen-covered surface increases and the reaction front moves from position  $x_1$  to  $x_2$  (Fig. 5.10d). When the oxygen-covered surface increases, as it happens during the kinetic transition  $\tau_B$ , the reaction front is called “oxygen front”. In turn, during  $\tau_A$ , the CO-covered surface propagates at the expense of the oxygen-covered surface. In this case the “CO front” propagates.

The reaction front can be monitored by PEEM due to the differences between the local work functions of the CO- and oxygen-covered surface. Therefore, the position of the reaction front is well visible in PEEM, as shown in Fig. 5.11.

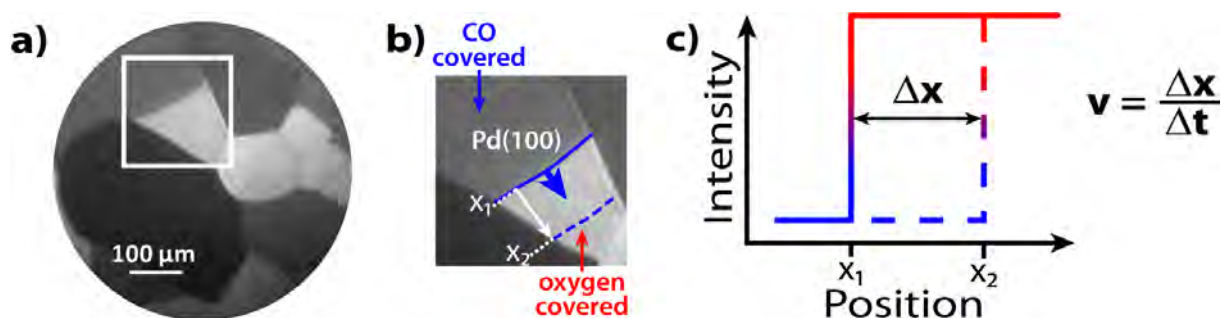


**Fig. 5.11:** Reaction front propagation on a Pd foil:

a) An in situ PEEM snapshot of a polycrystalline Pd foil which was taken during the kinetic transition  $\tau_B$  from the steady state of high reactivity to the steady state of low reactivity; the analysed area has been marked.

b) The dark regions of the Pd foil are CO-covered, while the bright parts are oxygen-covered. The CO-front has been marked with a continuous blue line. The CO-covered surface is spreading from position  $x_1$  towards the blue dashed line in position  $x_2$ .

c) The schematically drafted local image intensities for the frame shown in b and the frame, where the reaction front reached the dashed line are shown in one graph. Positions  $x_1$  and  $x_2$  can be detected due to the “steps” in the intensity curve. From the distance  $\Delta x$  between  $x_1$  and  $x_2$  the velocity of the reaction front can be calculated.

By evaluating the position of the reaction front on different PEEM video frames taken during the CO oxidation experiment, it is possible to obtain information about the reac-

tion front propagation. Since the time between the frames is known, the velocity of the reaction front can be obtained. In the case of Pd the oxygen-covered surface has a higher brightness than the CO-covered part of the sample. Therefore, the local change of the reaction front can be determined by analysing the positions of the “brightness steps” in a diagram which shows the PEEM intensity as a function of the position, as shown in Fig. 5.11: e.g. the reaction front (continuous blue line in Fig. 5.11b) moves from position  $x_1$  towards the blue dashed line in position  $x_2$ . Figure 5.11c schematically shows the PEEM intensity curves and the distance  $\Delta x$ , the oxygen front has moved from its way from  $x_1$  to  $x_2$ . Since the time period which the reaction front needs to pass this distance is known, the velocity of the reaction front can easily be calculated as

$$v = \frac{\Delta x}{\Delta t} \quad (5.4)$$

where  $v$  is the average velocity of the reaction front propagation,  $\Delta x$  is the distance between the two positions of the reaction fronts evaluated from different PEEM frames and  $\Delta t$  denotes the time period between the two frames concerning the used PEEM intensity curves.

#### 5.4.3.2 Reaction fronts on Pd samples with different morphologies

During the study of the Pd/Pt system reaction fronts were observed on the Pt part of the sample, but they could also be observed on the surface of the Pd powder agglomerates. Using the method described above, it was possible to study these fronts as well and evaluate their velocities. Exemplary the oxygen front propagation on Pd I during an isothermal measurement at 413  $T$  and a partial oxygen pressure of  $1,3 \times 10^{-5}$  mbar is shown in Fig. 5.12 on the next page.

Figure 5.12a shows a PEEM-snapshot of the surface including the Pd I agglomerate during the kinetic transition  $\tau_B$ , Fig. 5.12b shows the position of the reaction front on Pd I at three different moments (0 s was chosen arbitrarily) and Fig. 5.12c shows three resulting intensity curves at 0, 3 and 10 s. The corresponding “intensity steps” in the curves refer to the current positions of the reaction front. From these positions and e.q. (5.4) the velocity of the oxygen front was obtained as 3,1  $\mu\text{m}/\text{s}$  under these conditions.

The observed behaviour of the reaction fronts on the Pd/Pt sample was compared with the results for the Pd/Al<sub>2</sub>O<sub>3</sub> sample and with the results for two sputtered domains of a clean Pd foil. Both domains are part of the same clean Pd foil and the same Pd powder was used to prepare the two different powder samples (with Pt and Al<sub>2</sub>O<sub>3</sub> as support).

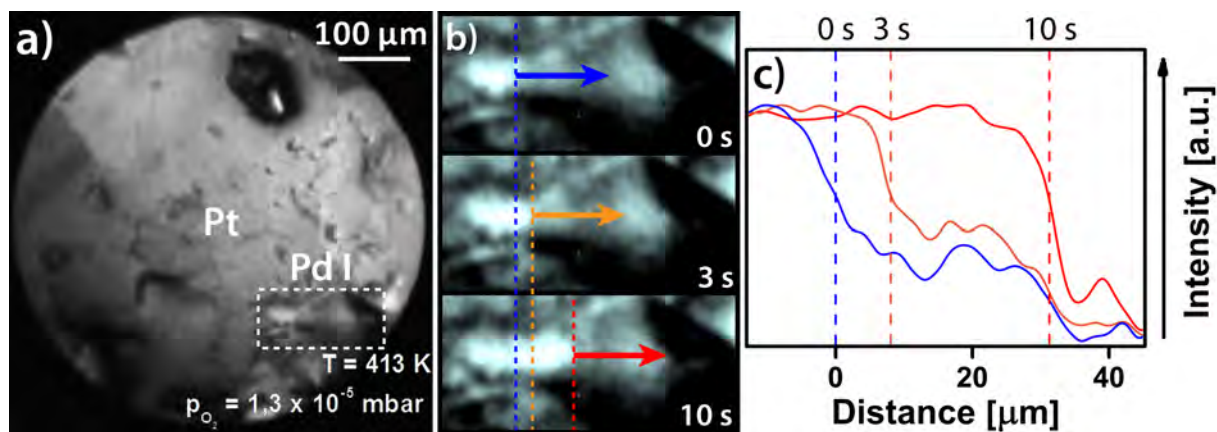


**Fig. 5.12:** Oxygen front on a Pd powder agglomerate:

- The PEEM-snapshot made while the oxygen front is propagating on the Pd I agglomerate marked at 413  $T$  and a partial oxygen pressure of  $1,3 \times 10^{-5}$  mbar.
- The moving reaction front. The contrast was artificially enhanced to show the propagation of the bright oxygen front more clearly.
- The PEEM intensity along a line following the reaction front propagation.

Figure 5.13 shows the comparison of the velocities of CO fronts and oxygen fronts on the sputtered Pd(100) and Pd(110) domain during the CO oxidation reaction with the corresponding reaction fronts on the Pd part of the Pd/Al<sub>2</sub>O<sub>3</sub> sample and on the Pd part of the Pd/Pt sample. All experiments were performed at similar reaction conditions, e.g. partial oxygen pressures and partial CO pressure ramps were identical.

The comparison of the CO front velocities in Fig. 5.13a shows the difference between the CO front velocities on the sputtered Pd foil and on the powder samples: within the studied temperature range the CO front velocity on the sputtered surfaces increases significantly with the temperature, while the CO front velocity increases only a little bit on the powder surface of the Pd/Pt sample and remains nearly constant on the powder surface of the Pd/Al<sub>2</sub>O<sub>3</sub> sample. Further, the velocities of the CO fronts moving on the Pd/Pt sample are higher than those on the Pd/Al<sub>2</sub>O<sub>3</sub> sample.

Analogous to Fig. 5.13a, Fig. 5.13b shows the comparison of the four measured oxygen fronts. Contrary to the CO fronts, all the velocities remain more or less constant within the studied temperature range. Only the oxygen front velocity on the Pd part of the Pd/Pt sample increases slightly (this increase can be seen more clearly in Fig. 5.13d). Furthermore, it can be said, that the oxygen fronts move faster on the sputtered surfaces within the measured temperature range than on the Pd powder samples and the oxygen fronts on the Pd/Pt sample are slower than those on the Pd/Al<sub>2</sub>O<sub>3</sub> sample.

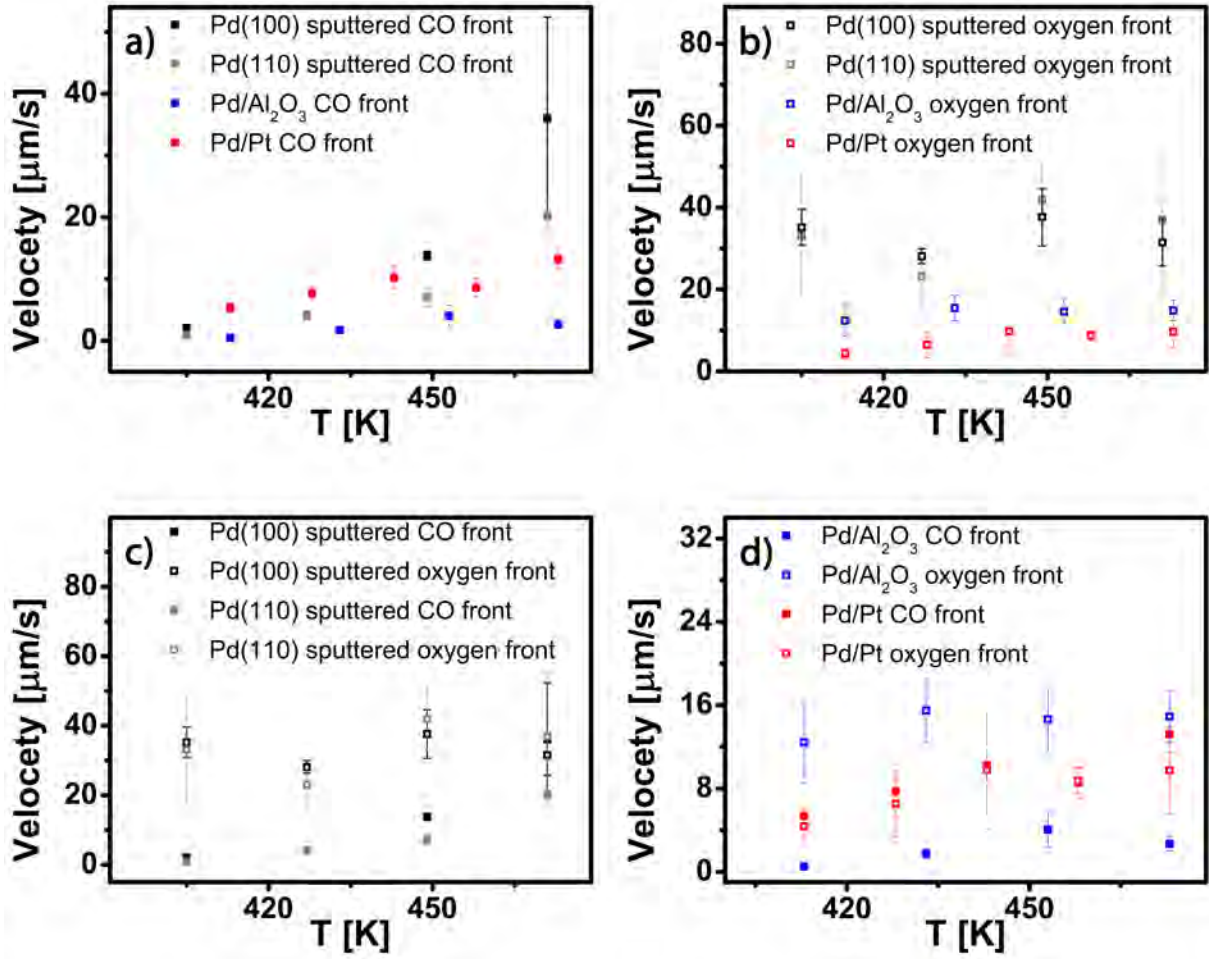


**Fig. 5.13:** Comparison of the velocity of the reaction fronts during CO oxidation experiments in a temperature range of 405 to 473 K on different Pd samples:

a) While the velocity of the CO front on two sputtered Pd domains of the same polycrystalline foil increases significantly within this temperature range, its velocity on the Pd/Pt surface increases only slightly and the velocity on Pd/Al<sub>2</sub>O<sub>3</sub> remains approximately constant within the temperature range studied. The velocity of the CO fronts occurring on the Pd/Pt sample is generally higher than those on the Pd/Al<sub>2</sub>O<sub>3</sub> sample.

b) Within this temperature range the velocity of the oxygen fronts remains approximately constant on almost all samples: only the velocity of the oxygen front on the Pd/Pt sample increases significantly. Within the temperature range measured the oxygen fronts move faster on the sputtered surfaces than on the powder surfaces. Contrary to the velocities of the CO fronts on the combined samples, the oxygen fronts on the Pd/Al<sub>2</sub>O<sub>3</sub> sample move faster than those on the Pd/Pt sample.

c) The velocities of the CO and oxygen fronts on the sputtered Pd domains differ significantly at 405 K, but they are nearly equal at 449 K.

d) The velocities of the CO and the oxygen front on Pd/Al<sub>2</sub>O<sub>3</sub> differ much less on Pd/Al<sub>2</sub>O<sub>3</sub>. Additionally, only on the Pd/Pt system the CO front moves faster than the oxygen front.

In Fig. 5.13c both reaction fronts (CO and oxygen) on the sputtered Pd foil are compared. Within the temperature range studied the velocities of the oxygen fronts seem to be independent of the temperature, while the velocities of the CO front increase significantly with the temperature.

Analogous to Fig. 5.13c, Fig. 5.13d shows the comparison of the CO and the oxygen reaction fronts on the Pd powder surfaces of the combined samples. The most obvious result is that the CO and oxygen fronts on the Pd/Pt system behave more similar to each other than those on the Pd/Al<sub>2</sub>O<sub>3</sub> surface. It is also worth mentioning that on the Pd/Pt system CO fronts move faster than the oxygen fronts.

It is hardly possible to explain all these observations without the corresponding theoretical modelling. However, it should be noticed that the surface of powder agglomerates contains various steps and defects. Because sputtering of a clean surface forms lots of artificially created steps and defects, a sputtered sample surface should provide a similar morphology as a pressed powder surface does. Therefore, also their catalytic behaviour should be similar, if there is no interaction between the powder and the support.

Nevertheless, it can be said that the obvious differences in the behaviour of the reaction fronts analysed indicate that there is a significant influence of the supporting material on the catalytically active powder, which influences also the velocity of the CO front and the oxygen front in the catalysed CO oxidation reaction.

#### 5.4.4 Comparison of the CO oxidation on Pd samples of different morphology

In the previous chapter, it was shown that there are differences in the behaviour of the reaction fronts occurring on the different Pd samples which might refer to the different supports. In this chapter the catalytic reactivity of some samples (Pd foil, Pd/Al<sub>2</sub>O<sub>3</sub> and Pd/Pt) and the role of their supports on their catalytic reactivity are compared and discussed. Therefore, similarities and differences between their kinetic phase diagrams were studied. Contrary to the locally measured kinetic phase diagrams for the Pd/Pt sample, the other two diagrams (for Pd/Al<sub>2</sub>O<sub>3</sub> and a sputtered Pd foil) were measured globally by evaluating the CO<sub>2</sub> production rate as a function of the partial CO pressure, as it was described in Chap. 5.2 Global kinetic behaviour of the CO oxidation reaction catalysed by the Pd/Pt model system. As already mentioned, such global measurements were not possible in the case of the Pd/Pt surface since Pt is, contrary to Al<sub>2</sub>O<sub>3</sub>, catalytically active and “overlaps” the activity of Pd.

Although the sputtered Pd surface, which has lots of artificial steps and defects, and a Pd powder surface are in a certain sense similar, the comparison between the kinetic phase diagrams for a Pd powder impregnated into an Al<sub>2</sub>O<sub>3</sub> foil and for a sputtered Pd foil reveals significant differences, as it can be seen in Fig. 5.14.

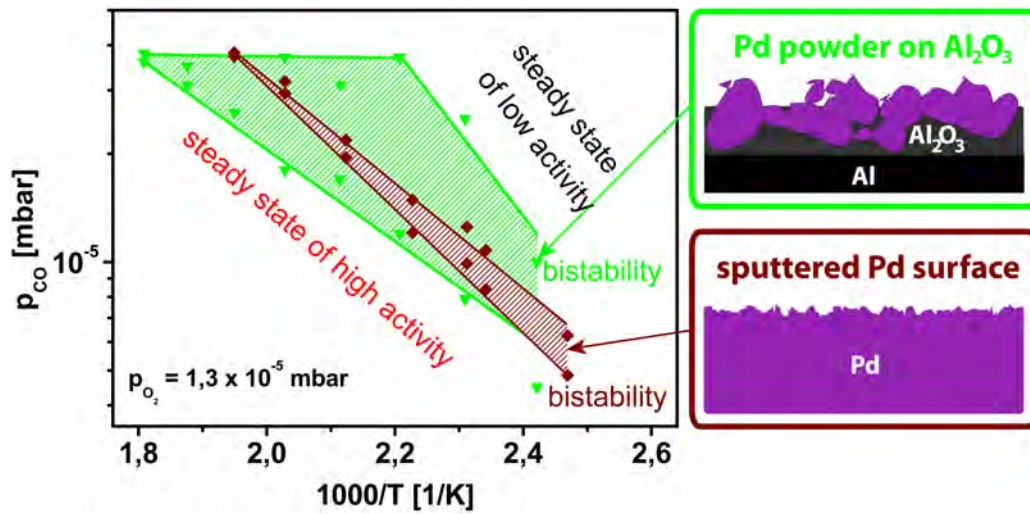


**Fig. 5.14:** Comparison between the catalytic behaviour of Pd powder impregnated into an  $Al_2O_3$  foil and a clean sputtered Pd foil: The shape of the kinetic phase diagram of the Pd/ $Al_2O_3$  sample and of the sputtered Pd foil differ significantly.

The striking difference indicates that the similar morphology of a sputtered surface and a powder agglomerate is not sufficient for a similar catalytic behaviour and that there is a significant influence of the  $Al_2O_3$  support on the catalytic behaviour of the Pd powder. In Fig. 5.15 the catalytic behaviour of the two different powder samples (Pd/Pt and Pd/ $Al_2O_3$ ) is compared by contrasting their kinetic phase diagrams.

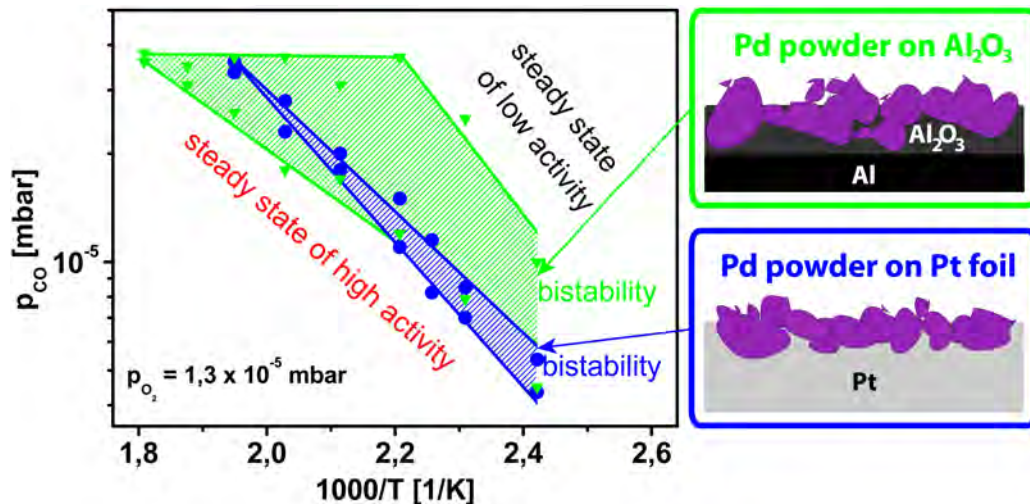


**Fig. 5.15:** Comparison of the catalytic behaviour of a Pd/ $Al_2O_3$  and a Pd/Pt model system: The difference in the shape of the kinetic phase diagrams of the Pd/ $Al_2O_3$  sample and the Pd/Pt sample is still significant.

As the same Pd powder was impregnated with the same procedure into the two different metal foils ( $\text{Al}_2\text{O}_3$  and Pd) and the reaction conditions during the measurements were nearly the same, only the interaction between the supports and the powder could lead to differences between the kinetic phase diagrams.

Finally, the kinetic phase diagrams for a sputtered Pd foil and the Pd agglomerates of the Pd/Pt model system were compared, which is also shown in Fig. 5.16.

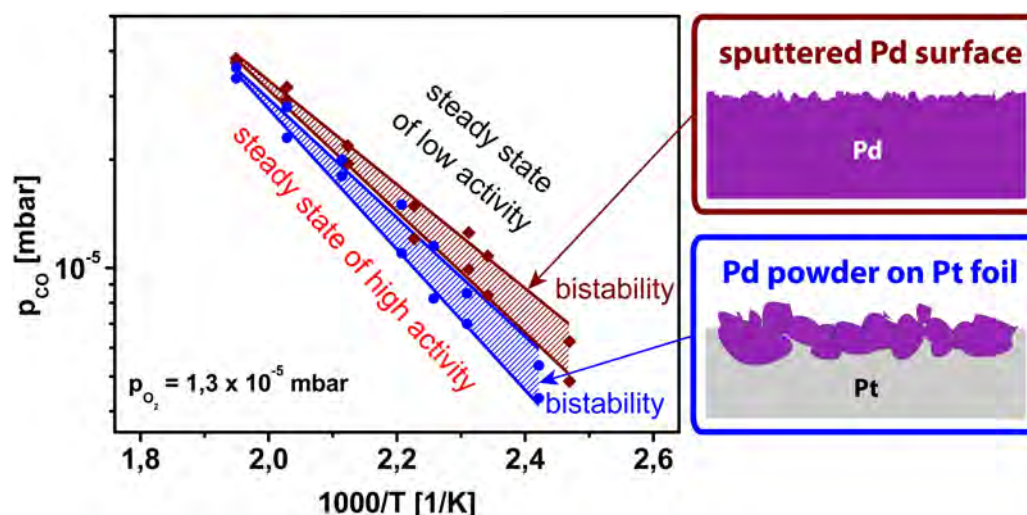


**Fig. 5.16:** Comparison between the catalytic behaviour of a clean sputtered Pd foil and that of the Pd/Pt model system:

The good agreement between the two kinetic phase diagrams indicates that the influence of the metallic support (Pt) on the catalytic behaviour of Pd powder is rather small. The small shift between the diagrams might result from differences between the Pd powder and the sputtered Pd foil morphology.

Considering the results from Fig. 5.14, Fig. 5.15 and Fig. 5.16, a few conclusions can be suggested:

1. The phase diagram of the Pd powder on  $\text{Al}_2\text{O}_3$  differs strongly from the phase diagrams for the sputtered Pd surface and for the Pd powder on Pd.
2. The phase diagram for the Pd powder supported by metallic Pd differs only slightly from that for the sputtered Pd. The differences apparently result from the differing morphologies, because the metallic support, although it is catalytically active itself, hardly influences Pd powder.
3. Contrary to metallic Pt, the oxidic support ( $\text{Al}_2\text{O}_3$ ) significantly influences the catalytic properties of the impregnated Pd powder: the isobaric width of the bistability region is much wider for the Pd/ $\text{Al}_2\text{O}_3$  than for the Pd/Pt system, i.e. the Pd/ $\text{Al}_2\text{O}_3$  system remains catalytically active at significantly lower temperatures than the Pd/Pt system.

# 6

## Summary and Conclusions

---

In the present thesis the heterogeneous catalysed CO oxidation reaction was studied using different Pd/Pt model system samples by UV-PEEM. The questions to be answered were about the factors influencing the reaction, like the role of the supporting material, the influence of the morphology of the catalytically active surface or of the size and shape of powder agglomerates on the catalytic behaviour of the catalyst in the CO oxidation reaction. These questions could be answered by comparing the results for the Pd/Pt system with two other model systems: Pd/Al<sub>2</sub>O<sub>3</sub> and a Pd foil with artificially created defect sites, formed by Ar<sup>+</sup> sputtering.

By comparing literature data for clean and adsorbate-covered low Miller index Pt planes with PEEM images of the clean, oxygen-covered and CO-covered surface of the Pd/Pt sample, a Pt(100) and a Pt(110) domain could be localised on the combined Pd/Pt sample next to two Pd powder agglomerates which differ in size and shape in the  $\mu m$ -range. Therefore, it was possible to use PEEM to obtain simultaneously information about the catalytic behaviour of impregnated Pd powder agglomerates and the two low Miller index Pt domains in the CO oxidation reaction at exactly the same reaction conditions.

The CO oxidation reaction was studied at a constant partial oxygen pressure of  $1,3 \times 10^{-5}$  mbar, within a partial CO pressure range of  $4 \times 10^{-6}$  to  $3 \times 10^{-5}$  mbar and within a temperature range of 413 to 553 K. Under these conditions the Pd parts of the samples studied show a bistable catalytic behaviour. The kinetic behaviour of the three model systems (Pd/Pt, Pd/Al<sub>2</sub>O<sub>3</sub> and sputtered Pd foil) in the CO oxidation reaction were analysed by local (PEEM) studies of the chosen sample regions and global (QMS) measurements during isothermal experiments, where the partial oxygen pressure remained constant while the partial CO pressure was changed cyclically. Additionally, isobaric cat-

## 6 Summary and Conclusions

alytic ignitions and catalytic extinctions for the Pd powder agglomerates were studied. Catalytic ignition experiments simulate a “cold-start” of a real catalyst by heating up the “cold” sample under isobaric reaction conditions until the catalytic ignition takes place, i.e. until the system “jumps” from the steady state of low reactivity to the steady state of high reactivity. Afterwards the temperature is reduced again to study the reversed kinetic transition which is also called extinction.

The kinetic transition points for the Pd powder agglomerates and for the two localized Pt domains from the Pd/Pt sample were determined by analysing the plots of the corresponding local PEEM image intensity as a function of the partial CO pressure (for isothermal experiments) or temperature (for the ignition-extinction experiments). From these transition points local kinetic phase diagrams for individual regions were obtained. Three kinetic phase diagrams for the CO oxidation reaction on the Pd powder agglomerates, the Pt(100) and the Pt(110) domain were obtained from measurements on the Pd/Pt model system. Although the kinetic phase diagrams for the Pd and the Pt part of the sample differ significantly, the diagrams for the Pt domains of the Pd/Pt sample and the corresponding diagrams for Pt planes of the same crystallographic orientation of a pure Pt foil are in good agreement. Therefore, it can be concluded that both parts of the Pd/Pt model system retain their independence in respect to the catalytic CO oxidation, at least within the pressure range studied.

The influence of differences in the size and shape (in the  $\mu\text{m}$ -range) of Pd powder agglomerates on their catalytic reactivity was investigated by comparing the catalytic behaviour of two differing Pd agglomerates. The equal catalytic behaviour of both Pd agglomerates indicates that variations of size and shape in the  $\mu\text{m}$ -scale have no influence on the catalytic reactivity. It was also shown that transition points obtained from ignition-extinction measurements lead to the same kinetic phase diagrams as those obtained from isothermal measurements.

The reaction fronts which propagate during the heterogeneous catalysed processes on different flat catalytically active surfaces, e.g. single crystals or domains of polycrystalline foils, have not been reported yet on powder samples. In the present study, such fronts were observed for the first time for the Pd powder supported by Pd foil and  $\text{Al}_2\text{O}_3$ . The evaluated velocities of the reaction fronts on the Pd part of the Pd/Pt sample and the Pd part of the  $\text{Al}_2\text{O}_3$  sample were compared to those on a sputtered Pd foil. Due to its artificially created steps and defects a sputtered surface is similar to a powder surface and therefore, a similar catalytic behaviour might be expected. But the comparison between the evaluated reaction front velocities shows significant differences indicating that the supports have a substantial influence on the propagation of the reaction fronts during the CO oxidation.

Finally, the comparison of the three kinetic phase diagrams (sputtered Pd foil, Pd part of the Pd/Pt sample and Pd part of the Pd/ $\text{Al}_2\text{O}_3$  sample) leads to the insight that the Pt

## 6 *Summary and Conclusions*

foil hardly influences the reactivity of the impregnated Pd powder, while the metal-oxide interaction between the Pd powder and the  $\text{Al}_2\text{O}_3$  foil remarkably influence the catalytic behaviour of the impregnated Pd powder. Further, the differences between the morphology of a sputtered Pd surface and pressed Pd powder shift the kinetic phase diagram for the CO oxidation to lower partial CO pressures.

## List of figures

---

1.1	Catalytic CO oxidation reaction on platinum group metals is studied on simplified model systems . . . . .	4
1.2	Complexity axis . . . . .	5
1.3	Energy diagram of the chemical reaction $A + B \rightarrow AB$ with and without using a catalyst . . . . .	6
2.1	Three-way catalyst . . . . .	10
2.2	Adsorption . . . . .	11
2.3	Principle of the Langmuir Hinshelwood mechanism . . . . .	13
2.4	Langmuir-Hinshelwood mechanism . . . . .	14
2.5	Schema of the hysteresis of the CO <sub>2</sub> production rate in the catalytic CO oxidation during cyclic variation of the CO pressure and its bistability behaviour . . . . .	16
2.6	Kinetic phase diagram . . . . .	17
3.1	Front of the experimental setup . . . . .	19
3.2	Back of the experimental setup . . . . .	20
3.3	Scheme of the experimental setup . . . . .	21
3.4	Model system sample and transfer tool . . . . .	23
3.5	View through a CF40 window into the XPS-chamber . . . . .	24
3.6	View through a CF40 window into the PEEM-chamber . . . . .	25
3.7	Working principle of an XPS . . . . .	26
3.8	Energy diagram of the photoeffect . . . . .	27
3.9	Principle of the emission of a characteristic X-ray photon or a KLM-Auger-electron . . . . .	28
3.10	Working principle of an XPS-analyser . . . . .	29
3.11	The universal inelastic mean free path curve . . . . .	30
3.12	Relation between the number of photo electrons emitted from a metal, their mean free path and their depth . . . . .	31
3.13	Angle-resolved XPS . . . . .	32
3.14	Schematic cross section of a Hemispherical Electron Energy Analyser . . . . .	33
3.15	The XPS-spectrum . . . . .	36
3.16	Example of chemical shift and peak fitting . . . . .	37

3.17	General scheme of a photoelectron spectrum. . . . .	38
3.18	Scheme of the contrast formation in PEEM. . . . .	39
3.19	Layout of a UV-PEEM . . . . .	40
3.20	Propagation of reaction fronts during the catalytic CO oxidation on a platinum foil. . . . .	42
3.21	Working principle of a QMS . . . . .	43
3.22	Deflection of particles in the quadrupole field whose mass-to-charge-ratio is too small . . . . .	45
3.23	Deflection of particles in the quadrupole field whose mass-to-charge-ratio is too big . . . . .	46
3.24	Working principle of an SEM . . . . .	47
3.25	Working principle of a channeltron . . . . .	48
3.26	Channeltron in the <i>off axis</i> geometry . . . . .	49
4.1	Surface crystallography of Pt and Pd and their adsorption sites for CO . .	51
4.2	XPS-spectra of the clean sample surface . . . . .	53
4.3	Composition of the sample . . . . .	53
5.1	Plot of the global production rate of CO <sub>2</sub> as a function of the partial CO pressure . . . . .	55
5.2	A section of the Pd/Pt model system sample imaged by PEEM. . . . .	56
5.3	PEEM snapshots of the kinetic transitions during the CO oxidation on the Pd/Pt model system at 473 K and a partial oxygen pressure of $1,3 \times 10^{-5}$ mbar. . . . .	57
5.4	Hysteresis plots for the the local PEEM intensity of Pt(100) and Pt(110) domains during the CO oxidation at a constant temperature by a cyclic variation of the CO pressure and the corresponding kinetic phase diagrams . . . . .	59
5.5	Comparison of the the kinetic phase diagrams for Pt(100) and Pt(110) domains of the Pd/Pt model system with the previous results for a clean Pt foil . . . . .	61
5.6	PEEM field of view containing two Pd powder agglomerates . . . . .	63
5.7	Hysteresis plot for the local PEEM intensity for the Pd agglomerate Pd I and corresponding frames during the CO oxidation at a constant temperature with a cyclic variation of the CO pressure and the corresponding kinetic phase diagram . . . . .	64
5.8	Comparison of the catalytic behaviour of two different Pd agglomerates under exactly the same reaction conditions . . . . .	66
5.9	Ignition-extinction experiments in the CO oxidation on the Pd part of the sample . . . . .	67
5.10	Formation of a reaction front in the CO oxidation reaction on Pd . . . . .	69

5.11	Reaction front propagation on a Pd foil . . . . .	70
5.12	Oxygen front on a Pd powder agglomerate . . . . .	72
5.13	Comparison of the velocity of the reaction fronts during CO oxidation experiments in a temperature range of 405 to 473 <i>K</i> on different Pd samples	73
5.14	Comparison between the catalytic behaviour of Pd powder impregnated into an Al <sub>2</sub> O <sub>3</sub> foil and a clean sputtered Pd foil . . . . .	75
5.15	Comparison of the catalytic behaviour of a Pd/Al <sub>2</sub> O <sub>3</sub> and a Pd/Pt model system . . . . .	75
5.16	Comparison between the catalytic behaviour of a clean sputtered Pd foil and that of the Pd/Pt model system . . . . .	76

## References

---

- [1] <http://www.forschungs-blog.de/katalysatoren-im-auto-konnen-auch-schadlich-sein/>, 07.12.12
- [2] G. ERTL, *Angew. Chem. Int. Ed.* **47**, 3524 (2008).
- [3] <http://www.sportkat.ch/katalysator.htm>, 28.10.2012
- [4] <http://m.autozeitung.de/taxonomy/term/48/0?page=315>, 07.12.2012
- [5] <http://www.mein-autolexikon.de/elektronik/katalysator.html>, 07.12.2012
- [6] I. Chorkendorff and J. Niemannsverdriet, *Concepts of Modern Catalysis and Kinetics*, Wiley-VCH., (2003).
- [7] G.ERTL, Nobel Prize Lecture, *Angew.Chem.* **120**, 3578 (2008).
- [8] [http://www.yambo-code.org/tutorials/Surface\\_spectroscopy/index.php](http://www.yambo-code.org/tutorials/Surface_spectroscopy/index.php), 24.06.2013
- [9] E. BRÜCHE, *Z. Phys.* **86**, 448 (1933).
- [10] W. ENGEL, M. E. KORDESCH, H. H. ROTERMUND, S. KUBALA, and A. VON OERTZEN, *Ultramicroscopy* **36**, 148 (1991).
- [11] E. BAUER, M. MUNDSCHAU, W. SWIECH, and W. TELIEPS, *Ultramicroscopy* **31**, 49 (1989).
- [12] M. E. KORDESCH, W. ENGEL, G. J. LAPEYRE, E. ZEITLER, and A. M. BRADSHAW, *Appl. Phys. A* **49**, 399 (1989).
- [13] S. GÜNTHER, B. KAULICH, L. Gregoratti, M. Kisikinova, *Surface Science* **70**, 187–260 (2002).
- [14] H. SIMON and R.SUHRMANN, *Der lichtelektrische Effekt und seine Anwendungen*, Springer-Verlag, Berlin, 1958.

## Bibliography

- [15] D. VOGEL, C. SPIEL, Y. SUCHORSKI, A. URICH, R. SCHLÖGL, G. RUPPRECHTER, *Surface Science* **605**, 1999–2005 (2011).
- [16] M. MCLEAN and H. MYKURA, *Surf. Sci.* **5**, 466 (1966).
- [17] R. SMOLUCHOWSKI, *Phys. Rev.* **60**, 661–674 (1941).
- [18] J. MARIEN, *Bull. Soc. R. Sci. Liège* **45**, 103 (1976).
- [19] S. NETTESHEIM, A. VON OERTZEN, H. H. ROTERMUND, and G. ERTL, *J. Chem. Phys.* **98**, 9977 (1993).
- [20] B. E. NIEUWENHUYS, R. BOUWMAN, and W. M. H. SACHTLER, *Thin Solid Films* **21**, 51 (1974).
- [21] J. LAUTERBACH, G. HAAS, H. H. ROTERMUND, and G. ERTL, *Surf. Sci.* **294**, 116 (1993).
- [22] P. R. NORTON, K. GRIFFITHS, and P. E. BINDNER, *Surf. Sci.* **138**, 125 (1984).
- [23] Y. SUCHORSKI, C. SPIEL, D. VOGEL, W. DRACHSEL, R. SCHLÖGL and G. RUPPRECHTER, *Chemphyschem*, **11**, 3231-3235 (2010)
- [24] D. VOGEL, C. SPIEL, Y. SUCHORSKI, A. TRINCHERO, R. SCHLÖGL, H. GRÖNBECK and G. RUPPRECHTER, *Angewandte Chemie*, **124**, 10185–10189 (2012)
- [25] R. IMBIHL and G. ERTL, *Chem. Rev.*, **95** (3), 697-733D (1995)
- [26] M. FALCKE and H. ENGEL, *J. Chem. Phys.*, **101** (7), 6255-6263 (1994)

# Oral talks and poster presentations

---

## Oral talks

- IMC Seminar of the Technical University of Vienna, 16.01.2013: *CO oxidation reaction on Palladium - Platinum model catalysts: kinetic transitions and spatial coupling*, M. DATLER

## Poster presentations

- (I) Special Research Program (SFB) F45 Functional Oxide Surfaces and Interfaces (FOXSI) Annual Symposium, 26.09.12 - 28.09.12, Conference Center Burg Schlaining, Stadtschlaining, Austria: *Visualizing the CO oxidation on powder samples: palladium versus platinum*, D. VOGEL, Z. BUDINSKA, M. DATLER, R. SCHLÖGL Y. SUCHORSKI and G. RUPPRECHTER.
- (II) 6th International Workshop on Surface Physics (IWSP) 2013, Functional Materials, 01.09.13 – 06.09.13 September 2013, Niemcza, Poland: *Kinetics of oxides formation on Zr and Pd surfaces: an XPS and PEEM study*, D. VOGEL, Z. BUDINSKA, I. BESPALOV, M. DATLER, R. SCHLÖGL, G. RUPPRECHTER and Y. SUCHORSKI.

**Abstract of (II):**

***Kinetics of oxides formation on Zr and Pd surfaces: an XPS and PEEM study***

The formation of oxides on metal surfaces is being extensively studied at present, whereas the deposited species segregated from the bulk or genuine surface can be oxidized [1, 2]. Mostly, the composition, the structure and the oxidation state are being studied rather than the kinetics and the mechanism of oxide formation. In the present contribution we apply XPS and PEEM to the kinetic studies of silicon oxide formation induced by Si-impurity segregation on the polycrystalline Pd surface and zirconium oxide formation via oxidation of the polycrystalline Zr surface. Activation energy values for both processes were obtained from the XPS data and the role of Zr suboxides in the oxidation of a Zr surface are discussed. The poisoning effect of SiO<sub>2</sub> formation in the CO oxidation reaction on Pd is revealed and its mechanism is discussed [2].

[1] S. Surnev, M.G. Ramsey, F.P. Netzer, Prog. Surf. Sci. 73 (2003) 117

U. Diebold, M. Schmid, Ann. Rev. Phys. Chem. 61 (2010) 129

D. Vogel, Z. Budinska, R. Schlögl, Y. Suchorski, G. Rupprechter, Cat. Lett. 143 (2013) 235.

**FOXSI**  
FunctionalOxide Surfaces and Interfaces  
Annual 8th FOXSI Symposium, September 26-29, 2015

**SFB F45**  
**04**

## Visualizing the CO oxidation on powder samples: palladium versus platinum

**TU WIEN**

**D. Vogel<sup>1,2</sup>, Z. Budinska<sup>1</sup>, M. Datler<sup>1</sup>, R. Schlögl<sup>2</sup>, Y. Suchorski<sup>1</sup> and G. Rupprechter<sup>1</sup>**

<sup>1</sup>Institute of Materials Chemistry, Vienna University of Technology, Vienna, Austria  
<sup>2</sup>Department of Inorganic Chemistry, Fritz-Haber-Institute of the Max-Planck-Society, Berlin, Germany

**Introduction and Motivation**



Microscopic visualization of ongoing catalytic reactions such as CO oxidation on platinum group metals allows to distill important information about the propagation of reaction fronts [1], pattern formation [2] and even about the local reaction kinetics on a  $\mu\text{m}$ -scale [3]. Till now, mainly single crystal samples [1, 2] and domains on polycrystalline foils [3] were used for the reaction imaging. We present the first results for the CO oxidation on Pt and Pd powders supported by oxidized Al foil ( $\text{Al}_2\text{O}_3$ ) imaged by photoelectron emission microscopy (PEEM).

supported Pd-powder catalyst prepared for the PEEM imaging

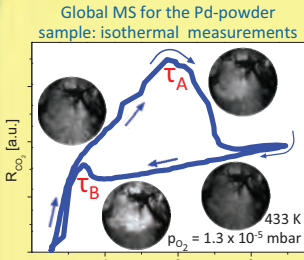
**Experimental Approach**



Local reaction kinetics was evaluated from the analysis of PEEM video-frames recorded *in situ* during the ongoing CO oxidation reaction in the  $10^{-5}$  mbar pressure range. The local image brightness is related via the work function to the local CO- or O-coverage and thus to the local  $\text{CO}_2$  production rate [4]. Simultaneously, the global  $\text{CO}_2$  reaction rate was measured by mass spectrometry (MS).

**CO oxidation reaction on  $\text{Al}_2\text{O}_3$  supported samples**

**Global MS for the Pd-powder sample: isothermal measurements**



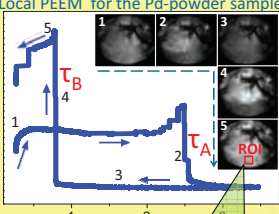
The CO oxidation reaction on  $\text{Al}_2\text{O}_3$  supported Pd and Pt powders was monitored *in situ* in the bistability region at constant oxygen pressure of  $1.3 \times 10^{-5}$  mbar by MS (global measurements, averaging the data over the whole sample) and by PEEM (parallel imaging technique, allowing local measurements) simultaneously. From the characteristic points in the hysteresis curves, typical for the bistability, the kinetic transition points  $\tau_A$  and  $\tau_B$  were obtained.

**Pd- and Pt-powders supported on  $\text{Al}_2\text{O}_3$**



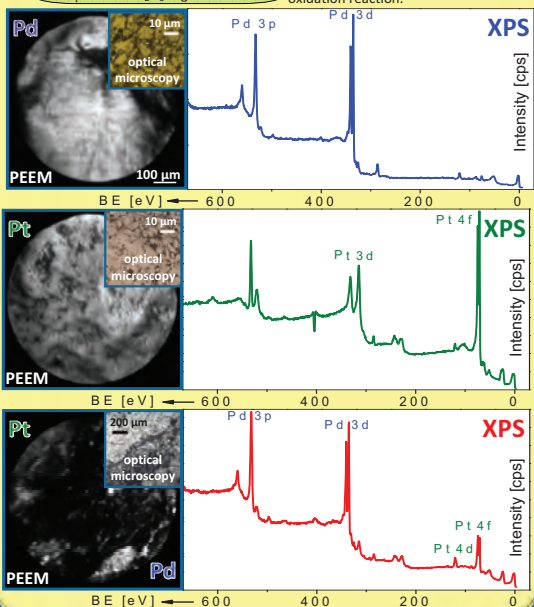
The „supported Pd and Pt catalysts“ samples were prepared by impregnation of the Pd black (Fluka AG) and Pt (Mateck) powders into the oxidized Al foil ( $\text{Al}_2\text{O}_3$ , as was confirmed by XPS). In UHV ( $10^{-9}$  mbar), the samples were Ar<sup>+</sup> sputtered and annealed at 623 K before the CO oxidation reaction.

**Local PEEM for the Pd-powder sample**



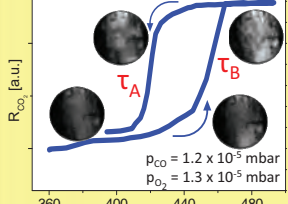
The spatially-resolved PEEM measurements (analysis of the ROI in the PEEM video-sequences corresponding to a surface area of  $\sim 65 \times 65 \mu\text{m}^2$ ) provide the local hysteresis curves for the chosen areas of the powder samples. video-sequences recorded during the CO oxidation reaction were analyzed within the ROI corresponding to  $\sim 65 \times 65 \mu\text{m}^2$  area on the surface.

**XPS**



Both Pd and Pt are well detectable on the combined sample.

**Global MS for the Pd-powder sample: isobaric measurements**



A ROI of the size of  $\sim 25 \times 25 \mu\text{m}^2$  was placed within the Pd-region on the combined Pd/Pt powder sample, the PEEM video sequences were analyzed, and the kinetic transitions  $\tau_A$  and  $\tau_B$  were determined.

**Summary**

The spatially resolved analysis of the PEEM data obtained during the ongoing CO oxidation on the  $\text{Al}_2\text{O}_3$  supported Pd and Pt powders allows to obtain the local kinetic phase diagrams with a spatial resolution down to  $1 \times 1 \mu\text{m}^2$  (one pixel limit). The possibility to place the ROIs arbitrarily in any region of the sample allows to perform such analysis for a chosen component, e.g. Pd in spatially heterogeneous samples with separated components.

**References**

[1] G. Ertl, *Angew. Chem. Int. Ed.* 47 (2008) 3524; [2] G. Ertl, *Science* 254 (1991) 1750; [3] D. Vogel, C. Spiel, Y. Suchorski, A. Trinchero, H. Grönbeck, R. Schlögl, G. Rupprechter, *Angew. Chem. Int. Ed.* 51 (2012); [4] Y. Suchorski, C. Spiel, D. Vogel, W. Drachsel, R. Schlögl, G. Rupprechter, *ChemPhysChem* 11 (2010) 3231.

Acknowledgements: Technical support by Johannes Frank (IMC, TU Vienna) is cordially acknowledged. This work was partially supported by FWF Austria (SFB-F45-04 FOXSI), GAD, Project 840US and the Vienna University of Technology (Innovatives Projekt "Spectromicroscopy of Surfaces by Metastable He atoms (He-SMS)").



## Kinetics of oxides formation on Zr and Pd surfaces: an XPS and PEEM study

D. Vogel, Z. Budinska, I. Bepalov, M. Datler, R. Schlögl, G. Rupprechter and Y. Suchorski  
Institute of Materials Chemistry, Vienna University of Technology, Vienna, Austria

FOXSI2  
Functional Oxide Surfaces and Interfaces

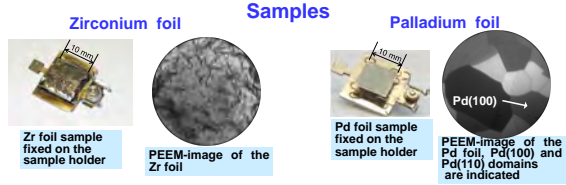
SFB F45  
04

### Motivation

Formation of oxides on the metal surfaces is extensively studied presently, whereas the deposited, segregated from the bulk or genuine surface species can be oxidized [1, 2]. Mostly, the composition, the structure and the oxidation state are studied, much less the kinetics and the mechanism of the oxide formation. In the present contribution we apply XPS and PEEM for the kinetic studies of the zirconium oxide formation via oxidation of the polycrystalline Zr surface and of the silicon oxide formation induced by Si-impurity segregation on the polycrystalline Pd surface. Activation energy values for both processes were obtained from the XPS data and the presence of Zr suboxides is detected. The role of the SiO<sub>2</sub> layer in the CO oxidation reaction on Pd is studied and the mechanism of the inhibiting effect [2] is revealed.

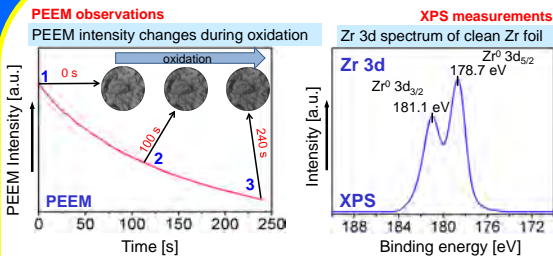
### Experimental approach

Chemical composition of the samples was monitored by XPS (SPECS, Germany). PEEM (STAIB, Germany) was applied to visualize *in situ* the oxidation processes. Kinetic data could be obtained from the XPS measurements and by processing of the corresponding video-PEEM sequences. For the CO oxidation on Pd, the global CO<sub>2</sub> formation rate was additionally monitored by QMS.



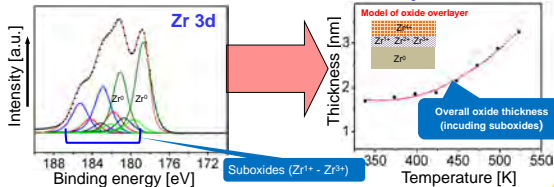
The Zr sample consisted of polycrystalline Zr foil (Mateck 99.9% purity), cleaned in UHV by several cycles of Ar<sup>+</sup> ion sputtering (E<sub>kin</sub>=1.7 keV) and annealing at 1073 K. A polycrystalline Pd foil (Alfa Aesar, 99.9% purity) consisted of 50–100 μm large grains of different crystallographic orientation formed after annealing the sample for several hours in UHV. The Pd sample was cleaned by several cycles of Ar<sup>+</sup> ion sputtering (E<sub>kin</sub>=1 keV) and annealing at 1073 K before each experiment. For the SiO<sub>2</sub> formation, the Pd sample was heated in oxygen (8x10<sup>-7</sup> mbar) at temperatures 873 to 1073 K.

### Initial oxidation of zirconium



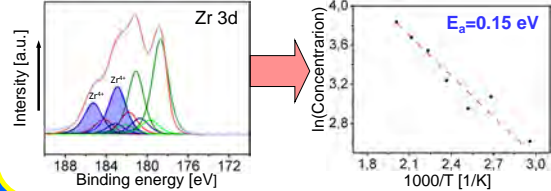
The appearance of Zr suboxides during the initial oxidation of Zr is still under discussion. However no satisfactory fitting can be obtained with three or less oxidation states. The Zr 3d spectra were analyzed in terms of five possible oxidation states of Zr (Zr<sup>0</sup>, Zr<sup>1+</sup>, Zr<sup>2+</sup>, Zr<sup>3+</sup>, and Zr<sup>4+</sup>) which would correspond to metallic Zr, Zr<sub>2</sub>O, ZrO, Zr<sub>2</sub>O<sub>3</sub>, ZrO<sub>2</sub> respectively. The Zr<sup>4+</sup> peaks were shifted by 4.2 eV relatively to the Zr<sup>0</sup> metal peaks. All suboxides were shifted by value of 1.05 eV per metal-oxygen bond.

### Thickness of the Zr oxide overlayer

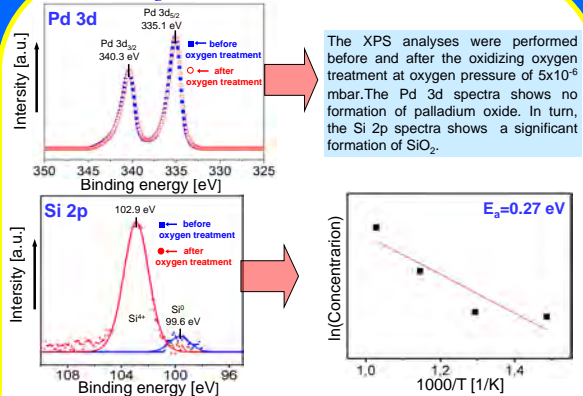


Acknowledgements: Technical support by Johannes Frank (IMC, TU Vienna) is cordially acknowledged. This work was supported by FWF Austria (SFB-F45-04 FOXSI).

### Activation energy of the ZrO<sub>2</sub> formation

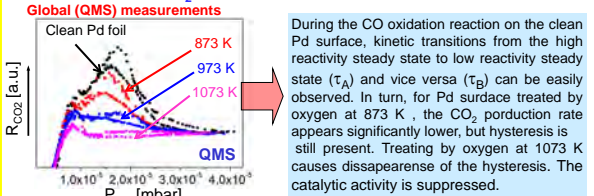


### SiO<sub>2</sub> formation on the Pd foil surface

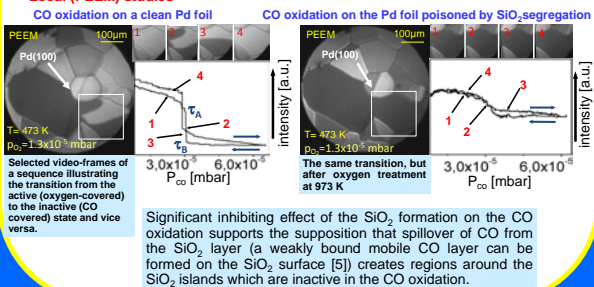


The presence of oxygen stimulates the diffusion of bulk-dissolved Si from the near-surface regions towards the surface and thus enhances the segregation of Si to the Pd surface (compare the Si<sup>0</sup> and the Si<sup>4+</sup> 2p signals, measured for the Si segregated without and with oxygen atmosphere).

### The role of the SiO<sub>2</sub> formation in the CO oxidation the Pd foil



### Local (PEEM) studies



### Summary

- Initial oxidation of the polycrystalline Zr has been studied under HV conditions (p<sub>O<sub>2</sub></sub>=1.3x10<sup>-5</sup> mbar) by PEEM and XPS in the temperature range 338 to 523 K.
- The Zr suboxides were detected and the thickness of the Zr overlayer was estimated.
- Segregation of Si on the Pd surface and subsequent SiO<sub>2</sub> formation under HV conditions (p<sub>O<sub>2</sub></sub>=1.3x10<sup>-5</sup> mbar) in the temperature range 873 to 1073 K has been examined using XPS and PEEM.
- Global (QMS) and local (PEEM, for the (100)-domain) studies detected a significant inhibiting effect of SiO<sub>2</sub> formation on the Pd reactivity towards CO oxidation.

### References

- [1] S. Survee, M.G. Ramsey, F.P. Netzer, Prog. Surf. Sci. 73 (2003) 117; [2] U. Diebold, M. Schmid, Ann. Rev. Phys. Chem. 61 (2010) 129; [3] D. Vogel, Z. Budinska, R. Schlögl, Y. Suchorski, G. Rupprechter, Cat. Lett. 143 (2013) 235; [4] P.L.J. Gunter, J.V. Niemandsverdiert, Appl. Surf. Sci. 89 (1995) 69; [5] A. Blomqvist, L. Lehman, P. Salo, Phys. Stat. Sol. 249 (2012) 1046